

# Grain Size Effects on the Mechanical Behaviour of Polycrystalline Nickel from Micro to Nanoscale

## **Dissertation**

Zur Erlangung des Grades des  
Doktors der Ingenieurwissenschaften (Dr.-Ing.)  
der Naturwissenschaftlich-Technischen Fakultät III  
Chemie, Pharmazie, Bio- und Werkstoffwissenschaften  
der Universität des Saarlandes

von

**Dipl.-Ing. Bo Yang**

Saarbrücken, 2006

Eingereicht am: 20.06.2006  
Tag der mündlichen Prüfung: 24.11.2006  
Dekan: Prof. Dr. K. Hegetschweiler  
Vorsitzender: Prof. Dr. R. Clasen  
Berichterstatter: Prof. Dr. H. Vehoff  
Prof. Dr. W. Arnold  
Akad. Mitarbeiter: Dr. F. Aubertin

# Acknowledgements

I am sincerely grateful to my advisor, Prof. Dr. rer. nat. Horst Vehoff, for his support and supervision during my Ph.D study in his institute. He is one man in my life who urged me on by way of his untiring studying in the kingdom of materials science.

I sincerely appreciate Prof. Dr. Mathias Göken of Erlangen-Nuernberg University for giving me the opportunity to work here, for his continuous help and advice and successful organization of the workshop every year.

During the course of this work, I was supported under the contract number SFB 277 (B8). The support of the Deutsche Forschungsgemeinschaft is gratefully acknowledged. I would like to thank Prof. Rolf Hempelmann for providing me the nanonickel.

I thank Miss Kerstin Schüler and Mr. Michael Marx very much for their advice and help for my dissertation; Mr. Karsten Durst, Mr. Markus Kempf, Mr. Mark Henning, Mr. Afroz Barnoush, Miss Dephine Lemaire, Mr. Thomas Waschkies, Mr. Andreas Noll, Mr. Jürgen Braun, Mr. Wolfgang Schäf, Mr. Markus Welsch, Mr. Johaness Müller, Mr. Elmar Schweitzer, Mr. Jens Weggler, Mr. Wolfgang Jung for their help and fruitful discussions and Mr. Stefan Monz and Mr. Hao Shen for the XRD measurements and discussions.

I thank all the numbers in the research group, Mrs. Elisabeth Ohm, Mr. Horst Vogel-Knels, Miss Rita Maron, Mr. Andreas Kirsch, Mr. Peter Limbach, Mr. Rolf Kiefer, Mr. Stefan Schmitz etc., for their help and making me a harmonious and pleasant life in Germany.

I give my special thanks to my family: my parents, for giving me life and bringing me up; my wife, the best friend and partner in my life, for giving me endless love, unconditional support and encouragement; my daughter, for giving me so much pleasure and responsibility.

# Abstract

In this work the grain size effects on the mechanical behaviour of polycrystalline nickel from micro to nanoscale were studied. Pulse-electrodeposited nanocrystalline nickel was heat-treated to produce different grain sizes. The interaction between dislocations nucleated under the indenter tip and individual grain boundaries was examined by performing nanoindents always in the center of the largest grains in a given metallographic section with a nanoindenting atomic force microscope. The results show that hardness not only depends on the grain size, but also on the ratio of the indent size to the grain size. With increasing indentation depth, hardness increases or decreases, depending on the relationship between the grain size and the plastic zone size. Direct dislocation-boundary-interaction was observed in the grain size range of 300 nm to 900 nm, where the pop-in width increases with increasing grain size. Later pop-ins occur at lower loads with increasing pop-in widths and could be regarded as the sign of activation of new dislocation sources in the adjacent grains. The result is in agreement with the theoretical prediction of the classical Hall-Petch model.

Strain rate-controlled tensile and nanoindentation experiments are performed to reveal the grain size effects on deformation mechanisms. Results show that with decreasing grain size, the strain rate sensitivity increases and the activation volume decreases. Quantitative analyses of the activation volume show different dislocation sources in coarse-grained nickel and nanocrystalline nickel. Room temperature creep behaviour was observed in nanocrystalline nickel. In-situ bending experiments on bulk nanonickel in an atomic force microscope, for the first time, show that grain boundary sliding at room temperature plays an important role during bending and fatigue tests, and the fatigue crack is intergranular. These results demonstrated that in nanocrystalline nickel the grain boundary mediated deformation processes play a significant role.

In der vorliegenden Arbeit wurde der Einfluß der Korngröße auf das mechanische Verhalten von polykristallinem Nickel von der Mikro- zur Nanoskala untersucht. Die unterschiedlichen Korngrößen wurden durch Wärmebehandlung von nanokristallinem Nickel, das über Elektrochemische Impulabscheidung hergestellt wurde, eingestellt. Mit dem nanoindentierenden Rasterkraftmikroskop wurden Versetzungen unter der Indenterspitze nukleiert und deren Wechselwirkungen mit Korngrenzen untersucht. Die Ergebnisse zeigen, dass die Nanohärte nicht nur von der Korngröße abhängt, sondern auch von dem Verhältnis der Größe des Nanohärteeindrucks zur Korngröße. Mit zunehmender Eindringtiefe des Indenters steigt oder fällt die gemessene Härte in Abhängigkeit von der Beziehung der Korngröße zur Größe der resultierenden plastischen Zone. Im Korngrößenbereich von 300 nm bis 900 nm wurde eine direkte Wechselwirkung zwischen Versetzungen und Korngrenzen beobachtet. Dabei steigt die Pop-in-Tiefe mit wachsender Korngröße. Die Pop-ins höherer Ordnung erscheinen hier bei immer niedrigeren Lasten und mit wachsenden Pop-in-Tiefen. Sie können als Zeichen für die Aktivierung von neuen Versetzungsquellen in den direkt benachbarten Körnern angesehen werden. Die Ergebnisse in diesem Bereich stimmen mit den theoretischen Vorhersagen des klassischen Hall-Petch-Modells überein.

Um Einflüsse der Korngröße auf das Umformverhalten festzustellen wurden zusätzlich zu dehnratenkontrollierten Nanoindentierungsversuchen makroskopische Dehnratenwechselversuche unter zügiger Beanspruchung durchgeführt. Für kleiner werdende Korngrößen steigen die Dehnratenempfindlichkeiten und die Aktivierungsvolumina fallen. Quantitative Analysen des Aktivierungsvolumens zeigen jeweils unterschiedliche Versetzungsquellen für grobkörniges und nanokristallines Nickel. Weitere Untersuchungen beziehen sich auf das Kriechverhalten von nanokristallinem Nickel bei Raumtemperatur. Durch In-situ-Biegeversuche an massivem Nanonickel konnte im Rasterkraftmikroskop zum ersten Mal gezeigt werden, dass Korngrenzengleiten bei Raumtemperatur eine wichtige Rolle während der Biege- und Ermüdungsversuche spielt. Der beobachtete Ermüdungsriss verläuft intergranular. Alle diese Ergebnisse zeigen die herausragende Bedeutung von Korngrenzenmechanismen bei der Verformung von nanokristallinem Nickel auf.

# Contents

<b>Acknowledgements</b>	<b>iii</b>
<b>Abstract</b>	<b>iv</b>
<b>List of Figures</b>	<b>xi</b>
<b>List of Tables</b>	<b>xv</b>
<b>Symbols</b>	<b>xvi</b>
<b>Acronyms</b>	<b>xviii</b>
<b>1 Introduction</b>	<b>1</b>
<b>2 Literature Review</b>	<b>4</b>
2.1 Nanocrystalline materials – synthesis, general characteristics and mechanical properties . . . . .	4
2.1.1 Synthesis . . . . .	4
2.1.1.1 Gas-phase condensation . . . . .	5
2.1.1.2 Mechanical alloying . . . . .	5
2.1.1.3 Severe plastic deformation . . . . .	6
2.1.1.4 Electrodeposition . . . . .	6
2.1.2 General characteristics . . . . .	7
2.1.3 Mechanical properties . . . . .	8
2.1.3.1 Elastic modulus . . . . .	8
2.1.3.2 Hardness and yield strength . . . . .	9

## Contents

---

2.1.3.3	Reduced ductility . . . . .	9
2.1.3.4	Enhanced diffusional creep . . . . .	10
2.1.3.5	Improved superplasticity . . . . .	11
2.2	A general introduction to plastic deformation . . . . .	12
2.2.1	Dislocation glide and climb . . . . .	12
2.2.2	Thermal activation of dislocation . . . . .	12
2.2.3	Creep . . . . .	14
2.2.4	A general survey of the deformation mechanisms – Ashby maps . . . . .	16
2.3	Explanations of the Hall-Petch relation . . . . .	18
2.3.1	Dislocation pile-up model . . . . .	18
2.3.2	Dislocation density model . . . . .	19
2.4	Grain boundary mediated deformation mechanisms in nanocrystalline metals . . . . .	20
2.4.1	Nucleation of dislocations and stacking faults from grain boundaries . . . . .	20
2.4.2	Emission of deformation twins from grain boundaries . . . . .	22
2.4.3	Transformation of grain boundary dislocation pile-ups at triple junction . . . . .	23
2.4.4	Grain boundary sliding and grain rotation . . . . .	25
2.5	Methods of investigation . . . . .	28
2.5.1	Atomistic simulations . . . . .	28
2.5.2	Microscopic observations . . . . .	31
2.5.3	In-situ X-ray diffraction profile . . . . .	35
2.5.4	Study of the thermal activation parameters . . . . .	37
2.5.5	Nanoindentation . . . . .	38
2.5.5.1	Background information . . . . .	38
2.5.5.2	Pop-in and dislocation nucleation during nanoindentation . . . . .	42
2.5.5.3	Indentation size effect . . . . .	44
2.6	Open questions and aims . . . . .	46
2.6.1	Local examination of Hall-Petch relation . . . . .	46
2.6.2	Deformation mechanisms of bulk electrodeposited nanonickel . . . . .	48

## **3 Experimental 50**

## Contents

---

3.1	Specimen preparation . . . . .	50
3.1.1	As-prepared specimen . . . . .	50
3.1.2	Specimens for indentation, tensile and bending tests . . . . .	50
3.1.3	Heat-treatments . . . . .	50
3.1.4	Surface finish preparation . . . . .	51
3.1.4.1	Mechanical polishing . . . . .	51
3.1.4.2	Electropolishing . . . . .	52
3.2	Microstructure analysis . . . . .	52
3.3	Mechanical property measurements . . . . .	52
3.3.1	Microindentation . . . . .	52
3.3.2	Nanoindentation . . . . .	52
3.3.3	Tensile experiments . . . . .	53
3.3.4	In-situ bending AFM experiments . . . . .	53
3.4	Equipments . . . . .	53
3.4.1	Hysitron TriboScope . . . . .	53
3.4.1.1	System . . . . .	53
3.4.1.2	Probe tips . . . . .	55
3.4.1.3	Machine compliance and tip shape calibration . . . . .	56
3.4.2	In-situ bending AFM . . . . .	59
3.5	Influences of specimen preparation on nanoindentation . . . . .	63
3.5.1	Mechanical polishing and electropolishing . . . . .	63
3.5.2	Oxide films . . . . .	64
3.5.3	Roughness . . . . .	65
<b>4</b>	<b>Results</b>	<b>67</b>
4.1	Microstructure . . . . .	67
4.1.1	Microstructure of as-prepared nickel . . . . .	67
4.1.1.1	As-prepared coarse-grained nickel . . . . .	67
4.1.1.2	As-prepared nanocrystalline nickel . . . . .	68
4.1.1.3	Microstructure of heat-treated nickel . . . . .	69

## Contents

---

4.2	Microhardness . . . . .	70
4.3	Nanohardness and reduced modulus . . . . .	71
4.3.1	Effects of grain boundaries and triple points . . . . .	73
4.3.2	Nanoindentation with peak force 2000 $\mu\text{N}$ . . . . .	74
4.4	Strain rate sensitivity and activation volume . . . . .	75
4.4.1	Strain rate sensitivity examined by nanoindentation . . . . .	75
4.4.1.1	Definition of strain rate sensitivity under indentation . . . . .	75
4.4.1.2	Strain rate sensitivity studied with peak load 4000 $\mu\text{N}$ . . . . .	76
4.4.1.3	Strain rate sensitivity studied with peak load 300 $\mu\text{N}$ . . . . .	77
4.4.2	Tensile strain rate jump experiments . . . . .	78
4.4.2.1	Definition of the strain rate sensitivity and activation volume from a tensile strain jump test . . . . .	78
4.4.2.2	Results of tensile strain jump experiments . . . . .	80
4.5	Stress jump experiments in creep tests . . . . .	82
<b>5</b>	<b>Discussion</b>	<b>84</b>
5.1	Nanohardness dependence on the ratio of indent size and grain size . . . . .	84
5.1.1	Microindentation with peak force of 490 mN . . . . .	85
5.1.2	Nanoindentation with peak forces of 600 $\mu\text{N}$ , 300 $\mu\text{N}$ and 250 $\mu\text{N}$ . . . . .	86
5.1.3	Conclusion . . . . .	89
5.2	Indentation size effect in individual grains . . . . .	90
5.2.1	Schematic diagram of nanoindentation performed in the center of a sin- gle grain . . . . .	91
5.2.2	Indentation size effect vs. Grain boundary effect . . . . .	93
5.2.3	Indentation size vs. plastic zone size . . . . .	97
5.2.4	The spreading of the plastic zone out of the indented single grains . . . . .	97
5.2.5	Conclusion . . . . .	98
5.3	Direct observation of dislocation-boundary-interaction in ultrafine grains . . . . .	99
5.3.1	The first pop-in behaviour vs. individual grain size . . . . .	100
5.3.2	The later pop-ins . . . . .	104

## Contents

---

5.3.3	Conclusion . . . . .	105
5.4	Grain size effects on the deformation mechanisms revealed from the plastic strain rate-controlled experiments . . . . .	106
5.4.1	Grain size effects on the tensile deformation mechanisms . . . . .	106
5.4.2	Grain size effects on the indentation deformation mechanisms . . . . .	108
5.4.3	Plastic deformation kinetics revealed by analysis of activation volume . . . . .	114
5.4.4	Conclusion . . . . .	116
5.5	Grain size effects on the room temperature creep behaviour and the creep mechanisms of nanocrystalline nickel according to Norton's creep law . . . . .	117
5.6	Deformation behaviour of bulk nanonickel studied by in-situ bending AFM . . . . .	120
5.6.1	Bending behaviour . . . . .	120
5.6.2	Fatigue response and fracture behaviour . . . . .	121
5.7	The local dislocation-boundary-interaction and the deformation mechanisms of bulk nanocrystalline nickel . . . . .	124
<b>6</b>	<b>Summary</b>	<b>126</b>
<b>A</b>	<b>Mechanical properties of different as-deposited nanonickel</b>	<b>130</b>
<b>B</b>	<b>Effects of annealing on tensile properties of nanonickel</b>	<b>132</b>
<b>C</b>	<b>The reverse Hall-Petch effect caused by annealing</b>	<b>135</b>
C.1	Effects of annealing on the hardness and elastic modulus . . . . .	135
C.2	Explanations . . . . .	135
	<b>Bibliography</b>	<b>138</b>
	<b>Publications</b>	<b>149</b>

# List of Figures

1.1	Variation of strength with grain size for metals . . . . .	3
2.1	A mobile dislocation hung up on dislocation trees . . . . .	13
2.2	A glide resistance diagram . . . . .	13
2.3	Schematic representation of a creep curve . . . . .	15
2.4	A deformation map of pure nickel with mean grain diameter $d = 1 \text{ mm}$ . . . . .	17
2.5	Pile-up of dislocations at grain boundaries . . . . .	19
2.6	Emission of a partial dislocation followed by stacking fault (SF) from grain boundaries . . . . .	21
2.7	Perfect dislocation splits into Shockley partials connected by a stacking fault . . . . .	21
2.8	Deformation twin created by emission of partial dislocations . . . . .	22
2.9	Transformations of grain boundary dislocation pile-ups at triple junctions . . . . .	23
2.10	Combined action of grain boundary sliding and rotational deformation mode . . . . .	26
2.11	Enhancement of the climb of grain boundary dislocations . . . . .	27
2.12	A pile-up formed in a nanograin . . . . .	30
2.13	A simulated NC copper sample before and after deformation . . . . .	31
2.14	Map of the operational deformation mechanisms in NC fcc metals . . . . .	32
2.15	A sequence of images captured during an in-situ deformation test in the TEM of NC Ni . . . . .	33
2.16	Deformation twins and stacking faults in NC Al . . . . .	34
2.17	Dark-Field TEM observation of the rapid genesis of an agglomerate . . . . .	36
2.18	Indentation geometry at maximum load and after unloading . . . . .	40
2.19	Nanoindentation data analysis model . . . . .	41

*List of Figures*

---

2.20	Schematic diagram of dislocation nucleation during nanoindentation . . . . .	42
2.21	Hertzian contact model used for to fit the pure elastic part of F-h curves . . . . .	43
2.22	Geometrically necessary dislocations created by a rigid conical indentation . . . . .	44
2.23	Studying the dislocation-boundary-interaction by NI-AFM . . . . .	47
3.1	As-deposited nanocrystalline nickel plate and specimens . . . . .	51
3.2	Shape of specimens for tensile and bending tests . . . . .	51
3.3	Triboscope indentation system . . . . .	54
3.4	Hysitron TriboScope transducer assembly . . . . .	56
3.5	Nanoindentation probe tips and their projected area related to the depth . . . . .	57
3.6	Nanoindentation tests on fused quartz for tip calibration . . . . .	59
3.7	Contact area as a function of contact depth of the Berkovich indenter . . . . .	60
3.8	Loading device of the 4-point-bend experiment . . . . .	60
3.9	NiAl single crystal in soft orientation . . . . .	61
3.10	AFM images of the deformation process near the crack tip of a NiAl single crystal . . . . .	61
3.11	Photograph of the bending machine . . . . .	61
3.12	Schematic diagram of the developed in-situ bending AFM . . . . .	62
3.13	In-situ AFM imaging the deformation process of coarse-grained nickel during bending . . . . .	62
3.14	Surface effects on nanoindentation with a peak loading force of $600 \mu\text{N}$ . . . . .	64
3.15	Oxide film effects on the force-displacement curves of nanoindentation on an annealed nickel single crystal . . . . .	65
3.16	Oxide film effects on the force-displacement curves of nanoindentation on NC nickel . . . . .	66
4.1	Surface structure of CG nickel . . . . .	68
4.2	Microstructure of as-deposited NC nickel . . . . .	69
4.3	TEM images of the microstructure of as-deposited NC nickel . . . . .	70
4.4	XRD pattern of as-deposited NC nickel . . . . .	71
4.5	Grain structure after different heat-treatments on as-prepared NC nickel . . . . .	72
4.6	TEM observation of the microstructure after different heat-treatments . . . . .	73

*List of Figures*

---

4.7	Microhardness vs. mean grain size . . . . .	75
4.8	Load functions of nanoindentation . . . . .	76
4.9	Nanoindentation at different positions . . . . .	77
4.10	Nanohardness and modulus vs. grain size . . . . .	78
4.11	Nanoindentation with peak load 4000 $\mu\text{N}$ and different indenting rates . . . . .	79
4.12	Nanoindentation with peak load 300 $\mu\text{N}$ and different indenting rates . . . . .	80
4.13	Definition of strain rate sensitivity and experimental activation volume . . . . .	81
4.14	True stress-strain curves of NC nickel and CG nickel in a tensile rate jump test .	81
4.15	Strain rate sensitivity and activation volume of CG nickel . . . . .	82
4.16	Tensile stresses for the different stress jump number . . . . .	82
4.17	Creep rate at different stages . . . . .	83
5.1	Definition of indent size . . . . .	84
5.2	Microhardness vs. mean grain size . . . . .	86
5.3	Nanohardness vs. grain size with a peak load of 600 $\mu\text{N}$ . . . . .	87
5.4	Nanohardness vs. grain size with a peak load of 300 $\mu\text{N}$ . . . . .	89
5.5	Nanoindentation in the center of individual grains with a peak load of 250 $\mu\text{N}$ .	90
5.6	Schematic of nanoindentation performed in the center of a grain . . . . .	92
5.7	Schematic of the indenter with a tip radius $R$ . . . . .	93
5.8	Nanohardness vs. Indentation depth . . . . .	94
5.9	Examination of the indentation size effect in single grains . . . . .	95
5.10	Nanoindentation in the center of individual grains with a peak force of 300 $\mu\text{N}$	100
5.11	The first pop-in force and displacement vs. individual grain size . . . . .	101
5.12	The first pop-in width and maximum shear stress vs. individual grain size . . .	102
5.13	Later pop-ins vs. individual grain size . . . . .	104
5.14	Strain rate sensitivity of NC nickel and CG nickel as a function of plastic strain	107
5.15	Nanoindentation on CG, UFG and as-deposited NC nickel with peak force of 4000 $\mu\text{N}$ and different indent rates . . . . .	109
5.16	Hardness and strain rate sensitivity of CG, UFG and as-deposited NC nickel . .	110
5.17	Hardness and strain rate sensitivity of grains with sizes of 850 nm and 400 nm.	111

*List of Figures*

---

5.18	Local examination of indent rate effects in UFG grains . . . . .	112
5.19	Fraction of interfacial atoms of a grain related to the grain size . . . . .	113
5.20	Surface area before and after indentation . . . . .	114
5.21	Activation volume of NC nickel and CG nickel as a function of plastic strain . .	115
5.22	Creep rate as a function of the stress plotted with log-log form . . . . .	118
5.23	Bending response of NC nickel . . . . .	120
5.24	Surface topography of as-deposited NC nickel after fatigue . . . . .	121
5.25	AFM images of as-deposited NC nickel after fatigue . . . . .	122
5.26	Crack tip of as-deposited nanocrystalline nickel . . . . .	123
A.1	Engineering stress-strain curves for as-prepared nickel . . . . .	131
B.1	Room temperature engineering stress-strain curves of as-deposited and heat- treated NC nickel . . . . .	132
B.2	SEM fractographs of electrodeposited nickel . . . . .	133
C.1	Reduced modulus evolution with heat treatments . . . . .	136

# List of Tables

4.1	Mean grain size and microhardness of as-deposited and heat-treated specimens	74
4.2	SRS of CG, UFG and as-deposited NC nickel . . . . .	79
4.3	SRS in UFG size range . . . . .	80
A.1	Mean grain size, microhardness, nanohardness and reduced modulus of different as-deposited NC nickel specimens . . . . .	131
C.1	Grain size and microstrain of as-deposited and annealed nanocrystalline nickel	137

# Symbols

$a$	contact radius
$A_c$	contact area
$b$	Burgers vector
$d$	grain size
$d_c$	critical grain size for the transition of Hall-Petch behavior
$d'$	the distance the dislocation must move before the dislocation tree is cut
$\Delta G$	activation energy
$\delta$	thickness of the grain boundary
$D_{gb}$	coefficients of grain boundary diffusion
$D_L$	coefficients of lattice diffusion
$E$	elastic modulus
$E_r$	reduced elastic modulus
$\dot{\epsilon}$	strain rate
$\dot{\epsilon}_s$	steady-state creep rate
$F$	applied force
$f$	a factor related with $r$ and $a$
$F_s$	the volume fraction of soft triple junctions
$F_h$	the volume fraction of hard triple junctions
$H$	hardness
$H_V$	Vickers microhardness
$h$	indentation depth

## Symbols

---

$k$	Hall-Petch constant
$k'$	Hall-Petch constant
$k_B$	Boltzmann constant
$L$	pile-up length
$l'_0$	the distance between the dislocation trees
$m$	strain rate sensitivity
$\mu$	shear modulus
$n$	the coefficient
$\Omega$	vacancy volume
$q$	geometric factor
$\rho$	dislocation density
$R$	tip radius
$r$	radius of the plastic zone
$s$	radius of the indentation size
$S$	contact stiffness
$S_m$	indent size of microindentation
$S_n$	indent size of nanoindentation
$\sigma$	applied stress
$T$	absolute temperature
$T_m$	melting point
$\tau_e$	effective shear stress
$\tau_0$	lattice friction stress
$\tau_p$	stress at the head of the pile-up
$\tau_y$	yield stress
$U_0$	the energy needed to overcome the obstacles when no stress is applied to the crystal
$V$	the plastic deformation volume
$V_a$	activation volume

# Acronyms

AFM	atomic force microscope
AV	activation volume
bcc	body-centered-cubic
CG	coarse-grained
DSI	depth sensing indentation
ED	electrodeposition
EDM	electro-discharge machine
fcc	face-centered-cubic
GBD	grain boundary dislocation
GND	geometrically necessary dislocation
MC	microcrystalline
MD	molecular dynamics
NC	nanocrystalline
NI-AFM	nanoindentation combined with an AFM
OM	Optical Microscopy
SEM	Scanning Electron Microscopy
SF	stacking fault
SPD	Severe plastic deformation
SPM	Scanning Probe Microscopy
SRS	strain rate sensitivity
TEM	Transmission Electron Microscopy
UFG	ultrafine-grained

# 1 Introduction

The microstructure of engineering materials determines a wide variety of the sample properties. Therefore, the study of microstructure-property relationship has been historically of great interest to the scientists and engineers. Of all the microstructural parameters which influence the mechanical properties of polycrystalline metals and alloys, the grain size has been proved to be the most important.

The strong influence of grain size on the mechanical properties of materials, a subject of continuous investigation since the early work of Hall [Hal51] and Petch [Pet53], has been observed with historical roots going back many decades. An increase in yield strength with decreasing grain size is characteristic of many metals and alloys. This has become known as the Hall-Petch (H-P) effect following the recognition that the relationship between the yield stress  $\tau_y$  and the average grain size  $d$  is described as:

$$\tau_y = \tau_0 + kd^{-0.5} \quad (1.1)$$

where  $\tau_0$  is the lattice friction stress needed to move individual dislocations and  $k$  the so-called H-P constant.

At low homologous temperatures ( $T/T_m$ , where  $T$  is the absolute temperature and  $T_m$  the melting point) the hardness,  $H_V$  (Vickers microhardness), is related to the yield stress  $\tau_y$  through the empirical relationship  $H_V/\tau_y \approx 3$  [Tab51], this leads to the similar size dependence of hardness:

$$H_V \approx H_0 + k'd^{-0.5} \quad (1.2)$$

where  $H_0$  are  $k'$  are constants.

The validity of H-P relationship has been confirmed for many metals and alloys. Many models were proposed to explain the H-P relationship. Among them the most popular one

is the dislocation-pile-up model [Mey82], in which it is assumed that yielding occurs when the stress deduced by the dislocations contained in a pile-up is large enough to activate a dislocation source in the adjacent grain. The length of the pile-up is assumed to be proportional to the grain size, e.g. pile-up in larger grains may contain more dislocations than that in smaller grains. Therefore, in larger grains the stress concentration caused by the pile-up is larger and a lower external stress is needed for the occurrence of yielding. Consequently, metals with smaller grains exhibit a higher yield stress. However, besides in the Transmission Electron Microscopy (TEM) where the pile-ups could be observed directly, the local interaction between dislocations and grain boundaries described in the dislocation pile-up model was never examined in bulk specimens. As a result, the origin of H-P relationship is not completely understood yet.

In recent years the availability of nanocrystalline (NC) materials (or some other common names such as nanophase materials, nanocrystals, nanostructured materials, nanometre sized crystalline solids, ultrafine structures or submicrometre structures [Sio04]) paves the way for the potential discovery of new phenomena observable only in the NC regime, igniting a renewed interest in the influence of grain size on the mechanical properties of materials. With an average grain size (typically smaller than 100 nm) several orders of magnitude smaller than that of conventional polycrystalline materials, NC materials provide a unique opportunity to investigate the grain size effects on the mechanical properties at an extremely fine microstructural scale.

Superior mechanical properties of NC materials compared to coarse-grained (CG) or microcrystalline (MC, average grain size larger than 1000 nm) counterparts have been reported, such as increased resistance to tribological and environmentally-assisted damage [Kum03], high ductility [Yam00, Ehr97], the promise of enhanced superplastic formability at lower temperatures [McF99], and dramatically increased strength and hardness due to the normal H-P effect [Nie91, Sie97]. However, experimental measurements also show various deviations from the H-P equation as grain size becomes very small. A decrease of the H-P slope  $k$  was always found, and in some cases (grain size in the range of 5–30 nm observed in some experiments) even a negative  $k$  was reported, i.e. grain size softening, the so-called “inverse H-P behavior” [Cho89]. The variation of yield stress as a function of grain size for metals is schematically shown in Fig. 1.1. It shows that the strength of the material first increases (“normal H-P behavior”) and then decreases with decreasing grain size (“inverse H-P behavior”) [Yip98]. As the

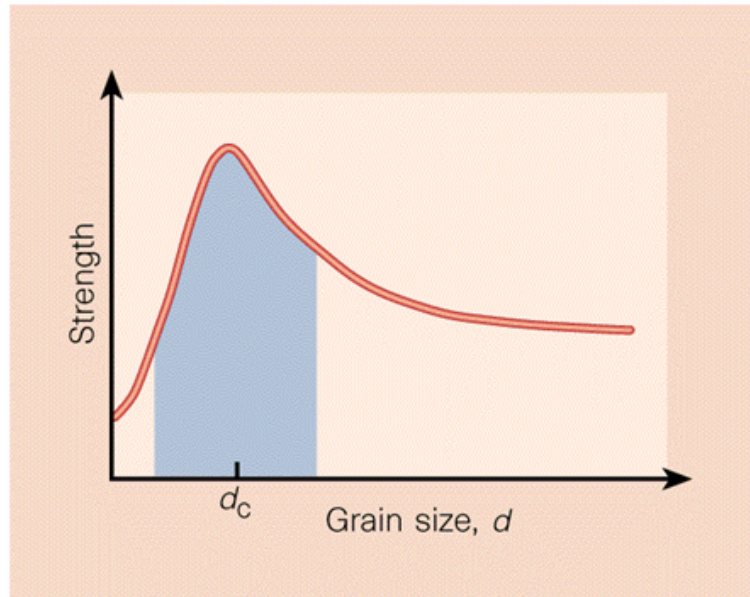


Figure 1.1: Variation of strength with grain size for metals.

mechanical property and deformation mechanism are interactive, the transition of H-P behavior from “normal” to “inverse” at a critical grain size  $d_c$  is therefore thought to be due to a change in the dominant deformation mechanism. At sufficiently small grain sizes, the H-P relationship based on the dislocation pile-up is expected to fail, as the volume of material is too small for a dislocation model to be meaningful and other modes of deformation must dominate, such as twinning, grain boundary sliding or grain rotation, etc. However, the deformation mechanisms related to the complexity of grain size dependence of mechanical properties in NC materials are still under debate, although there is a considerable experimental and theoretical effort so far.

The above considerations motivate the research described in this thesis (I) studying the mechanical properties of materials with grain sizes ranging from micro- to nanoscale systematically and (II) unravelling the mystery underlying this technologically and fundamentally important phenomenon related to the grain size.

# 2 Literature Review

## 2.1 Nanocrystalline materials – synthesis, general characteristics and mechanical properties

### 2.1.1 Synthesis

The successful synthesis of large-scale materials with grain sizes in NC range represents a major achievement in the emerging field of nanotechnology [Koc02]. NC materials can be produced in the following forms: thin films, coatings, powders and as a bulk material. Inspection of the scientific literature indicates that there are many synthesis techniques, like:

- inert gas condensation or chemical vapour condensation [Sur95, Gle89]
- electrodeposition [Els95]
- crystallization of amorphous solids [Lu96]
- plasma synthesis [Bir89]
- severe plastic deformation [Val00]
- consolidation of mechanically alloyed or cryomilled powders [Sun00, Tel01]

Only a few of these techniques can generate nanostructures with sufficient thermal stability to permit the fabrication of bulk materials. These techniques will be briefly introduced in the following parts.

### 2.1.1.1 Gas-phase condensation

NC bulk materials can be manufactured by the consolidation of powders from gas-phase condensation (or inert-gas condensation techniques). This method was pioneered by the group of Birringer and Gleiter [Bir84]. Nano-sized powder particles are produced by a rapid condensation of a vapour phase which is essentially evaporation of a solid metal. The particles are then consolidated in a die using high pressures and, in some cases, with additional thermal energy.

This process has several limitations:

- the limited specimen volume
- purity issues, particularly in the vicinity of the particle boundaries
- porosity from incomplete densification

The incomplete densification results in specimens with densities lower than 99% of the theoretical density. This has great effects on the mechanical properties of the specimen. For example, tensile behavior of the nanostructured Cu and Pd alloys is significantly influenced by the residual porosity after consolidation. Because of the existence of porosity, all the nanostructured specimens fail in the strain-hardening region. The values of Young's modulus of the nanostructured Cu and Pd alloys increase with decreasing fraction of porosity [Niem91]. Therefore, eliminating the porosity in nanostructured materials processed via gas-phase condensation is still a critical challenge for the improvement of the mechanical (especially tensile) properties.

### 2.1.1.2 Mechanical alloying

Mechanical alloying, first developed in the 1960s, is a high energy ball milling process [Gil83, Koc89]. It has been used widely for the preparation of powders in ultrafine-grained (UFG, average grain size 100–1000 nm) and nanograin size [Tak92, Fec95], particularly successful with aluminium alloys [Tel01, Zho03]. During milling, the material undergoes a severe plastic deformation resulting in grain refinement. Bulk NC bulk materials can be produced after consolidation of the powders under appropriate conditions. There are several popular approaches such as high-temperature sintering, hot isostatic pressing (HIP) and cold isostatic pressing (CIP), of which HIP is more effective for generating high density bulk.

A further effective process for manufacturing bulk nanostructured Al alloys in recent years developed from mechanical alloying is cryomilling. The powder normally has a grain size of about 20 nm, and the processing usually includes several steps: cryomilling, degassing, consolidation and secondary processing [Han05]. The presence of fine oxides/nitrides that result from the milling process is key to maintaining the fine grain size during consolidation. While the advantage of the process lies in its ability to produce billets with reasonable size, its principal disadvantages include the inability to control material purity and obtain full density. Since the consolidated materials usually have a density lower than the theoretical density, a secondary processing at high temperature, for instance, extrusion or forging, has to be performed to remove any remaining porosity of the consolidated billets and to improve mechanical properties. However, how to retain the fine grain size at high temperature is a challenge.

### **2.1.1.3 Severe plastic deformation**

Severe plastic deformation (SPD) is an approach that refines the grain structure by plastically deforming the materials to a very large strain (up to some thousands percent) [Ros05, Val00]. NC materials produced by SPD are reportedly 100% dense, contamination-free, and sufficiently large for use in real commercial structural applications. These materials are found to have high strength, good ductility, superior superplasticity, a low friction coefficient, high wear resistance, enhanced high cycle fatigue life, and good corrosion resistance. However, samples produced by SPD have drawbacks of a lower limit of grain refinement (about 50 nm) and wide grain size distribution. Several SPD processing methods are now available, but the most important two are equal-channel angular pressing (ECAP) [Höp02] and high-pressure torsion (HPT) [Bar01, Val93, Zhu04], which appear to have the greatest potential for industrial applications.

### **2.1.1.4 Electrodeposition**

Electrodeposition (ED) is an electrode reaction which involves oxidation/reduction of a solid metal and its dissolved ion. The process can be considered as a special form of grain boundary engineering in which the grain boundary content (types and quantities of grain boundaries) of a material are controlled during material processing to achieve certain physical, chemical and mechanical properties [Aus93]. The basic components required for electrodeposition are an

anode, cathode, electrolyte and current source.

ED (direct current or pulsed) has the capability to produce fully dense NC materials in a single-step process. The grain size of the specimen can be controlled by changing the physical deposition parameters (current density, current characteristics) and the chemical deposition parameters (grain refiners, complex formers) [Nat98]. ED has been used to produce NC materials such as pure metals, alloys, composites, and ceramics with grain sizes less than 100 nm and thickness more than 4 mm. Literature contains numerous examples giving electrochemical processing windows for the synthesis of NC pure metals (Ni, Co, Pd and Cu) [Bak93, Nat96] and alloys (Ni-P, Ni-Fe, Ni-Fe-Cr) [Des87, Nat98]. Even multilayered structures or compositionally modulated alloys (Cu-Pb, Cu-Ni), metal matrix composites (Ni-SiC) and ceramics (ZrO<sub>2</sub>) have been successfully produced by ED methods [Erb93, Shi93].

### 2.1.2 General characteristics

1. Small grain size: grain size is in the nanometre range, e.g. 1–10 nm [Sur92, Lu01], or 10–1000 nm [Sax02], but the most widely accepted range of grain size is less than 100 nm in at least one dimension [Sie93].
2. High interfacial area/volume ratio: the volume fraction of interfacial atoms can be as high as 50% for grain size of 5 nm estimated by Mutschele and Kirchheim [Mut98]. A maximum volume fraction of 50% was also reported for grain size of 3 nm by Wang et al. [Wan93]. This high volume fraction of interfacial atoms has been attributed to the formation of triple lines and then to the quadruple nodes, i.e. the intersection of (usually four) triple lines in the grain boundary region [Pal90]. Due to the high percentage of grain boundary atoms, NC materials can be viewed as a ‘composite’ of grains with normal lattice atoms and the grain boundary region comprising atoms with different interatomic spacing [Wan93, Sio04].
3. Unclear grain boundary structure: some studies on grain boundary structures in NC materials showed that the atoms in grain boundaries are in a totally disordered state [Zhu87, Hau89, Wür87], whereas other studies [Fit91, Eas92] have revealed that the

structure of the grain boundaries in NC materials is close to that in conventional polycrystalline materials.

4. Process dependent grain boundary angels: high angel grain boundaries are always found in milled NC materials and materials produced by SPD [Val97], while low angel grain boundary are always reported for electrodeposited NC materials [Lu00, Ebr99].

## 2.1.3 Mechanical properties

### 2.1.3.1 Elastic modulus

The elastic modulus of a material is related to the atomic binding forces and characterizes the elastic response of a material under loading. Different arrangements of atoms will result in different bond strength and finally different elastic moduli. As shown before, NC materials have a high interfacial area/volume ratio. The arrangement of atoms in the grain boundary region is different from that within the grains, therefore, it is expected that the elastic moduli of NC materials will vary with the grain size.

Early measurements showed lower values of the elastic modulus  $E$  for NC materials compacted from powders than for conventional materials [Niem91]. It was suggested that the presence of extrinsic defects — pores and cracks, for example — was responsible for the low values of  $E$  in NC materials [Krs93, San97]. Computational analysis with phase mixture model predicted the reduction of elastic modulus with an increase of porosity for NC Cu [Kim99]. Subsequent work on nearly porosity-free materials has shown that the intrinsic elastic modulus of NC materials is essentially the same as those for conventional materials [Zhou03]. Molecular dynamic simulations showed that a reduction of the elastic modulus occurs only if the grain size is smaller than 10 nm [Wee99]. As the grain size becomes very small (e.g.  $< 5$  nm), the number of atoms associated with the grain boundaries and triple junctions becomes very large and the elastic properties in this case are not very clear yet. For example, NC NiP produced by electroplating with negligible porosity levels had a reduced elastic modulus with decreasing grain size in the range 5–10 nm [Zhou03], similar results were reported on NC Fe prepared by mechanical alloying and measured by a nanoindentation technique [Shi93].

Even removing the other factors such as methods of the sample production and experimental

techniques, there are still divided results on the elastic modulus of NC materials. It seems the unusual elastic properties of NC materials are due to both the small grain size and the grain boundary state.

### **2.1.3.2 Hardness and yield strength**

NC materials typically exhibit significantly higher hardness and yield strength relative to their MC counterparts. This is in good agreement with the H-P relationship. However, different H-P slope values were observed as the grain size becomes smaller, including:

1. Positive slope (normal H-P behavior)
2. Zero slope (no grain size dependence)
3. Negative slope (“inverse H-P behavior”) [Kna04, Gut01, Mor97, Mas98]

Carl C. Koch and J. Narayan point out that most experiments that show the negative H-P slope at the smallest grain sizes are performed on NC samples that have been annealed to increase their grain size [Koc01]. It is suggested that thermal treatment of NC materials in the as-produced condition may result in such changes in structure as densification, stress relief, phase transformations, or grain boundary structure, all of which may lead to the the observed negative H-P behavior. However, there are reports of the inverse H-P behavior where no obvious artifacts or other problems, like that caused by heat-treatment, exist [Erb95, Alv96]. Therefore, more effort has to be done to explain the observed different H-P behaviour in NC materials.

### **2.1.3.3 Reduced ductility**

For MC materials, grain size refinement can make crack nucleation more difficult and therefore increase the fracture toughness and yield strength. With the same decrease of grain size, the fracture strength increases more than the yield strength, and the materials get more ductile. Based on this experience with MC materials, the ductility should increase as the grain size goes down to the nanoscale regime. However, experimental data have not verified this predicted trend. On the contrary, NC materials typically exhibit significant higher yield strength but

reduced tensile elongation at fracture relative to their conventional MC counterparts. Examples for this observation could be found in NC Cu, Ni and Pd [Rob99, Niem91].

One of the reasons for the lower ductility of NC materials may be due to the present processing defects such as porosity. Nieman et al. [Niem90] demonstrated that the density after powder compaction and the surface finish greatly influence the ductility data. Very limited ductility was observed even for the samples with density greater than 98% of the theoretical density. In other related studies, a short elongation of 0.3% in the NC alloys (processed by compaction of inert-gas condensation) were reported [Rit97]. The other reason may be due to the nature of deformation process in terms of shear banding [Ebr98] or localized necking [Niem91]. A universally accepted view of this point has not been achieved yet. It is notable that NC specimens with bimodal distribution of grain size always exhibit higher ductility. For example, Wang et al. [Wan02] reported that Cu specimens with a bimodal grain size distribution show a high tensile ductility (65%).

### 2.1.3.4 Enhanced diffusional creep

There are two important parameters, grain size and diffusivity, which affect strongly the creep behaviour of a polycrystalline material. By increasing diffusivity and/or reducing the grain size, the creep rate of a polycrystalline material can be enhanced. For example, in the case of the Coble model and grain boundary sliding model, the creep rate depends on the third power of the mean grain size. Going from a grain size of 1  $\mu\text{m}$  to 10 nm should increase creep rate  $\dot{\epsilon}$  by  $10^6$  or more if the diffusivity of grain boundary is significantly larger for NC materials [Gus98]. With respect to the diffusivity, some experimental work [Hor87, Pal90] has shown that the self-diffusivity in NC materials is much higher (about  $10^3$  times for NC Cu) than that in conventional CG counterparts. With high diffusivity and nanometer grain size, NC materials are expected to creep at room temperature.

The presence of diffusional creep at room temperature was cited as the reason for the grain size softening effect in NC Cu [Cho89]. This suggestion was tested by Yamakov et al. [Yam02a] by performing MD simulations of NC Pd with a grain size of up to 15.2 nm. The results reveal that the onset of steady-state creep is characterized by constant strain rates. These rates were found to increase linearly with the applied stress for the entire range of grain sizes and

temperatures investigated, consistent with the well-known Coble-creep. In addition, “Interface controlled diffusional creep” of NC Cu with an average grain size of 30 nm at low temperatures ( $0.22\text{--}0.24 T_m$ ) was reported by Cai et al. [Cai99]. Wang et al. [Wan97] studied the room temperature creep behaviour of electrodeposited NC Ni with grain size 6–40 nm, and their results show that grain boundary sliding and diffusive matter transport play an important role. Other studies show that even brittle ceramics or intermetallics at low temperatures exhibit certain amount of ductility with NC grain structures [Bon91, Kar87]. These observations were suggested to be attributed to enhanced diffusional creep providing the plasticity at these temperatures, where conventional materials would fail in a brittle way. However, the results above have not been reproduced; in addition, creep measurements of NC Cu, Pd and Al-Zr at moderate temperatures showed creep rates comparable or even lower than corresponding rates of coarse-grained counterparts [Niem91]. In sum, the enhanced diffusional creep predicted in NC materials at low temperatures need to be further studied.

### 2.1.3.5 Improved superplasticity

Superplasticity is the capability of some polycrystalline materials to exhibit very large tensile elongation at particular temperatures and strain rates without necking or fracture. The defining elongation is typically from 100% to >1000%. This phenomenon is generally observed in materials with grain sizes less than 10  $\mu\text{m}$  in the temperature range  $0.5\text{--}0.6 T_m$  and at a strain rate of  $10^{-3}\text{--}10^{-4} \text{ s}^{-1}$  [Nie97]. For NC materials, owing to their fine grain size, large grain boundary area and high self-diffusivity, superplasticity is expected at lower temperatures and/or higher strain rates. Superplasticity was observed in a number of NC materials using miniature tensile specimens [McF99]. NC nickel was found to be superplastic at a temperature 734 K corresponding to  $0.36 T_m$ . Lu et al. [Lu00] attained superplasticity by rolling electrodeposited NC pure copper at room temperature, causing a very high extensibility (elongation exceeding 5000%) without a strain-hardening effect.

## 2.2 A general introduction to plastic deformation

### 2.2.1 Dislocation glide and climb

Dislocations are line defects that glide through a crystal lattice with an applied stress. There are typically two types of dislocations, edge dislocations and screw dislocations. A dislocation is characterized by its Burgers vector. An edge dislocation lies perpendicular to its Burgers vector, while a screw dislocation lies parallel to its Burgers vector.

Dislocation slip is the most common mechanism of deformation in crystalline solids. The slip plane of a dislocation is defined as the plane that contains both the dislocation line and its Burgers vector. Dislocations initially glide along the closest packed planes in the closest packed directions since this requires the lowest energy or applied stress. Screw dislocations have a Burgers vector parallel to the dislocation line, therefore they can glide on any close packed plane containing the dislocation line and the Burgers vector, whereas edge dislocations can only slip on the plane defined by the dislocation line and the perpendicular Burgers vector.

Climb is another movement method of edge dislocation and fundamentally different from slip. This process involves a motion perpendicular to the slip plane and requires vacancies movement through the lattice. It only occurs at comparatively high temperatures because of the temperature dependence of the necessary diffusion.

### 2.2.2 Thermal activation of dislocation

Many objects, such as precipitates, point defects or other dislocations can impede dislocation motion. If the applied stress is not large enough to push the dislocation through the obstacle, an additional energy must be supplied by a thermal fluctuation to overcome the resistance. Fig. 2.1 shows a mobile dislocation passing through obstacles (dislocation trees in this case) under an applied stress  $\sigma$ . The constant  $U_0$  represents the value of this additional energy when no stress is applied to the crystal, then the activation energy  $\Delta G$  needed to overcome the obstacles must be supplied by thermal fluctuations and is given by:

$$\Delta G = U_0 - \sigma V_a \quad (2.1)$$

where  $V_a$  is the activation volume and can be written as:

$$V_a = l'_0 \cdot d' \cdot b \quad (2.2)$$

where  $l'_0$  is the distance between the trees,  $d'$  the distance the dislocation must move before the tree is cut and  $b$  the Burgers vector of the mobile dislocation as shown in Fig. 2.1. A glide

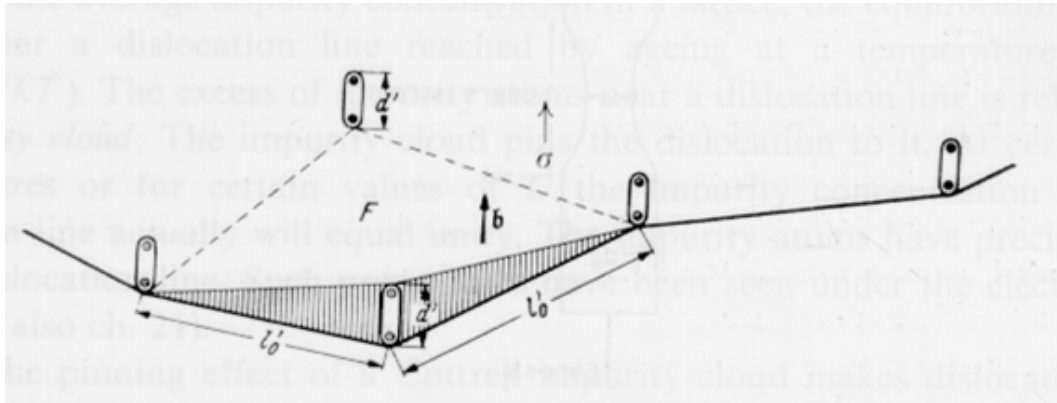


Figure 2.1: A mobile dislocation hung up on dislocation trees [Cah83].

resistance diagram is shown in Fig. 2.2. A dislocation travelling from the left to the right under a positive force would be in static equilibrium at position  $S$  (stable). A finite increment of area further on would be a second equilibrium position  $U$  (unstable). If the thermal fluctuations transferred the dislocation from  $S$  to  $U$ , it would be again under positive driving stress. The difference in energy between the stable and unstable equilibrium states at the given stress and temperature is the activation energy  $\Delta G$  supplied by thermal fluctuations needed to overcome the obstacles [Koc75].

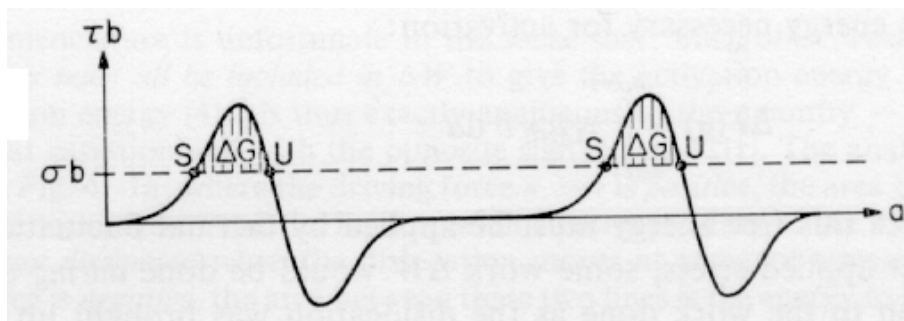


Figure 2.2: A glide resistance diagram [Koc75].

When the process is thermally activated, the strain rate  $\dot{\epsilon}$  related to the applied stress  $\sigma$  can be described by an Arrhenius-type equation:

$$\dot{\epsilon} = \dot{\epsilon}_0 \exp\left(-\frac{\Delta G}{k_B T}\right) \quad (2.3)$$

where  $k_B$  is the Boltzmann constant, and  $\dot{\epsilon}_0$  is always taken to be a constant. It is customary to use such an expression in conjunction with the experiment to define the activation energy  $\Delta G$  and activation volume  $V$  in terms of variations in strain rates with temperatures and stress [Cah01]:

$$\Delta G(\sigma) = k_B T \left. \frac{\partial \ln \dot{\epsilon}}{\partial \ln T} \right|_{\sigma} \quad (2.4)$$

and

$$V = k_B T \left. \frac{\partial \ln \dot{\epsilon}}{\partial \sigma} \right|_T \quad (2.5)$$

Another primary material parameter of interest is the strain rate sensitivity (SRS)  $m$  for the flow stress defined as:

$$m = \left. \frac{\partial \ln \sigma}{\partial \ln \dot{\epsilon}} \right|_T \quad (2.6)$$

### 2.2.3 Creep

Creep is the plastic deformation proceeding at constant stress or at constant load and constant temperature in time [Cad88].

In a creep test a constant load is applied to a tensile specimen at a constant temperature, and the strain is then measured over a period of time. The graphical representation of the time–strain relation is known as creep curve, as schematically shown in Fig. 2.3. The creep curve normally includes three stages. Stage I is the primary or transient creep stage, in which the creep rate decreases with time. Stage II is the steady-state or secondary creep stage, in which the creep rate is time invariant. Stage III is the tertiary creep stage, in which the creep rate increases with time and finally terminates in fracture.

Different creep mechanisms are responsible for the deformation depending on the material and the different loading and temperature conditions. There are three basic mechanisms that can contribute to creep in metals: diffusion creep, grain boundary sliding and dislocation creep.

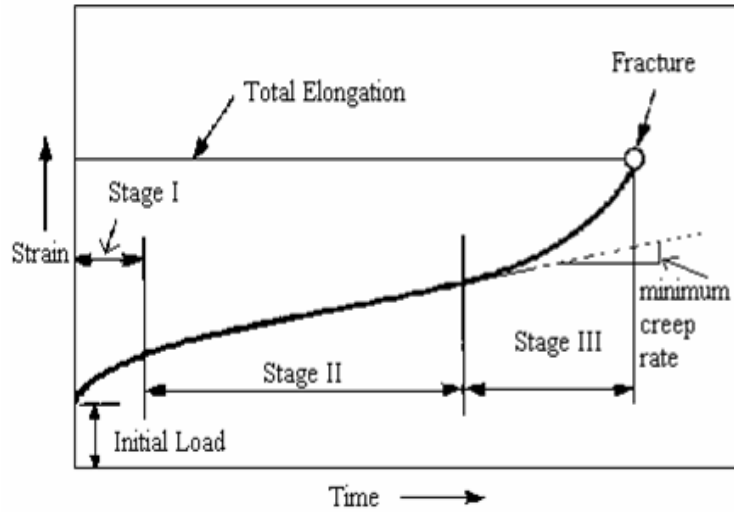


Figure 2.3: Schematic representation of a creep curve [Cad88].

- Diffusion creep: diffusion creep is one of the most common deformation mechanisms in engineering materials. Following the idea first proposed by Nabarro [Nab48] and Herring [Her50], then further developed by Coble [Cob63], deformation occurs by a diffusive matter transport through the individual grains and/or along grain boundaries of a stressed polycrystal. For a given applied stress  $\sigma$  and grain size  $d$ , the creep rate  $\dot{\epsilon}$  (or  $d\epsilon/dt$ ) is expressed as:

$$\dot{\epsilon} = 14 \frac{\Omega \sigma}{k_B T d^2} D_L \left( 1 + \frac{\pi \delta}{d} \frac{D_{gb}}{D_L} \right) \quad (2.7)$$

where  $\Omega$  is the vacancy volume,  $k_B$  the Boltzman constant,  $T$  the absolute temperature,  $\delta$  the thickness of the grain boundary,  $D_L$  and  $D_{gb}$  the coefficients of lattice and grain boundary diffusion, respectively.

- Grain boundary sliding: as a further diffusive mechanism acting in parallel to Nabarro-Herring and Coble creep, Gifkins [Gif68] proposed the so-called grain boundary sliding mechanism, which is either controlled by lattice or grain boundary diffusion. The creep rate  $\dot{\epsilon}$  is given by [Lüt79]:

$$\dot{\epsilon} = 2 \times 10^5 D_{gb} \frac{\mu b}{k_B T} \left( \frac{b}{d} \right)^3 \left( \frac{\sigma}{\mu} \right)^2 \quad (2.8)$$

for grain boundary diffusion controlled grain boundary sliding or

$$\dot{\epsilon} = 8 \times 10^6 D_L \frac{\mu b}{k_B T} \left(\frac{b}{d}\right)^2 \left(\frac{\sigma}{\mu}\right)^2 \quad (2.9)$$

for lattice diffusion controlled grain boundary sliding, where  $\mu$  is the shear modulus,  $b$  the Burgers vector and the other parameters are the same as in equation 2.7. In contrast to the linear stress dependence of creep rate in the diffusion mechanism of equation 2.7, in this case the creep rate exhibits a second-power stress dependence due to grain boundary sliding, i.e.  $\dot{\epsilon} \propto \sigma^2$ .

- Dislocation creep: dislocation glide-and-climb also leads to creep. The dislocation creep rate can be described by the so-called power-law relation [Ash72]:

$$\dot{\epsilon} = 3.83 \times 10^5 D_L \frac{\mu b}{k_B T} \left(\frac{\sigma}{\mu}\right)^n \quad (2.10)$$

where the value of  $n$  varies from 3–8.

## 2.2.4 A general survey of the deformation mechanisms – Ashby maps

The most important mechanism of plastic deformation is dislocation glide. In the course of plastic deformation taking place by this mechanism at relatively low homologous temperatures and high strain rates, the dislocation density increases, which manifests itself by increasing flow stress with strain.

When the homologous temperature  $T/T_m$  at which plastic deformation takes place is higher than about 0.4, dynamic recovery, a phenomenon which is unimportant or only slightly significant at low homologous temperatures and high strain rates, starts to play an important role. The dynamic recovery compensates, to an extent depending on temperature and strain rate, the effects of deformation strengthening. Recovery during plastic deformation can occur by various mechanisms. The most important mechanism obviously involves non-conservative motion of dislocations — climb — and annihilation of dislocations, and depends therefore on diffusion which can occur either via the lattice (higher homologous temperatures) or via dislocations cores (lower homologous temperatures).

At homologous temperatures higher than about 0.4, grain boundaries represent a system of glide planes which generally becomes active simultaneously with crystallographic glide systems within the grains. Thus, under an applied stress, grain boundary sliding takes place and this naturally contributes to the plastic strain. The grain boundary sliding causes extreme heterogeneity of plastic deformation at temperatures where it takes place to a significant extent. This can lead to a reduction in the polycrystal compatibility by formation of voids on grain boundaries if grain boundary sliding is not accommodated by intergranular deformation either due to dislocation glide or by diffusion creep. Diffusional creep can take place by diffusion of vacancies either via lattice (Nabarro-Herring creep) or via grain boundaries (Coble creep).

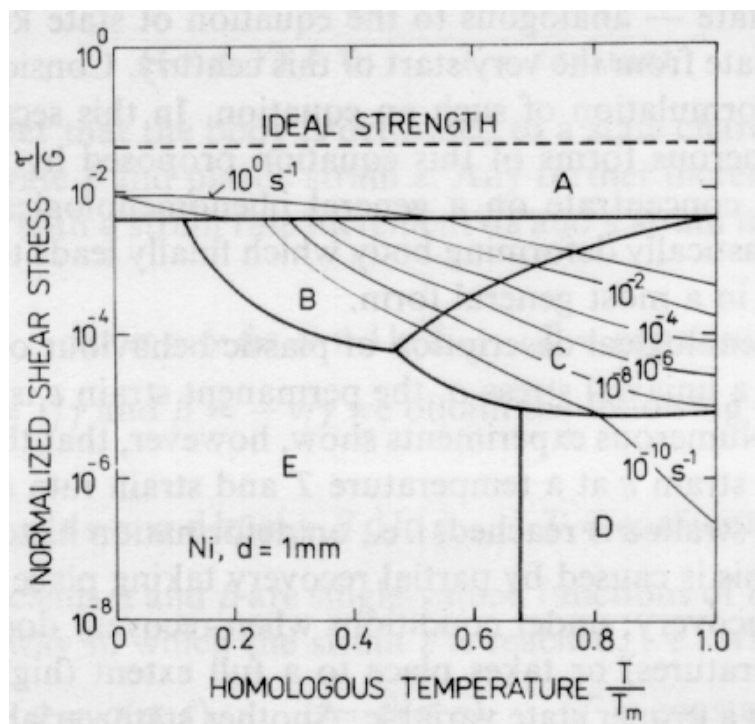


Figure 2.4: Example of a deformation map of pure nickel with mean grain diameter  $d = 1 \text{ mm}$ .

Field A - dislocation glide without participation of recovery; Field B - dislocation creep, dislocation core diffusion; Field C - dislocation creep, lattice diffusion; Field D and E - diffusion Nabarro-Herring and Coble creep, respectively. The curves of constant strain rates are shown on the map [Cad88].

An idea about which of the possible mechanisms dominates is provided by the deformation maps introduced by Ashby [Ash72]. The construction of deformation maps is based on the

assumption that all the deformation mechanisms considered are mutually independent, thus operate in a parallel way. It is also based on an application of constitutive equations describing the stress, temperature, grain size and stacking fault energy dependence of creep rates due to individual mechanisms. An example is shown in Fig. 2.4. The map is constructed for a given mean grain diameter in logarithmic coordinates: the stress normalized to the shear modulus,  $\sigma/\mu$ , and the homologous temperature  $T/T_m$ . On the top, the map is bounded by the theoretical or ideal strength (the normalized theoretical strength is equal to  $5 \times 10^{-2}$ ). At stresses somewhat lower than the theoretical strength, the deformation takes place by dislocation glide without participation of recovery — Field A in Fig. 2.4. The fields B (dislocation core diffusion) and C (lattice diffusion) represent regions of external conditions under which dislocation creep prevails; the fields D and E represent regions of external conditions under which the Nabarro-Herring and Coble creep dominate, respectively.

## 2.3 Explanations of the Hall-Petch relation

In general, many mechanical properties of polycrystalline metals, including yield strength and hardness, can be improved by refining the grain size at low temperatures. The values of typical mechanical properties increase with the reciprocal root of the grain size, known as the H-P effect. There are many models to interpret H-P relation [Mor01]. Among them, the best known and mostly cited are the dislocation pile-up model [Mey82, Hir92] and the dislocation density model [Cot53, Oro54].

### 2.3.1 Dislocation pile-up model

As shown in Fig. 2.5, it is considered that a dislocation source is activated and dislocations pile up against a grain boundary under an effective shear stress  $\tau_e$ :

$$\tau_e = \tau - \tau_0 \tag{2.11}$$

where  $\tau$  is the applied stress and  $\tau_0$  is a local correction due to friction and back stress. It can be shown that the stress at the head of the pile-up is:

$$\tau_p = n\tau_e \tag{2.12}$$

where  $n$  is the number of dislocations contained in the pile-up. If the pile-up has the length  $L$ , then the number of dislocations is also determined by effective stress  $\tau_e$ :

$$n = \frac{q\pi L\tau_e}{\mu b} \quad (2.13)$$

where  $\mu$  is the shear modulus and  $q$  is a geometric factor of order unity. Yielding is assumed to occur when the stress at the tip of the pile-up  $\tau_p$  reaches the critical value  $\tau_c$ , which is necessary to nucleate slip across the grain boundary. At this point,

$$\tau = \tau_y = \tau_0 + \left(\frac{\mu b \tau_c}{q\pi L}\right)^{0.5} \quad (2.14)$$

The pile-up length  $L$  can not be larger than the grain size  $d$  and is usually taken to be  $d/2$ , so equation 2.14 has the same form of  $\tau_y = \tau_0 + kd^{-0.5}$ .

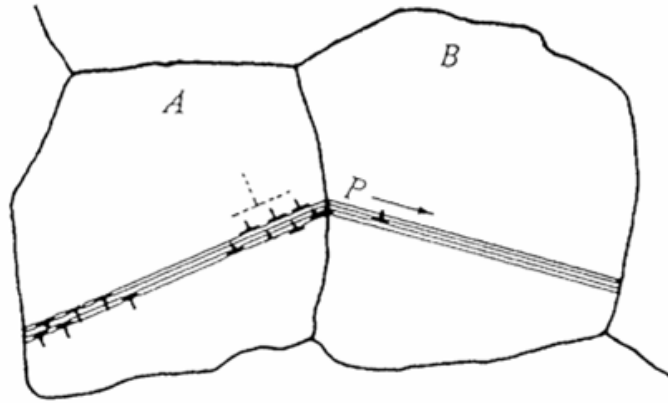


Figure 2.5: Pile-up of dislocations at grain boundaries.

### 2.3.2 Dislocation density model

This model is based on the correlation between grain size and dislocation density at yield. In the simple hardening models, the critical resolved shear stress to move a dislocation through a distribution of dislocations varies with the dislocation density  $\rho$ , as:

$$\tau_c = \tau_0 + \alpha\mu b\sqrt{\rho} \quad (2.15)$$

where  $\alpha$  is a factor in the range 0.1–0.3. An increasing body of evidence suggests that this basic hardening law applies widely to the deformation of metals, beginning from the yield strength.

If this is true and the H-P relation also holds at yield, the dislocation density at yield ( $\rho_y$ ) must be determined by the reciprocal grain size according to the relation:

$$\rho_y = \left(\frac{k_y}{\alpha\mu b}\right)^2 \left(\frac{1}{d}\right) \quad (2.16)$$

To justify a behaviour like that in equation 2.16, Li et al. [Li63, Li70] proposed that grain boundaries could act as dislocation sources and the dislocation density within the grain might be determined by sources located in the boundary. If these are distributed with a constant mean areal density, the number of dislocations within the grain ( $n$ ) would be proportional to the grain boundary area  $cd^2$ , where  $c$  is a constant that depends on the shape of grain. It follows that the dislocation density is:

$$\rho = \frac{n}{V} = \frac{cd^2}{d^3} = \frac{c}{d} \quad (2.17)$$

More recent interpretations have been based on the distribution of “geometrically necessary dislocations (GNDs)” that are required to assure compatible strain across grain boundaries [Jia95, Ash71]. The number of GNDs needed to accommodate a given misorientation across a boundary is proportional to the area of boundary. Hence the expected number of GNDs within a grain, after a given strain should be proportional to the grain boundary area, as in equation 2.17, again giving a dislocation density that increases with the reciprocal grain size [Mor01].

## **2.4 Grain boundary mediated deformation mechanisms in nanocrystalline metals**

### **2.4.1 Nucleation of dislocations and stacking faults from grain boundaries**

Theoretically the conventional dislocation sources such as the Frank-Read source cease to operate as grain size decreases down to a critical value. For face-centered-cubic (fcc) metals, which have been the object of most studies, it appears that the critical grain size is around 30 nm [Che03]. Around this critical grain size, grain boundaries act as dislocation sources or sinks. Partial and perfect dislocations are found being nucleated from either existing grain boundary dislocations or sources of stress concentration at grain boundaries, as schematically shown

in Fig. 2.6 [Asa05]. The deformation process of dislocation activity observed in molecular dynamics (MD) simulations is initiated by a Shockley partial nucleated from the grain boundary [Fro04]. If no other partial is emitted from the grain boundary, the initial single partial will travel across the entire grain cross-section to be absorbed in the opposite grain boundary, leaving behind an extended stacking fault that transects the entire grain. If the single partial dislocation is followed by the nucleation of a trailing partial dislocation at the same slip plane, a full dislocation is formed [Van99, Van02, Yam04]. The stacking faults resulted in the grain impede the movement of dislocations and thus strengthen the materials. For fcc metals the

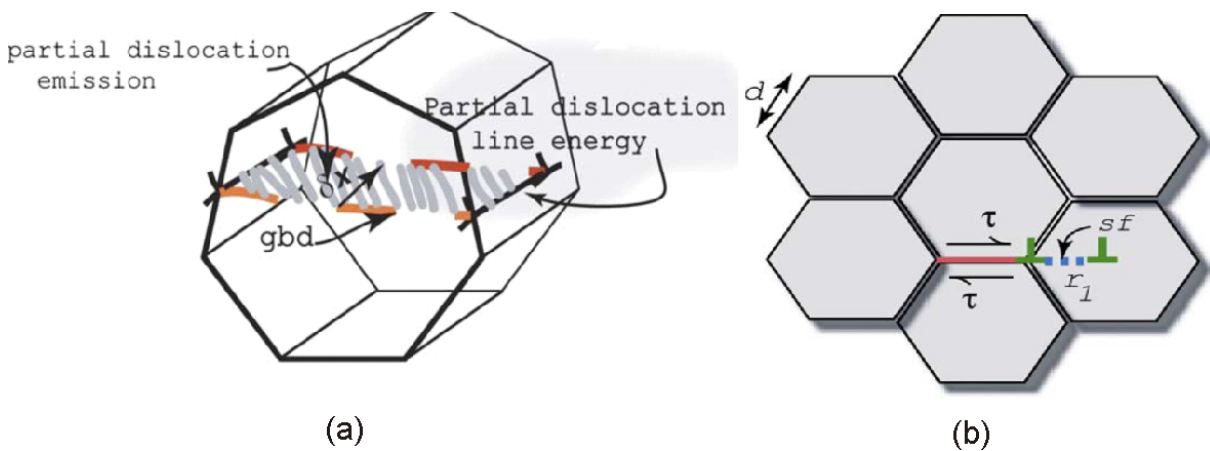


Figure 2.6: Emission of a partial dislocation followed by stacking fault from grain boundaries. (a) Emission of a partial dislocation into the grain from an exiting grain boundary dislocation; (b) Emission of a partial dislocation into the grain from a concentration on the grain boundary [Asa05].

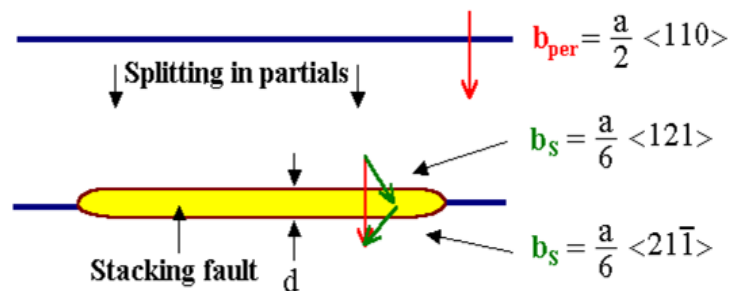


Figure 2.7: Perfect dislocation splits into Shockley partials connected by a stacking fault [Www01].

most common dislocations responsible for the slip deformation are extended dislocations with their cores being split into two Shockley partials connected by a stacking fault (see Fig. 2.7). In NC metals, the criteria whether a full dislocation will form from the grain boundary or not is not clear. Yamakov et al. [Yam04] use the splitting distance of an existing full dislocation as a critical parameter for the determination of a grain size below which no full dislocations will exist. Other studies show that aside from stacking fault energy alone, the unstable stacking energy plays an important role in determining the critical condition for the emission of a partial as well as a full dislocation [Van02, Van04].

### 2.4.2 Emission of deformation twins from grain boundaries



Figure 2.8: Emission of a leading partial dislocation with Burgers vector  $b^1$  followed by the emission of a second leading partial dislocation (having a different Burgers vector  $b^1$ ) on an adjacent slip plane, thus creating a deformation twin. The darker shaded region denotes an intrinsic stacking fault and the lighter region a deformation twin. The left side of the figure extends to the boundary from which the fault/twin was emitted. TP means twin plane [Asa05].

Deformation twinning, as an alternate mode of deformation, has been experimentally found in NC Al [Che03a, Yam02], Cu [Lia04] and Pd [Mar04] at different grain sizes. TEM studies revealed that below a critical grain size of the order of 10–20 nm, deformation twinning becomes an important deformation mode, although deformation twinning has never been seen in CG samples with nominally high stacking fault energy.

Regarding the mechanical twinning of fcc metals, several models have been proposed in which deformation twins are created by stacking faults led by  $1/6[112]$  Shockley partials [Yam02, Lia03, Wol05]. The process is shown in Fig. 2.8. A Shockley partial is nucleated from the grain

boundary followed by a stacking fault. If a trailing partial is nucleated from the grain boundary onto the adjacent slip plane instead of the same slip plane as the first one, a micro-twin is formed. The creation of such a micro-twin corresponds to the onset of deformation twinning. The model implies that deformation twinning occurs when the grain boundaries start to emit more partial dislocations than perfect ones.

### 2.4.3 Transformation of grain boundary dislocation pile-ups at triple junction

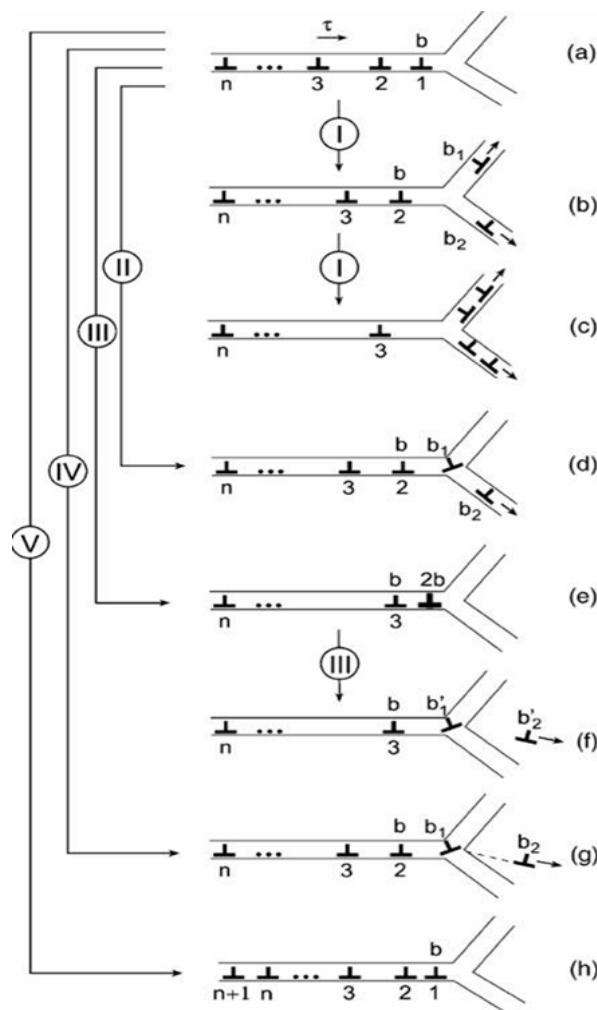


Figure 2.9: Transformations of grain boundary dislocation pile-ups at triple junctions [Fed03].

Transformation of grain boundary defects influences strongly both the structure and the prop-

erties of solids, particularly, the grain boundary sliding which occurs via motion of grain boundary dislocations crucially affects the deformation behaviour of polycrystalline materials. The features of grain boundary sliding depend strongly on triple junctions. NC materials are commonly synthesized at highly non-equilibrium conditions that cause many grain boundary dislocations and the volume of triple junctions is extremely high.

A theoretical model which describes several types of transformations of grain boundary dislocation (GBD) pile-ups was suggested by Fedorov et al. [Fed03]. Consider a GBD pile-up generated in a grain boundary of a plastically deformed NC or polycrystalline sample. When the motion of the GBD pile-up is stopped by a triple junction of grain boundaries (Fig. 2.9a), the authors suggested five basic ways of evolution of the GBD pile-up under this circumstance:

1. The head dislocation (with Burgers vector  $b$ ) of the pile-up splits into the two dislocations (with Burgers vectors  $b_1$  and  $b_2$ , respectively) that move along the adjacent grain boundaries (Fig. 2.9b). This process may repeatedly occur resulting in the consequent splitting of even all the dislocations that compose the pile-up (Fig. 2.9c).
2. The head dislocation of the pile-up splits into an immobile GBD with Burgers vector  $b_1$ , which stays at the triple junction, and a mobile GBD with Burgers vector  $b_2$ , which moves along one of adjacent grain boundaries (Fig. 2.9d).
3. Two (or more) GBDs each is characterized by Burgers vector  $b$  converge into a dislocation with Burgers vector  $2b$  having magnitude close to the crystal lattice parameter (Fig. 2.9e). Then the resultant dislocation splits into a mobile lattice dislocation with Burgers vector  $b'_2$ , which moves to the adjacent grain interior, and an immobile GBD with Burgers vector  $b'_1$ , which stays at the triple junction (Fig. 2.9f).
4. The head dislocation of the pile-up splits into an immobile GBD (with Burgers vector  $b_1$ ) that stays at the triple junction and a mobile partial dislocation (with Burgers vector  $b_2$ ) that moves in grain interior, in which case a stacking fault is formed behind the moving partial dislocation (Fig. 2.9g).
5. The pile-up is immobile. It accumulates new GBDs generated under the action of mechanical load (Fig. 2.9h). This process precedes one of the processes (1–5).

GBD pile-ups serve as stress concentrators. The processes of their splitting give rise to a decrease of the stress concentration and therefore, hamper fracture. In doing so, the geometry of the splitting of GBD pile-ups strongly influences the grain boundary sliding as a channel of plastic deformation. The triple junctions are distinguished as the so-called “soft” and “hard” ones, depending on at which whether the dislocation pile-up splitting occurs or not at the given conditions of loading. The ratio of the volume fraction of soft triple junctions  $F_s$  to the volume fraction of hard junctions  $F_h$  effectively characterizes the contribution of grain boundary sliding to plastic deformation. With a theoretical analysis the authors [Fed03] pointed out that the competition between grain boundary sliding and other deformation mechanisms is crucially influenced by the ratio  $F_s/F_h$ . Materials with a high ratio  $F_s/F_h$  exhibit enhanced grain boundary sliding characterized by the yield stress value being lower than the yield stress values specifying alternative deformation mechanisms, like diffusional creep mechanisms for instance. This means that plastic flow in materials with a low ratio  $F_s/F_h$  occurs by alternative deformation mechanisms, while grain boundary sliding is suppressed.

### 2.4.4 Grain boundary sliding and grain rotation

Grain boundary sliding occurs via motion of gliding grain boundary dislocations [Muk02] and plays a dominant role in the superplasticity in NC and MC materials. In NC Cu processed by high-pressure torsion, the elongated nanodomains finally transformed into equiaxed NC grains with large-angle grain boundaries, suggesting grain boundary sliding may play a significant role [Lia04]. Direct evidence for grain boundary sliding in NC materials was reported by Shan et al. [Sha04], who observed grain rotation in NC nickel films in a Transmission Electron Microscope.

A model of the crossover from the grain boundary sliding to the rotational mode of plastic flow in NC materials was proposed by Gutkin et al [Gut03]. In this model, a head grain boundary dislocation at a triple junction splitting into climbing grain boundary dislocations occurs repeatedly, resulting in the formation of two walls of dislocations and causing the crystal lattice rotation in the grain interior (Fig. 2.10).

In general, superplasticity also involves the conventional lattice dislocation slip, which provides accommodation for grain boundary sliding and on the other hand supplies grain boundary-

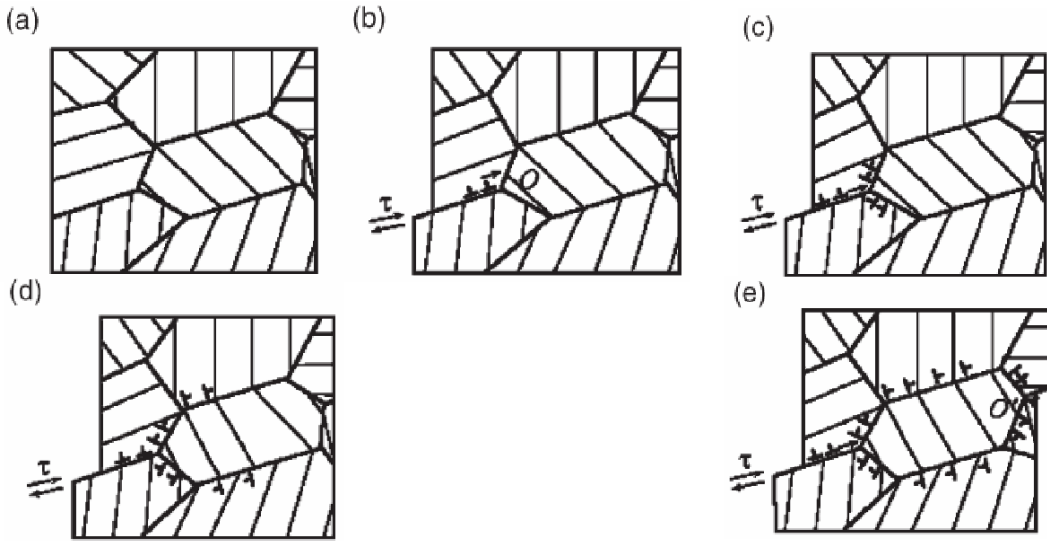


Figure 2.10: Combined action of grain boundary sliding and rotational deformation mode. (a) NC specimen in a non-deformed state; (b) grain boundary sliding occurs via motion of gliding grain boundary dislocations under shear stress action; (c) Gliding dislocations split at triple junction  $O$  of grain boundaries into climbing dislocations; (d) The splitting of gliding grain boundary dislocations repeatedly occurs causing the formation of walls of grain boundary dislocations whose climb is accompanied by crystal lattice rotation in a grain; (e) Climbing dislocations reach triple junction  $O'$  where they converge into gliding dislocations causing further grain boundary sliding [Gut03].

absorbed lattice dislocations. These grain boundary-absorbed lattice dislocations split into grain boundary dislocations being carriers of grain boundary sliding. Actually, lattice dislocations absorbed by grain boundaries commonly split into grain boundary dislocations of the two types: gliding and climbing grain boundary dislocations. The climbing dislocations absorbed by grain boundary also enhance a climb of grain boundary dislocations due to annihilation of climbing grain boundary dislocations along the boundary, as shown in Fig. 2.11.

The enhanced GBD climb stimulated by conventional dislocation slip causes the two following effects crucially important for superplasticity in NC materials:

1. plastic deformation is spread in the direction perpendicular to the direction of the maximum shear stress action;

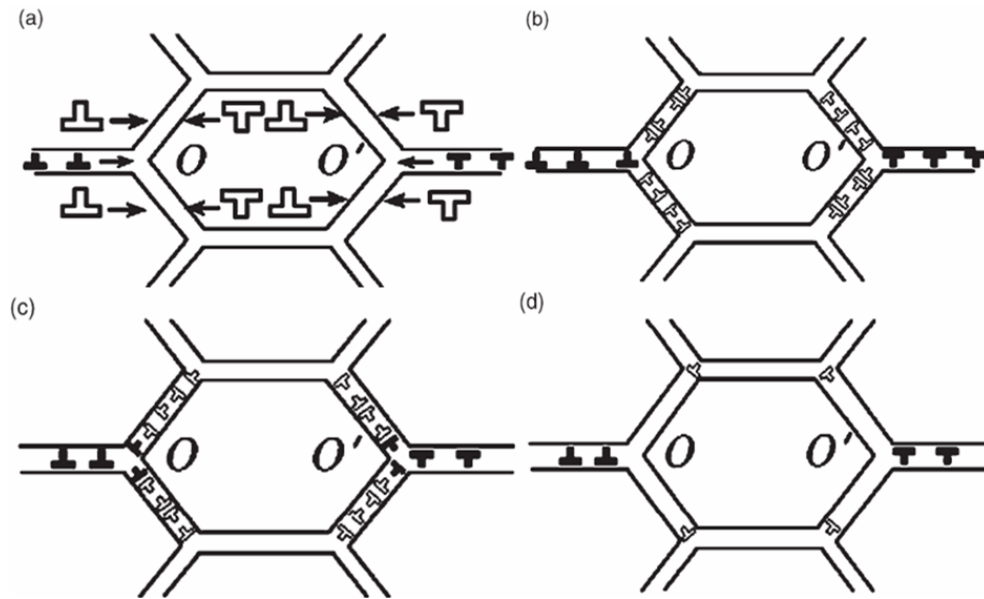


Figure 2.11: Enhancement of climb of grain boundary dislocations due to absorption of lattice dislocations. (a) Lattice dislocations (large open dislocation signs) and gliding boundary dislocations (small full dislocation signs) move under the shear stress action; (b) Climbing dislocations (small open dislocation signs) resulted from splitting of absorbed lattice dislocations form dipole configurations at grain boundaries; (c) Head grain boundary dislocations of pile-up split into climbing dislocations (full dislocation signs) at triple junctions  $O$  and  $O'$ ; (d) Annihilation of climbing dislocations forming dipole configurations results in the formation of isolated climbing dislocations highly distant from triple junctions  $O$  and  $O'$  [Gut03].

2. triple junctions with large abutting angles, that do not conduct grain boundary sliding, effectively conduct the crossover from the grain boundary sliding to the rotational mode. Therefore, these triple junctions do not serve as stress concentrators enhancing the nucleation of microcracks.

As a result of the above effects, neither plastic flow localization nor failure processes occur in a NC material, thus capable of sustaining large plastic deformations.

## 2.5 Methods of investigation

### 2.5.1 Atomistic simulations

Due to the extremely rapid increases in recent years in computer processor speed coupled with the development of larger parallel computing architectures, atomic-level simulations have begun to provide novel insights into the structure and thermo-mechanical behavior of NC materials. Simulations have recently advanced to a level where they provide a powerful new tool for elucidating – in a degree of detail not possible experimentally – the atomic-level mechanisms controlling the complex dislocation and grain boundary processes in heavily deformed materials with a submicron grain size. In particular, these simulations have now become large enough that they begin to capture the entire range of grain sizes where the transition from a dislocation to a grain boundary-based deformation mechanism occurs [Wol05].

Various atomic-level simulation methods have developed during the past decades, including lattice dynamics, Monte Carlo and molecular dynamics (MD) [Wol05]. Among which MD has been widely used for the investigation of plastic deformation of NC materials.

Besides being limited to relatively small model systems consisting of typically millions of atoms, the fundamental limitations inherent to the MD approach are well known, pertaining mainly to the reliability of the interatomic potentials used and the relatively short time period (of typically 10 ns, or about  $10^7$  MD time steps) over which the dynamics of the system can be probed. The interatomic force descriptions used in most MD simulations are of empirical or semi-empirical origin. Even with the advantage of being computationally extremely efficient, they are unable to fully capture the many-body nature of electronic bonding, particularly its complex, self-consistent variation as a function of local structure and chemistry in the vicinity of defects. The short time duration to which MD simulations are inherently limited is particularly relevant to the simulation of plastic deformation. As a consequence, such simulations always involve extremely high strain rates (of typically  $> 10^7 s^{-1}$ , corresponding to 1% strain in 1 ns), i.e. many orders of magnitude higher than in experiments.

In spite of these limitations, MD simulations have several unique features apart from their atomic-level spatial and temporal resolution. One is their ability to elucidate the behavior of a fully characterized, though usually idealized, NC model system in terms of the underlying in-

terfacial structure, driving forces and atomic-level mechanisms. Another arises from the ability to deform to rather large plastic strains, thus enabling the observation of deformation under very high dislocation densities. This enables identification of the intra- and intergranular dislocation and grain boundary processes in a deformation regime where they compete on an equal footing, thus providing atomic-level insights into the underlying mechanisms not available from laboratory experiments. Computational models have been developed in recent years to address the fundamental issue of nucleation and kinetics of defects in response to mechanical loading. In order to make direct correlations with experiments in a quantitative manner, many of these studies have focused on defect nucleation under conditions of nanoindentation of surfaces, which is a convenient experimental tool for quantifying local deformation.

Many useful results have been achieved by MD simulation, including: (I) identification of the atomic-level mechanisms for dislocation nucleation and annihilation at the grain boundaries [Fro04, Van97a, Gou01]; (II) the prediction and recent experimental verification of mechanical twinning in NC Al [Sor03] and Cu [Van04a]; (III) elucidation of the mechanistic reasons for the crossover from a dislocation to a grain boundary-based deformation mechanism with decreasing grain size [Yam03]; (IV) the observation of shear bands [Van02a] and fracture behaviour in NC metals [Far02, Has03]. Some examples are described below:

- Dislocation activities in NC copper

MD simulations of NC copper with grain sizes from 5 nm to 50 nm have been performed by Schiotz [Sch04]. Dislocations are constantly created at grain boundary sources, propagate through the grains and vanish at the opposite grain boundaries. Very few dislocations are created at in-grain sources such as Frank-Read sources. Many single Shockley partials are nucleated, leaving behind a stacking fault acting as weak barriers to the dislocation motion. Initially, dislocations arrive at grain boundaries and are absorbed by them, but when a number of dislocations have been absorbed, the back-stress prevents subsequent dislocations from entering the grain boundary, and a pile-up is formed, as shown in Fig. 2.12.

- Grain boundary sliding

Schiotz et al. [Sch98] simulated the molecular dynamics of crystals with grain sizes

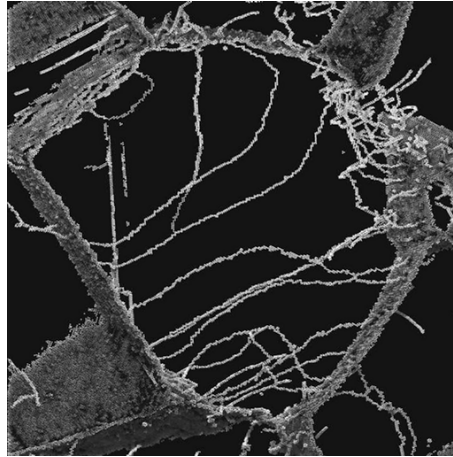


Figure 2.12: A pile-up formed in a nanograin. The dislocations move from the upper-left to the lower-right corner. A few dislocations, which are not part of the actual pile-up, are also seen on nearby slip planes [Sch04].

between 3.3 and 6.6 nm, using an interatomic potential model appropriate for copper sample containing 100,000 atoms. Their results show after 10% deformation, “most of the deformation occurs in the grain boundaries in the form of large number of small sliding events, where only a few atoms (or sometimes a few tens of atoms) move with respect to each other. Occasionally a partial dislocation is nucleated at a grain boundary and moves through a grain” (Fig. 2.13). They concluded that even in the absence of thermally activated processes, grain boundary sliding could operate and lead to the reverse H-P behavior.

- Deformation mechanism map for NC fcc metals

Based on MD simulation results, a deformation map was proposed by Yamakov and colleagues [Yam04]. This model identifies three regions of deformation behaviour depending on the grain size and stress level, both normalized by the stacking fault energy (Fig. 2.14). The map shows three distinct regions in which either complete extended dislocations (Region I) or partial dislocations (Region II), or no dislocations at all (Region III) exist during the low-temperature deformation of NC fcc metals. The crossover in the deformation mechanism arises from the length-scale competition between the grain size and the dislocation splitting distance  $r$ , which depends on the resolved shear stress  $\sigma$  and

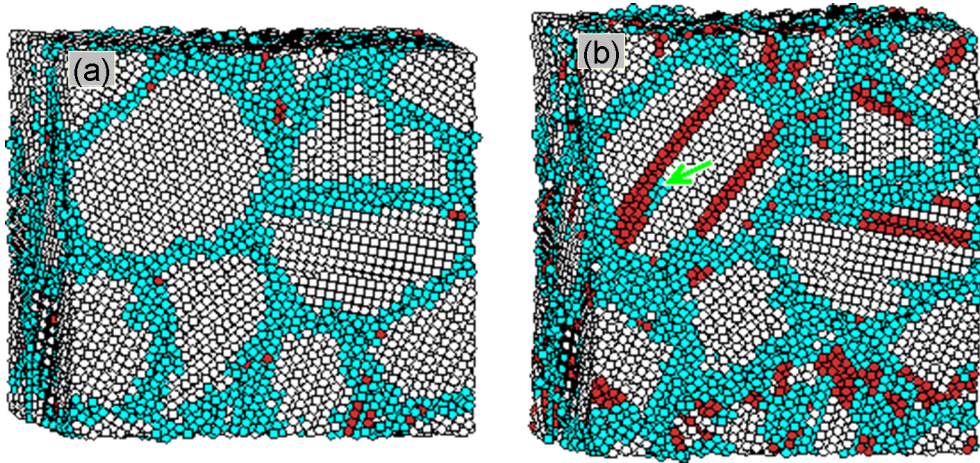


Figure 2.13: A simulated NC copper sample before (a) and after 10% deformation (b). The system contains 16 grains and approximately 100000 atoms, giving an average grain diameter of 5.2 nm. Atoms in the grain boundaries are colored blue, atoms at stacking faults are colored red. Stacking faults are left behind by partial dislocations that have run through the grains during the deformation processes. In the left side of the system a partial dislocation on its way through a grain is seen (green arrow) [Sch98].

the stacking fault energy  $\gamma$  via the relation:

$$r = \frac{r_0(\gamma)}{1 - \sigma/\sigma_\infty(\gamma)} \quad (2.18)$$

where  $r_0 = k_1 b^2 / \gamma$  is the equilibrium splitting distance at  $\sigma = 0$ ,  $b$  the Burgers vector of the Shockley partial dislocation and  $\sigma_\infty = k_2 \gamma$  the resolved shear stress at which the splitting distance becomes infinitely large. The constants  $k_1$  and  $k_2$  depend on the elastic moduli of the material and the particular types of the two Shockley partials [Yam04, Hir92].

## 2.5.2 Microscopic observations

Microscopy has been widely used to study the plastic deformation behaviour of metals and alloys. Optical microscope (OM) is not able to reveal the deformation mechanisms of fine-grained

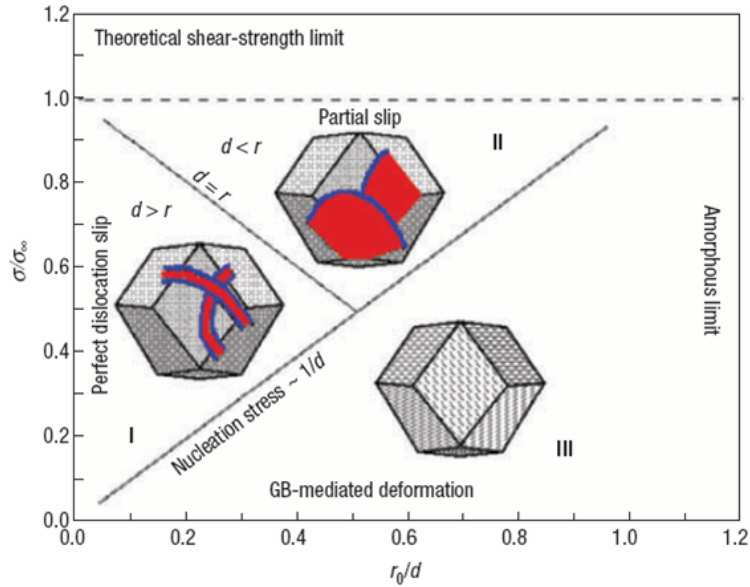


Figure 2.14: Map of the operational deformation mechanisms in NC fcc metals with grain size  $d$  during low-temperature deformation under a stress  $\sigma$  [Yam04].

materials due to the limited resolution. Among the high resolution microscopes (scanning electron microscope (SEM), transmission electron microscope (TEM) and the recently developed scanning probe microscope (SPM)) which have been applied to study the deformation mechanisms in nanometer range [Mar03, Hol04, Wel04, Veh97, Tho99], TEM (in-situ or ex-situ) is the most popular one. Some examples are given below.

- In-situ observation of dislocation activities and fracture behaviour in NC Ni

As grain size decreases down to several tens of nanometer, it is generally acknowledged that conventional dislocation sources such as the Frank-Read source cease to operate, and grain boundaries become potential dislocation sources and sinks. Post-deformation transmission electron microscope observations of NC metals have failed to uncover any evidence of dislocation activity characteristically observed in MC metals [Leg00]. However, in-situ TEM observation has revealed dislocation activity in the vicinity of crack tips [Kum03a]. A sequence of TEM images captured during an in-situ deformation test of a microtensile NC Ni with grain size in the 30–40 nm regime is shown in Fig. 2.15. In Fig. 2.15a, three grains (whose boundaries are identified by the three white arrows) and the crack tip denoted as A are seen. This image was obtained with the specimen under

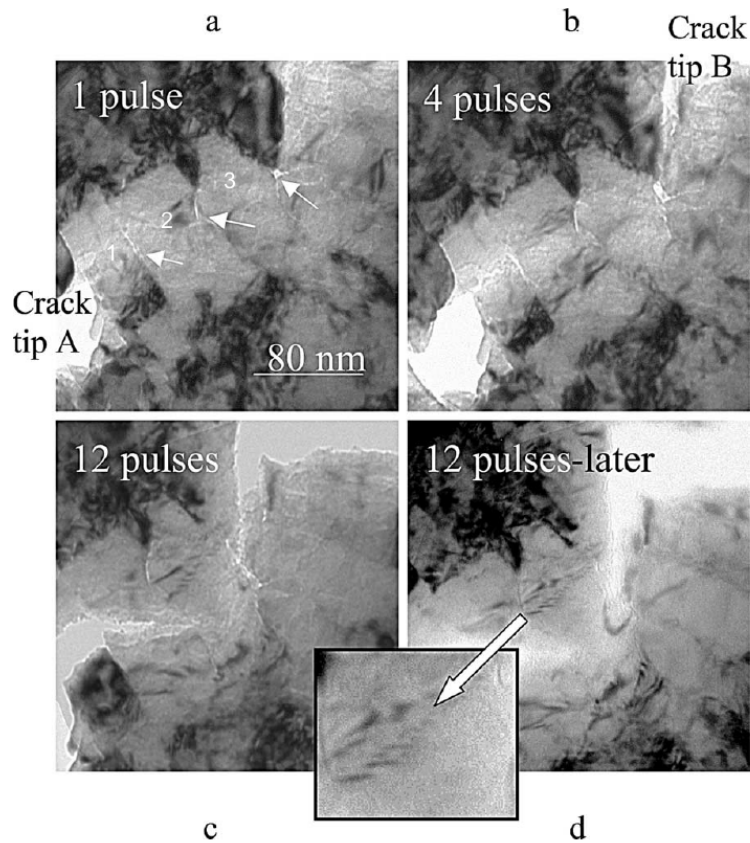


Figure 2.15: A sequence of images captured during an in-situ deformation test in the TEM of a microtensile NC nickel specimen. The presence of grain boundary cracks and triple-junction voids are indicated by white arrows in (a). Dislocation emission from crack tip B in (b-d) as a consequence of the applied displacement can all be seen. The magnified inset in (d) highlights the dislocation activity. [Kum03].

load after one displacement pulse. The white arrows in Fig. 2.15a illustrate the presence of grain boundary microcracks and triple junction voids. Whether these defects were produced by prior loading or they were pre-existing is not known. After four displacement pulses (Fig. 2.15b), the crack appears to proceed part way through grain 1, and the grain boundary cracks and triple junction void appear to have grown. A second crack (crack B) arrives in this region from the top right corner in Fig. 2.15b. The same location after 12 pulses is shown in Fig. 2.15c, where the progression of Crack A through grain 1 as well as through most of grain 2 is evident. The progression of crack B, from the top of the image down into grain 3 is also seen, with only a segment of grain 3 left intact. An array

of dislocations appears to have been emitted from crack B; at a later time, Fig. 2.15d, the array is still observed but it has a different configuration and the inset in Fig. 2.15d shows the array at this stage at a higher magnification [Kum03].

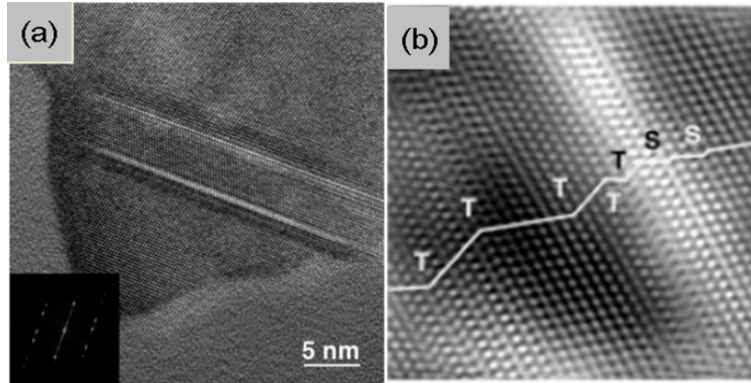


Figure 2.16: Deformation twins and stacking faults in NC Al. (a) HRTEM micrograph showing a deformation twin with parallel boundaries around an indent in NC aluminium; (b) A close-up view of deformation twins (T) and stacking fault (S) in NC aluminium deformed by manual grinding [Che03a].

- Deformation twins and stacking faults in NC Al

Twinning in NC Al, which has been suggested by MD simulations [Yam02a, Yam02b], has been confirmed by high resolution TEM (HRTEM) observations. NC aluminium films were deformed by microindentation and by manual grinding to allow the introduction of large plastic strains and to facilitate TEM observations of the deformation defects. Around the edges of the indent, planar defects with two parallel flat boundaries were seen in a number of grains and were identified as deformation twins. The width and orientation of the twin bands varied from grain to grain. The twinning seems to occur preferentially in smaller grains and propagates across the entire grain. In CG aluminium deformed under the same indenter, a large number of dislocations rather than deformation twinning were found. An example is shown in the HRTEM micrograph of Fig. 2.16a, together with a Fast Fourier Transform (FFT) pattern. Deformation twins were also observed in TEM micrographs of NC aluminium deformed by manual grinding. The multiple twins are highlighted in the Fourier-filtered image (Fig. 2.16b). Stacking faults, dislocations,

and microbands were also observed in the samples [Che03a].

- Watching nanograin rotation

By using an in-situ dark-field TEM technique, Shan et al. [Sha04] found that nanograin rotation in NC nickel films with an average grain size of about 10 nm has become the prominent deformation mode during deformation (Fig. 2.17). Because the plastic behavior of crystalline materials is mainly controlled by the nucleation and motion of lattice dislocations, the authors concluded that this change in the deformation mode arises from the grain size-dependent competition between the deformation controlled by nucleation and motion of dislocations and the deformation controlled by diffusion-assisted grain boundary processes.

### 2.5.3 In-situ X-ray diffraction profile

An in-situ X-ray diffraction profile technique, based on well-known peak profile analysis methods, was used to address the relationship between microstructure and mechanical properties in nanostructured materials recently [Bud04, Www02]. It uses high intensity X-rays from the Swiss Light Source synchrotron together with a specially developed microstrip detector covering a diffraction angle of  $60^\circ$  with an angular resolution of  $0.0037^\circ$ . The microstrip detector allows the measurement of the entire diffraction pattern at once during continuous deformation without having to sequentially scan the angular range of the scattering angle, as is usually done in powder diffraction techniques. Thus a peak profile analysis of several Bragg diffraction peaks can be followed in-situ during deformation.

X-ray diffraction profile analysis is a well-known technique for microstructural analysis, where peak broadening occurs for two reasons: (I) limitations in the spatial extent of the coherent scattering volumes and (II) the presence of inhomogeneous strain. Possible sources for inhomogeneous strain are lattice dislocations, but other sources can be of equal importance, especially in NC structures. For example, it was implied from X-ray diffraction experiments that cold rolling of 10–30 nm grain size Pd (produced by gas-phase condensation) caused an increase in stacking fault density, although the grain shape remained equiaxed and there was no preferred texture. Furthermore, an increasing dislocation density in CG metals will contribute

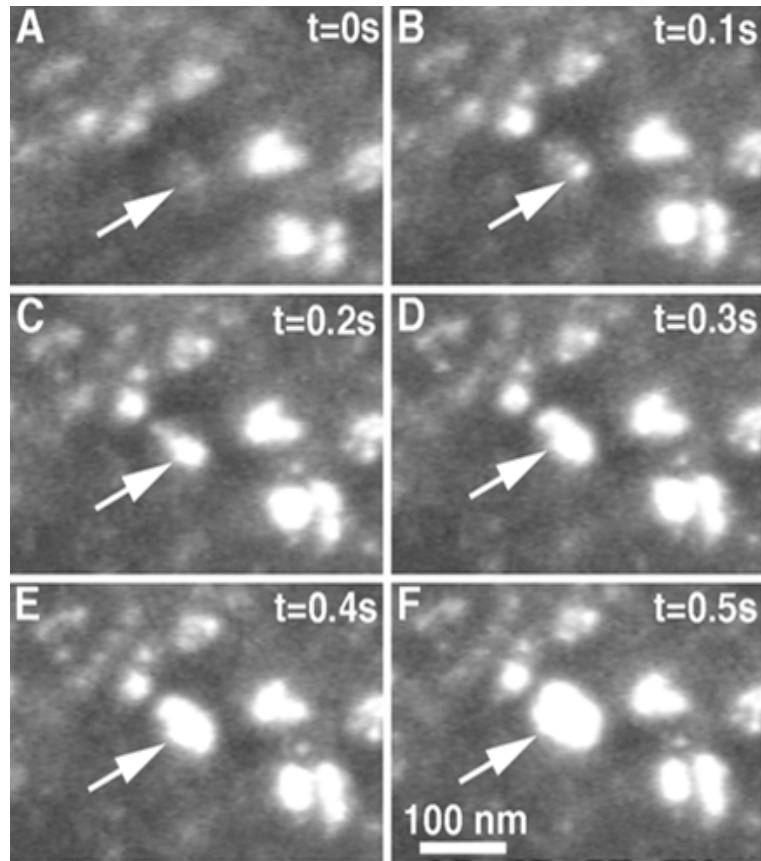


Figure 2.17: Dark-Field TEM observation of the rapid genesis of an agglomerate (e.g. white arrow) depicted by individual still frames extracted from a dynamic video sequence. (A) At  $t = 0$  s, no grains in the strong diffraction condition are near the white arrow; (B) At  $t = 0.1$  s, a grain in the strong diffraction condition with a size of about 6 nm is visible; (C) At  $t = 0.2$  s, a group of grains in bright contrast with a size of about 28 nm is visible; (D) At  $t = 0.3$  s, the group of grains has a nearly elliptical shape, with dimensions of 60 by 35 nm; (E) At  $t = 0.4$  s and (F)  $t = 0.5$  s, the size of the group of grains increases to maximum dimensions of about 80 by 60 nm [Sha04].

to the peak broadening.

Budrovic et al. [Bud04] found that the plastic deformation in CG metals, which is governed by dislocation-mediated processes and leads to the accumulation of a residual dislocation network, produces inhomogeneous strain and an irreversible broadening of the Bragg peaks in x-ray diffraction. However, the observation of the plastic deformation in electrodeposited NC Ni shows that the peak broadening is reversible upon unloading; there is an increase in dislocation density during loading, which disappears at unloading. Hence, the deformation process in NC Ni does not build up a residual dislocation network, evidencing a lack of dislocation debris. Their observation supports the absence of substantial work hardening in NC metals. The authors stated that this technique has a clear advantage over in-situ tensile deformation in TEM, because the high energy of the light source guarantees a better statistical approach and excludes thin-film artefacts.

### 2.5.4 Study of the thermal activation parameters

It is generally accepted that plastic deformation of metals associates with the thermally activated processes. As it has been introduced in section 2.2.2, the primary thermal activation parameters of interest are the strain rate sensitivity (SRS) and activation volume ( $AV$ ) which can be obtained by performing experiments employing strain rate and temperature changes. An analysis of these thermal activation parameters can shed light on the deformation mechanisms.

Wei et al. [Wei04] carried out strain rate jump tensile tests on CG and UFG fcc Cu, and UFG body-centered-cubic (bcc) Ta and Fe to obtain strain rate sensitivity and activation volume of the three UFG metals. They found that the strain rate sensitivities of the UFG fcc metals is much elevated, and those of the UFG bcc metals much reduced compared to the CG microstructure. They also observed that the activation volume in UFG Cu has been reduced whereas that of bcc metals remains largely unchanged in the UFG regime. May et al. [May05] also reported pronounced strain rate sensitivity for UFG Al compared to the conventionally CG Al, and similar results were obtained by Conrad [Con03], who studied the grain size dependence of plastic deformation kinetics in Cu.

Although some inconsistency exists, the data from the limited literature reported show that with decreasing grain size (for fcc metals), strain rate sensitivity increases and activation vol-

ume decreases. Different mechanisms were proposed. For example, Conrad [Con03] suggested that in the grain size regime 1000 nm–10 nm, the deformation mechanism is grain boundary shear promoted by dislocation pile-ups; in the grain size smaller than 10 nm the deformation mechanisms is grain boundary shear. Schwaiger et al. [Sch03] explained the marked SRS observed in UFG and NC nickel on the premise that a rate-sensitive grain boundary affected zone exist. In conclusion, a universally accepted mechanism responsible for this behavior has not achieved. This may be attributed to the different experimental specimens, loading conditions, displacement and monitoring techniques, and of course the precision of data. Therefore, further effort has to be made to clarify this issue.

## 2.5.5 Nanoindentation

### 2.5.5.1 Background information

Indentation tests are perhaps the most commonly applied methods for testing the mechanical properties of materials. The indentation hardness implies the resistance of materials to local plastic deformation. It is not a physical property of a material. In a conventional indentation test, a known load is applied to press a hard tip (typically a diamond) into the sample and then removed after some time. Then the indentation hardness is defined as:

$$H = \frac{F_{max}}{A} \quad (2.19)$$

where  $F_{max}$  is the maximum applied load and  $A$  the area of impression usually measured by a microscope.

The measurement of hardness on a micro- and nanometer scale has been manifested more and more important to get the local properties from very small volumes of the material. Conventional apparatus for hardness measurement became not suitable because the components to be analyzed become smaller and the limits of resolution are continually being pushed back.

Nanoindentation (refers to the depth sensing indentation (DSI)) technique was recently developed for the measurement of mechanical properties at a size scale beyond the optical capabilities. In this method a sharp indenter is pressed into the sample surface and then removed, and the displacement of the indenter tip at a known load is recorded. The probe tip has a very well defined area function based on the indent depth, enabling contact area calculation from

the displacement. With this new measurement technique, loads as small as tenths of micro-newtons and depths as small as fractions of nanometers, are measurable. By analyzing the load-displacement (F-h) data recorded during the indentation process, it is possible to measure the hardness and additionally the Young's Modulus of the tested sample without imaging the indent. Additionally, mechanical properties such as continuous stiffness, scratch resistance, film-substrate adhesion, residual stresses, time dependent creep and relaxation properties, fracture toughness and fatigue can be measured by nanoindentation technique, based on elastic contact theory and load-displacement data. Many commercial nanoindenter, such as Nano Indenter XP, TriboIndenter, UMIS II, Nano Hardness Tester and Nano Test System are available [Bhu03, Li02].

The most successful and widespread model for nanoindentation data analysis is one in which the unloading data are assumed to arise from a purely elastic contact (Hertzian contact [Her81]). This approach was developed over 40 years with contributions from a number of groups around the world, and the most commonly used form now is that presented by Oliver and Pharr, known as the Oliver–Pharr method [Www03, Oli92].

The basic assumptions of this approach are:

1. Deformation upon unloading is purely elastic.
2. The compliance of the specimen and of the indenter tip can be combined as springs in series:

$$\frac{1}{E_r} = \frac{1 - \nu_{specimen}^2}{E_{specimen}} + \frac{1 - \nu_{indenter}^2}{E_{indenter}} \quad (2.20)$$

where  $E_r$  is the “reduced modulus”,  $E$  the Young's modulus,  $\nu$  the Poisson's ratio respectively.

3. The contact can be modeled using an analytical model for contact between a rigid indenter of defined shape with a homogeneous isotropic elastic half space using:

$$S = \frac{2}{\sqrt{\pi}} E_r \sqrt{A_c} \quad (2.21)$$

where  $S$  is the contact stiffness and  $A_c$  the contact area. This relation, presented by Sneddon [Sne65], was demonstrated to be a robust equation which applies to tips with a wide range of shapes by Pharr, Oliver and Brotzen [Pha92].

The first complete nanoindentation data analysis was presented by Doerner and Nix [Doe86], who argued that, if the change in contact area is small during unloading, the indenter can be treated as a flat punch. Assuming that all of the material in contact with the indenter is plastically deformed and that outside the contact only elastic deformation occurs at the surface during loading, they were able to make the connection between F-h data and the contact area. The indentation geometry at maximum load  $F_{max}$  and after unloading is illustrated in Fig. 2.18. The “contact depth”  $h_c$  can be resulted by extrapolating the slope S of the unloading data at maximum load  $F_{max}$  to the displacement axis, see Fig. 2.19a.

$$S = \frac{dF}{dh} \tag{2.22}$$

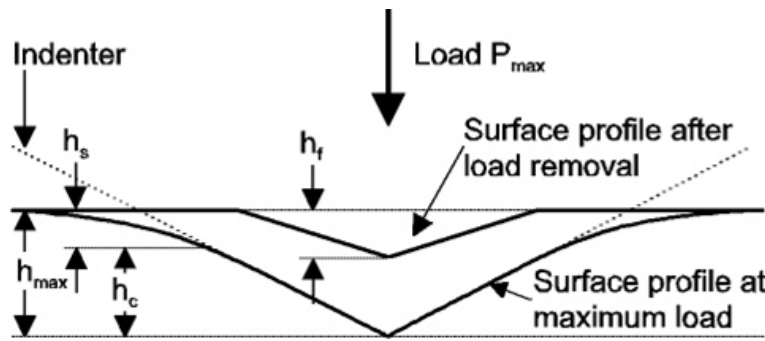


Figure 2.18: Illustration of the indentation geometry at maximum load and after unloading.

The hardness is defined simply as:

$$H = \frac{F_{max}}{A(h_c)} \tag{2.23}$$

where  $A(h_c)$  is the projected contact area at maximum load. If the tip shape is accurately known, a tip area function

$$A_c = f(h_c) \tag{2.24}$$

can be generated. Doerner and Nix measure the shape of their indenter by making a series of indents in soft brass and relating the contact depth to the contact area measured by imaging acetate replicas of those indentations in TEM.

This definition of hardness is different from the conventional definition of hardness. In the nanoindentation analysis the hardness is calculated utilizing the contact area at maximum load whereas in conventional tests the area of the residual indent after unloading is used.

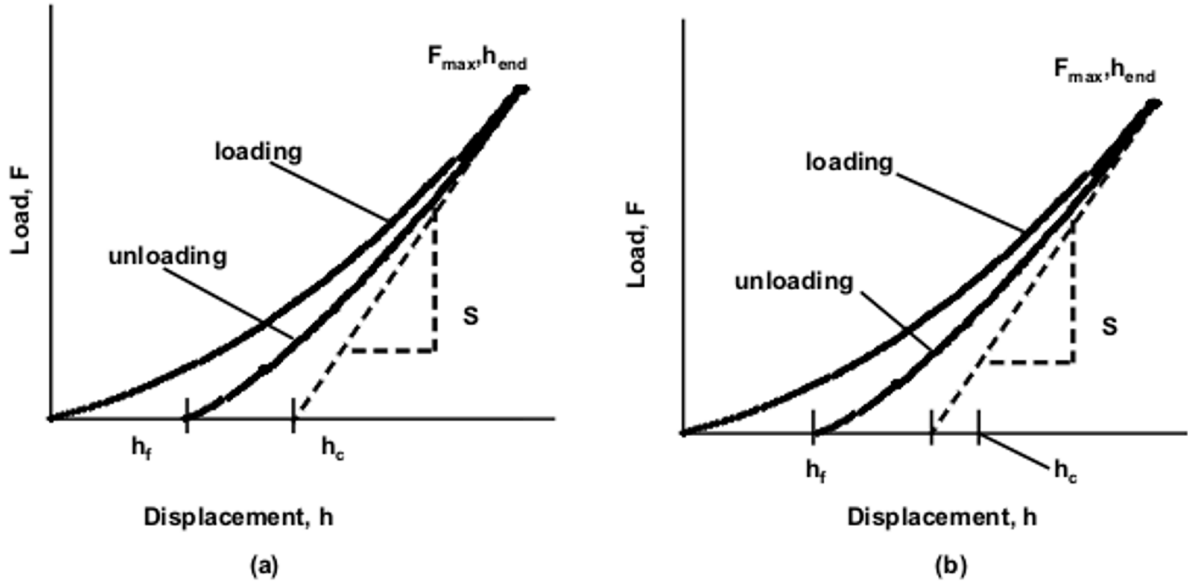


Figure 2.19: Schematic plots of the nanoindentation data analysis model. (a) the Doerner and Nix model; (b) the Oliver and Pharr model.

Since an elastic contact analysis is used, the elastic modulus of the material can be obtained. The contact area from equation 2.24 is combined with the stiffness (equation 2.21) at maximum load to find the reduced modulus in equation 2.20. If  $E$  and  $\nu$  for the indenter material are known, the Young's modulus  $E$  for the sample material can be obtained.

Oliver and Pharr [Oli92] made a critical improvement to the method proposed by Doerner and Nix [Doe86]. Sneddon's contact solution [Sne65] predicts that the unloading data for an elastic contact for many simple indenter geometries (sphere, cone, flat punch and paraboloid of revolution) follows a power law that can be written as follows:

$$F = \alpha h^m \quad (2.25)$$

In this equation  $F$  is the indent load,  $h$  is the elastic displacement of the indenter and  $\alpha$  and  $m$  are constants. Oliver and Pharr apply this formulation to determine the contact area at maximum load as it is valid even if the contact area changes during unloading. To do this, they derive the following relationship for the contact depth,  $h_c$ , from Sneddon's solutions:

$$h_c = h_{max} - \theta \frac{F_{max}}{S} \quad (2.26)$$

where  $\theta = 0.72, 0.75$  and  $1$  for cone-, sphere- and flat-punch-geometry respectively. The procedure for Oliver and Pharr analysis is to fit a power law function to the unloading segment.

This yields the contact stiffness  $S = dF/dh$  as slope of this function at maximum load. This slope in addition to the appropriate value of  $\theta$  is used in order to determine the actual contact depth so that it is finally possible to derive the indentation modulus in equation 2.20 and the indentation hardness in equation 2.23 from the measurement. A schematic sketch of such an analysis is shown in Fig. 2.19b.

### 2.5.5.2 Pop-in and dislocation nucleation during nanoindentation

One important phenomenon during nanoindentation is dislocation nucleation (Fig. 2.20), corresponding to the appearance of pop-ins (the discontinuities in the load-displacement ( $F-h$ ) curve, Fig. 2.21). The origin of different pop-ins has been intensively studied by many au-

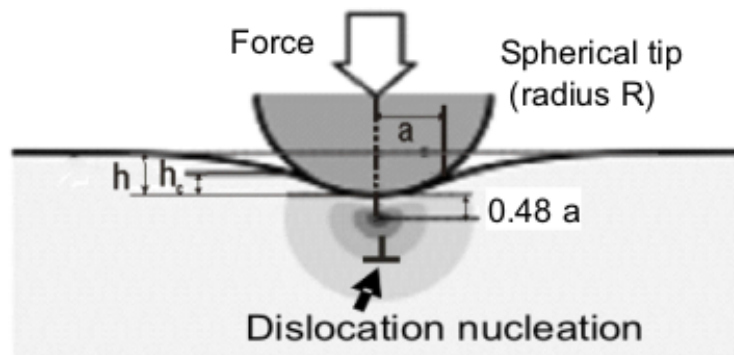


Figure 2.20: Dislocation nucleates under the indenter tip at a depth of about  $0.48a$ , where the maximum shear stress is reached [Kem02a].

thors [Gök99, Gök01, Lor03]. Although pop-in may be induced by other factors such as the breaking of surface oxide layers, phase transition in amorphous alloys and film delamination, for a metal with a low surface roughness and dislocation density, it refers to the homogenous dislocation nucleation under the indenter tip, which has been proved by microscopy observation [Gai03, Bra04, Min04, Kem02]. Pop-ins always mark a sharp transition from pure elastic loading to a plastic deformation of the specimen, thus corresponding to an initial yield point. Considering that the indenter tip is not ideally sharp and actually spherical, the Hertzian contact model can be used to fit the initial part of  $F-h$  curve to deduce valuable data.

According to Hertzian contact model the indent force  $F$  and the indent depth  $h$  is described

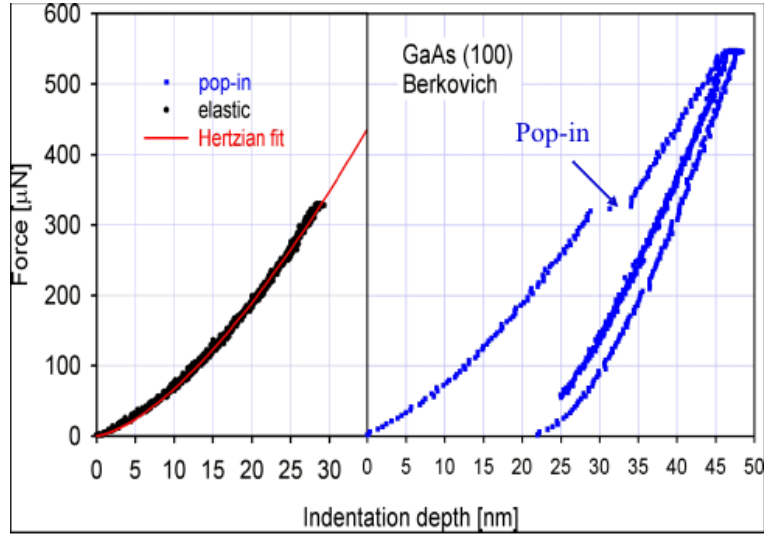


Figure 2.21: Hertzian contact model used for to fit the pure elastic part of F-h curves. A pop-in is marked in the load-displacement (F-h) curve recorded during nanoindentation with a Berkovich indenter tip on GaAs (100) (right). The initial part of the F-H curve before pop-in (left) can be fitted by the Hertzian contact model. With a known elastic modulus  $75.5 \text{ GPa}$  of GaAs, a tip radius of about  $460 \text{ nm}$  is deduced from equation 2.27. The maximum shear stress before pop-in deduced from equation 2.29 is about  $3.66 \text{ GPa}$ , which is near the theoretical strength value  $3.3 \text{ GPa}$ . This indicates that pop-in corresponds to the homogenous dislocation nucleation under the tip [Kem02a].

as:

$$F = \frac{4}{3} E_r \sqrt{R} h^3 \quad (2.27)$$

where  $E_r$  is the effective elastic modulus and  $R$  the combined radius (always taken to be the radius of the indenter tip).

The contact radius  $a$  can be expressed in this model as (Fig. 2.20):

$$a^2 = Rh \quad (2.28)$$

Dislocation nucleation begins at a depth of about  $0.48a$  (Fig. 2.20), where the maximum shear stress  $\tau_{max}$  under the indenter tip is reached:

$$\tau_{max} = \frac{0.31}{\pi} \left( \frac{6FE_r^2}{R^2} \right) \quad (2.29)$$

With the effective elastic modulus  $E_r$  obtained from the known Young's modulus  $E$  and Poisson's ration  $\nu$  of the specimen and the indenter material (diamond:  $E = 1141$  GPa,  $\nu = 0.07$ ) in equation 2.20, values of the indenter radius  $R$  and the maximum shear stress  $\tau_{max}$  can be estimated from equation 2.27 and 2.29.

### 2.5.5.3 Indentation size effect

That the hardness decreases with increasing indentation size is known as the indentation size effect (ISE), which has been observed in numerous nanoindentation experiments on various materials [Fle94, Maq95]. This decrease is believed to be associated with the geometrically necessary dislocations (GNDs) induced by imposed strain gradients. Nix and Gao (NG) [Nix98] successfully modeled the ISE for crystalline materials by considering the density of GNDs around a conical indenter. The NG-model has become one of the commonly cited treatments of the ISE. In the NG-model, it is assumed that the indentation is accommodated by circular loops of

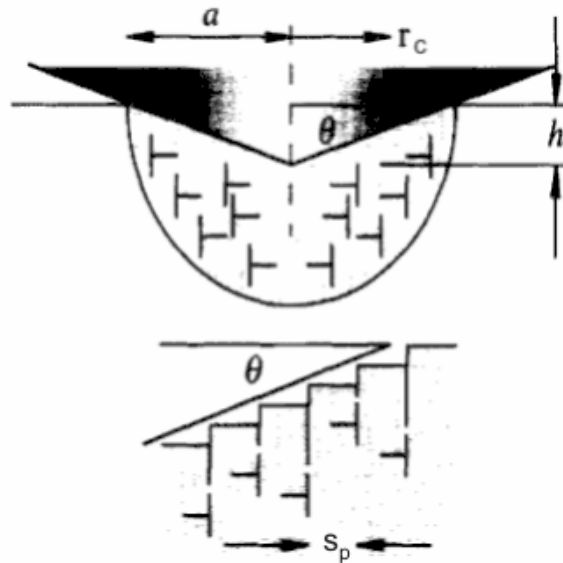


Figure 2.22: Geometrically necessary dislocations created by a rigid conical indentation. The dislocation structure is idealized as circular dislocation loops.  $a$  is the contact radius,  $r_c$  the radius of the circular loops,  $\theta$  the angle between the surface of conical indenter and the plane of the surface,  $h$  the indentation depth,  $s_p$  the spacing between individual slip steps on the indentation surface [Nix98].

GNDs with Burgers vector normal to the surface, as shown schematically in Fig. 2.22. Assuming that the individual dislocation loops are spaced equally along the surface of the indentation gives

$$\tan\theta = \frac{h}{a} = \frac{b}{s_p} \quad (2.30)$$

$$s_p = \frac{ba}{h} \quad (2.31)$$

where  $s_p$  is the spacing between individual slip steps on the indentation surface,  $b$  the magnitude of the Burgers vector,  $h$  the indentation depth,  $a$  the contact radius, and  $\theta$  the angle between the surface of the indenter and the plane of the sample surface, as shown in Fig. 2.22. The total line length  $\lambda$  of dislocation loops necessary to form the shape of the conical indenter is

$$\lambda = \int_0^a \frac{h}{ba} 2\pi r_c dr_c = \frac{\pi ha}{b} = \frac{\pi \tan\theta}{b} a^2 = \frac{\pi}{b} \cdot \frac{h^2}{\tan\theta} \quad (2.32)$$

It is also assumed that all of the injected loops remain within a hemispherical volume  $V_d$  defined by the contact radius

$$V_d = \frac{2}{3}\pi a^3 \quad (2.33)$$

So the density of the GNDs  $\rho_G$  is given by

$$\rho_G = \frac{\lambda}{V_d} = \frac{3h}{2ba^2} = \frac{3\tan^2\theta}{2bh} \quad (2.34)$$

By taking Tabor's factor to be 3 and applying the von Mises flow rule and the Taylor relation, the relation between hardness and dislocation density is expressed as:

$$H = 3\sigma = 3\sqrt{3}\tau = 3\sqrt{3}\alpha_1\mu b\sqrt{\rho_G + \rho_s} \quad (2.35)$$

where  $\sigma$  is the normal stress,  $\tau$  the shear stress,  $\alpha_1$  a constant,  $\mu$  the shear modulus, and  $\rho_s$  the density of statistically stored dislocations which determines the hardness  $H_0$  in the absence of any GNDs:

$$H_0 = \alpha_1\mu b\sqrt{\rho_s} \quad (2.36)$$

From these equations, the measured hardness  $H$  related with the indentation depth  $h$  can be described as

$$\sqrt{\frac{H}{H_0}} = \sqrt{1 + \frac{\rho_G}{\rho_s}} = \sqrt{1 + \frac{h_0}{h}} \quad (2.37)$$

where  $h_0$  is a length scale depending on  $\rho_s$  through  $H_0$ . Rewriting this equation as

$$H^2 = H_0^2 \left(1 + \frac{h_0}{h}\right) \quad (2.38)$$

a linear relationship would be found in the plot of  $H^2$  vs.  $h^{-1}$ .

In the NG-model, it is assumed that all the GNDs are contained in a hemisphere, namely the plastic zone, with a radius equal to the contact radius  $a$ . However, GNDs will spread beyond the hemisphere assumed due to the strong repulsive force between GNDs for very small indentation depth [Swa02]. It means the actual plastic zone is larger than that described in the NG-model. This has been confirmed by the overestimation in hardness by the NG-model at small indentation depths observed in several experiments [Fen04, Dur05], where the radius of plastic zone was taken to be  $fa$ ,  $f \geq 1$  to correct the NG-model at small indentation depths.

## 2.6 Open questions and aims

### 2.6.1 Local examination of Hall-Petch relation

There is no denying that the wide applicability of the classical H-P relation has made it one of the most important constitutive relations in Materials Science. However, the physical basis of H-P behaviour, which is generally accepted to be associated with the pile-up of dislocations at the grain boundaries [Mey82], and the reason for the deviation of H-P relation in nanograin size range, remain imperfectly understood. This could be attributed to the following reasons:

1. H-P relation is based on the local interaction between dislocations and grain boundaries, but it is difficult to design experiments to examine this interaction locally. So far, this could be only done in tensile tests on TEM foils with the usual problems to measure stress and strains.
2. Most experiments average over many grains. They are made on a macro scale and the quantitative data give only the dependence of the yield stress on the average grain size. However, the concept of the mean grain size is not accurate, because yielding always starts in the largest grain of the microstructure. In this sense, the mean grain size is only appropriate when the grain size distribution is narrow and the grain shape is regular.

In NC and UFG materials, depending on the production technique and their consequent time-temperature history, the grain size distribution is wide. Hence, the results depend on the largest grains over which the experimental technique averages. Probing individual grains instead of using the mean grain size seems to be more reasonable and reliable, but experiments on individual grains are difficult to perform since the surface preparation is very difficult to image single grains in nanocrystals and to perform local tests.

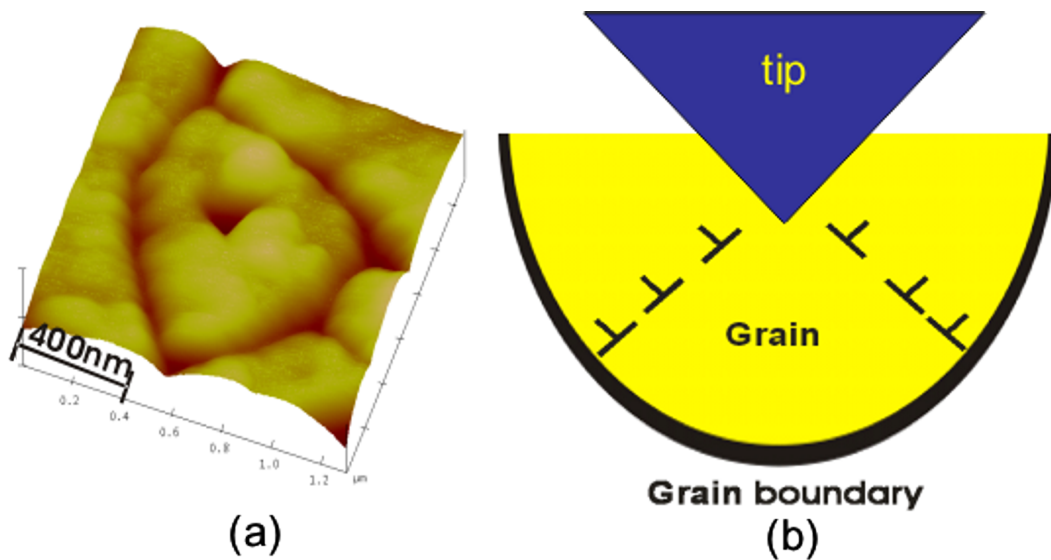


Figure 2.23: Study the local interaction between dislocations and grain boundaries in single grains by NI-AFM. (a) Nanoindenting in the center of a grain; (b) Dislocations nucleated under the tip interact with the grain boundary.

The above considerations were the inspiration for the following question:

How to examine the grain boundary-dislocation interaction in single grains and measure H-P relation locally?

In this work, different grain sizes ranging from the nanometer to the micrometer scale were produced by an appropriate heat treatment from nanonickel produced by pulsed electrodeposition. As it has been stated in 2.5.5, nanoindentation has been widely used to study the mechanical properties of materials. Nanoindentation combined with an imaging system of atomic force microscopy (NI-AFM, details on the equipment will be described in section 3.4.1) makes it available for the measurements of the local mechanical properties at a nanoscale. By using

a NI-AFM nanoindents were performed in the center of individual grains (Fig. 2.23a). Dislocations can be nucleated during nanoindentation below the indenter tip, and the nucleation of dislocations can be directly probed from the appearance of pop-ins in the load-displacement curves recorded (see 2.5.5.2). In doing this, we aim to study the interaction between dislocations and grain boundaries directly in single grains (Fig. 2.23b), hence the local examination of H-P relation.

## **2.6.2 Deformation mechanisms of bulk electrodeposited nanonickel**

As stated in section 2.1.3.2, different H-P slope values in nanometer grain size range at room temperatures have been reported in various metals, including positive, zero and negative slopes, indicating a transition of the deformation mechanisms. It is suggested that this transition is related to the interplay between dislocation and grain boundary processes (such as grain boundary sliding, enhanced Coble creep, nucleation of partial dislocations and twins from grain boundaries), however, how NC material deforms is not completely understood yet. This could be attributed to the following reasons:

1. NC specimens resulted from different production techniques always give controversial results due to the different internal structures and processing-induced artefacts (such as contamination, porosity and residual stress).
2. Some techniques can not produce sufficiently large and defect free specimens, resulting in the most mechanical properties reported are hardness, while others such as tensile, fatigue and fracture properties are rarely reported. Therefore, a complete understanding of the deformation mechanisms is hindered.
3. Most theoretical or computational studies focus on yield strength and related deformation mechanisms, but do not describe the rate-dependent mechanical behaviour of nc materials under realistic load or strain rates.
4. Most experimental techniques, such as TEM observations and MD simulations, only give indirect evidence of the deformation mechanisms of bulk NC materials. For example,

MD simulations must be conducted at extremely high strain rates which are many orders of magnitude higher than in experiments; TEM requires samples thinned to a thickness comparable to the grain size, inducing structural relaxations and thus changing the grain boundary structure. Therefore, it is a question whether these results represent the bulk behaviour of nanocrystals.

Out of the above considerations, in this work, NC nickel specimens produced by pulse electrodeposition are chosen, because they have hardly any porosity, high purity (> 99.9%) and a narrow grain size distribution with mean grain size smaller than 30 nm. In addition, they are large and thick enough for systematic tests (indentation, tensile, bending etc.) of mechanical properties.

We perform the following experiments on bulk nickel specimens with grain size ranging from the original nanoscale to microscale at room temperatures:

1. Strain rate jump experiments in tensile tests and nanoindentation experiments by using different loading rates. By analysing the grain size effects on the thermal activation parameters (strain rate sensitivity and activation volume) revealed from these experiments, a better understanding of the deformation mechanisms of NC materials, dislocation or grain boundary processes, can be achieved.
2. Tensile stress jump in creep experiments to study the room temperature creep behaviour.
3. Deformation behaviour of bulk NC nickel in-situ studied in an AFM combined with other equipments. Besides its high resolution, AFM has special advantages of performing measurements directly on bulk specimens. In this work, besides the indentation behaviour in-situ studied by the NI-AFM, we study the bending behaviour, fatigue response and fracture of bulk electrodeposited NC nickel specimens with a newly developed 4-point-bending machine (details on this equipment described in section 3.4.2).

# 3 Experimental

## 3.1 Specimen preparation

### 3.1.1 As-prepared specimen

Two kinds of the as-prepared specimens, bulk NC nickel produced by pulsed electrodeposition and CG commercial nickel (mean grain size larger than 10  $\mu\text{m}$ ) were used in this work. The original size of as-electrodeposited nanonickel plates are 65 mm in length and 35 mm in width, with thickness larger than 1 mm (1–4 mm). Both of them have high purity ( $> 99.9\%$ ) and hardly any porosity.

### 3.1.2 Specimens for indentation, tensile and bending tests

Specimens for indentation, tensile and bending tests were cut by an electro-discharge machine (EDM) from as-prepared bulk plate, as shown in Fig. 3.1. Indentation specimens were small pieces of 5–14 mm in diameter. The shape of the tensile and bending specimens is shown in Fig. 3.2.

### 3.1.3 Heat-treatments

Different heat-treatment procedures were used to produce UFG and MC specimens. Small specimens were encapsulated in quartz glass filled with inert gas argon. This procedure was only used for small indentation specimens due to the limited room of the glass. Larger specimens (for tensile and bending) were heat-treated in vacuum ( $10^{-6}$  mbar).

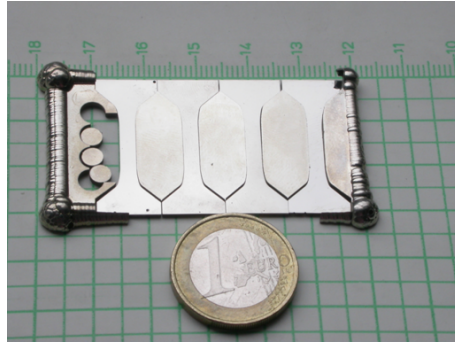


Figure 3.1: As-deposited nanocrystalline nickel plate and specimens cut by EDM.

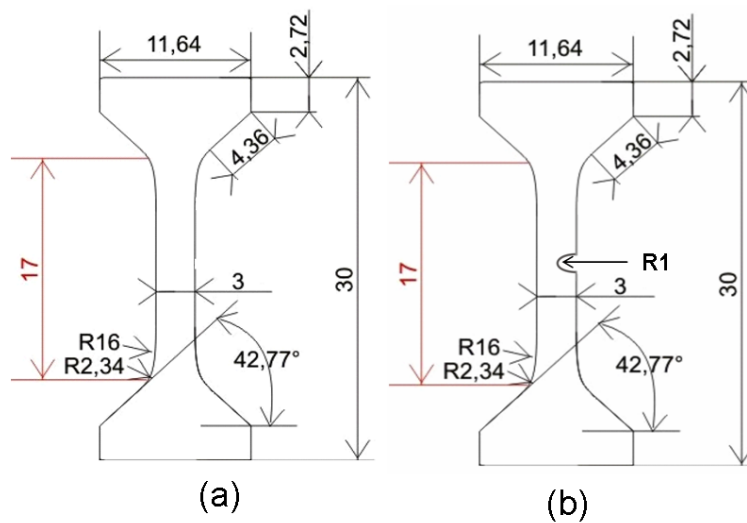


Figure 3.2: Shape of specimens for (a) tensile and (b) bending tests.

### 3.1.4 Surface finish preparation

All the specimens were prepared by standard metallographic preparation techniques, including mechanical polishing and electropolishing.

#### 3.1.4.1 Mechanical polishing

Specimens were first smoothly and carefully ground and polished with number 400–4000 sand sheets. Then the specimens were further polished with diamond paste with particle size from  $1\ \mu\text{m}$  to  $0.25\ \mu\text{m}$  and  $\text{SiO}_2$  paste ( $0.1\text{--}0.04\ \mu\text{m}$ ) to get a mirror surface finish. At last the specimens were cleaned with distilled water and dried.

### 3.1.4.2 Electropolishing

Electropolishing was performed with a polishing machine *LectroPol-5* from *Struers*. Electrolyte  $H_2SO_4(20ml) + CH_3OH(80ml)$  is used unless stated otherwise. The polishing parameters are 20 V for 20 s for nanonickel and 35 V for 60 s for MC (or CG) nickel with stainless steel as cathode.

## 3.2 Microstructure analysis

A Dimension 3000 AFM system (SPM 3000, Digital Instruments) was mainly utilized to analyze the microstructure. The maximum scan size is  $100\ \mu m \times 100\ \mu m$ . A cantilever with a tip radius of about 30 nm provides a lateral resolution of nearly 2 nm and a vertical resolution of 0.2 nm. X-ray diffraction(XRD), TEM and SEM are used as complementary methods.

## 3.3 Mechanical property measurements

### 3.3.1 Microindentation

Microindentation experiments were made with a Vickers hardness testing machine (*Leica-VWHT-MOT*). All experiments were performed at room temperature. Different maximum loading forces from 49 mN to 19 N are available. The maximum loading force is always kept 15 s before unloading. At least five indents were performed for each test.

### 3.3.2 Nanoindentation

All nanoindentation experiments were accomplished using a NI-AFM (nanoindentation combined with a high resolution imaging system AFM) from Hysitron Inc. A Berkovich diamond tip was used for all measurements. Load displacement (F-h) curves are taken in the indenting mode of the NI-AFM. Mechanical properties are calculated from the load-displacement curve recorded during indentation following the standard method proposed by Oliver and Pharr [Oli92].

### 3.3.3 Tensile experiments

Tensile strain rate jump tests and tensile stress jump experiments were performed to study the thermal activation parameters and creep behaviour of nickel, respectively. All experiments are performed at room temperatures and driven by LabVIEW programs. Two tensile machines (mechanic, Instron 8513 and hydraulic, Instron 8511) were used. The speed of the cross-head ranges from  $1.7 \times 10^{-7}$ – $1.7 \times 10^{-1} \text{ mm} \cdot \text{s}^{-1}$  for Instron 8513 and  $8.3 \times 10^{-2}$ – $5.5 \times 10^1 \text{ mm} \cdot \text{s}^{-1}$  for Instron 8511. Tensile specimens were machined by EDM from the as-prepared bulk plates, as schematically shown in Fig. 3.1 and Fig. 3.2.

### 3.3.4 In-situ bending AFM experiments

The bending behaviour, fatigue response and fracture of bulk electrodeposited NC nickel specimens were studied in an AFM with a newly developed in-situ 4-point-bending machine (in-situ bending AFM). Fatigue experiments were performed in a computer-controlled hydraulic test system. Specimen (shown in Fig. 3.2b) was initially fatigued by symmetrical push-pull testing at a constant plastic strain amplitude of  $6 \times 10^{-4}$  for 3000 cycles to produce a crack. An optical microscopy was used to check the crack initiation and the crack length. After the nucleation of the crack, the amplitude was reduced to  $3 \times 10^{-4}$  for 2000 cycles before the specimen was unloaded. Surface deformation and crack of the specimens were examined using the in-situ bending AFM equipment. The details of the new equipment is described in the following section 3.4.2.

## 3.4 Equipments

### 3.4.1 Hysitron TriboScope

#### 3.4.1.1 System

All nanoindentation measurements in this work were accomplished by Hysitron TriboScope from Hysitron Inc. The TriboScope testing and imaging system expands the capabilities of AFM to material testing at micro and nanometer resolutions. It is a powerful and unique in-

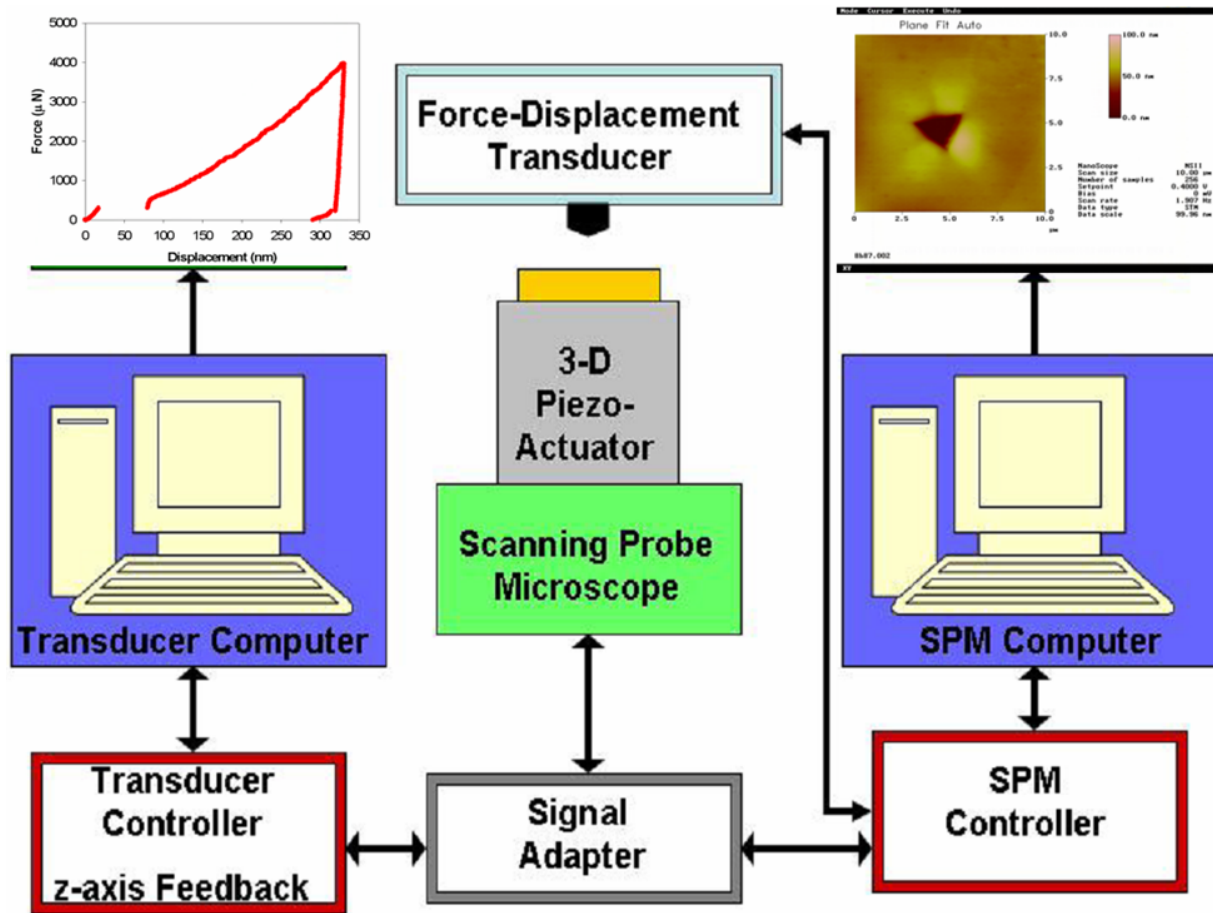


Figure 3.3: Schematic diagram of the indentation system which consists of the Triboscope and a Scanning Probe Microscope (SPM).

strument combining ultra-light load nanoindentation and high-resolution in-situ imaging in a single system eliminating lab time. Precise micro/nano indents and microscratch testing can be performed, plus in-situ high resolution surface imaging. An image of the tested area can be captured immediately after the test has been completed, without disturbing the sample. Accurate numerical data necessary to evaluate the plastic and elastic behaviour as well as visual information of region tested can be obtained.

The whole nanoindentation system is schematically shown in Fig. 3.3. It consists of two instruments: an commercial SPM (multimode AFM from Digital Instruments) consisting of the SPM controller, monitor and 3-D piezo actuators, and the TriboScope itself consisting of a transducer and its associated hardware of the Hysitron indenter system. The transducer assem-

bly replaces the optical head of the AFM. The system has a depth resolution of 0.2 nm and can apply indentation loads as high as 7000  $\mu\text{N}$  with a resolution of 0.1  $\mu\text{N}$ .

The TriboScope uses a simple three-plate capacitor system for its force displacement transducer, which is the heart of the instrument specially designed for load/displacement control. Fig. 3.4 shows the transducer assembly schematically. The sensor consists of two fixed outer plates (the drive plates) and one pickup electrode (the middle plate) which is spring mounted, and therefore free to move up and down in the region between the two drive plates. This middle plate has a screw, which is where the tip attaches. To perform an indentation an electrostatic force is generated between the drive plates and the pickup electrode when a voltage is applied to the drive plates. The terminals labeled “CHA HV IN” and “CHB HV IN” are used to provide force that is electrostatically generated by the transducer. The electrostatic force ( $F_{el}$ ) is proportional to the square of the Voltage ( $V$ ) applied to the drive plate:

$$F_{el} = k_e \cdot V^2 \quad (3.1)$$

Where  $k_e$  is an electrostatic force constant (determined by the manufacturer and supplied with the transducer). Equation 3.1 is used to determine the tip-to-sample force during indentation. The area of the plates and the distance between them determines this electrostatic force constant. Once calibrated the instrument determines the appropriate voltage profile to apply the required force profile for the specified indentation test. For displacement sensing, the two outer electrodes are driven by AC voltage that is 180° out of phase. This results in an electrostatic field whose potential varies linearly with lateral displacement, due to the close proximity of the plates. In the center this field is zero, because the two fields cancel each other out. At the location of either plate the field is proportional to the voltage applied. The middle plate or pick-up electrode assumes the potential of the position relative to the drive plates. The displacements are measured by changes in the capacitance of the stack of plates. This enables the displacement and applied load to be measured simultaneously [Tri96, McC04].

#### 3.4.1.2 Probe tips

The probe tip is a very important part of indentation testing. The geometry and the material of the tip can influence the raw data dramatically. The main requirements for the probe tip are

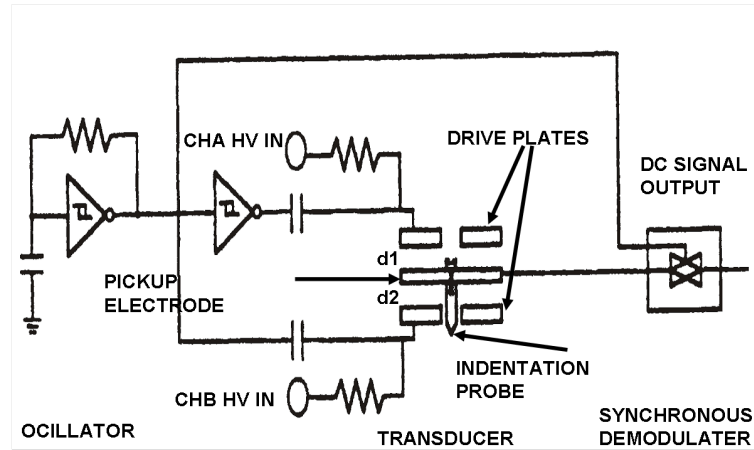


Figure 3.4: Schematic diagram of the Hysitron TriboScope transducer assembly.

high elastic modulus, no plastic deformation, low friction, smooth surface and a well defined geometry. The first four requirements are satisfied by choosing diamond as material for the tip. There are many tips available for use with the TriboScope nanomechanical testing system. The most common shapes of indenters are spheres, flat punches, cones, and pyramids. Three types, Berkovich, Cube Corner and Conical, and their projected area ( $A_{\perp}$ ) related to the depth ( $h$ ) are shown in Fig. 3.5. Each has its own load distributions, and therefore different load requirements for deformation. In this work, a Berkovich tip is always used unless stated otherwise. This Berkovich tip is three-sided pyramidal diamond directly brazed to a steel holder, with a nominal angle of  $65.3^{\circ}$  between the side face and the normal to the base at apex, an angle of  $76.9^{\circ}$  between edge and normal. This produces the same projected area to depth ratio as a Vickers indenter.

#### 3.4.1.3 Machine compliance and tip shape calibration

In nanoindentation test, the measured displacements are the sum of the indentation depth in the specimen and the displacements of the suspending springs and the displacements associated with the measuring instrument, referred to the machine compliance ( $C_m$ ). At large loads for materials with a high modulus, this can account for a significant portion of the total displacement. Therefore, to measure the accurate displacement into the specimen,  $C_m$  must be known with some precision. The total compliance of the system ( $C_t$ ) is  $C_m$  plus that of the indented

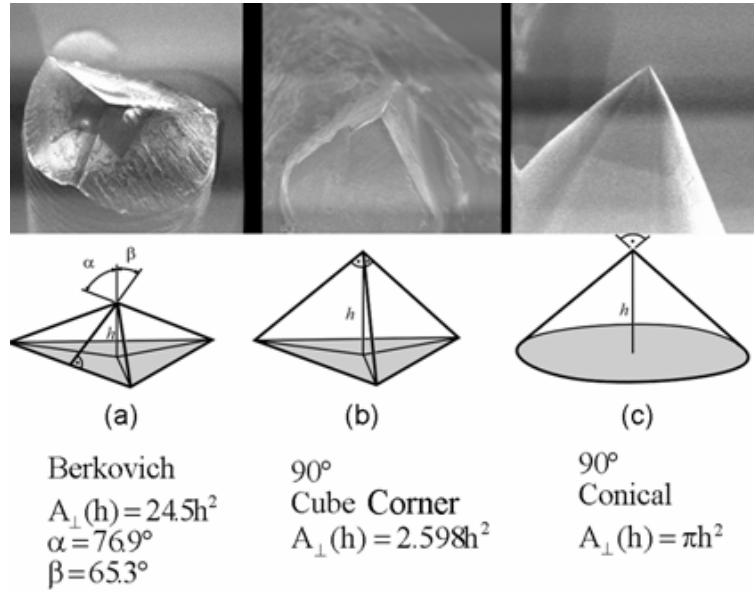


Figure 3.5: Schematic of nanoindentation probe tips and their projected area ( $A_{\perp}$ ) related to the depth ( $h$ ). (a) Berkovich; (b) Cube Corner; (c) Conical.

material, which is equal to one over the material stiffness  $S$ :

$$C_t = C_m + \frac{1}{S} = C_m + \frac{\sqrt{\pi}}{2E_r\sqrt{A_c}} \quad (3.2)$$

This expression demonstrates that the total compliance can be considered as springs in series, simply adding the separate components. From equation 3.2 it is thus seen that if the modulus is constant, a plot of  $C_t$  vs  $A^{-0.5}$  is linear for a given material, and the intercept of the plot is a direct measure of the machine compliance. This value can be determined by making a number of indents in a well annealed aluminum crystal with high purity. Aluminum is chosen for its low hardness and nearly elastic isotropy, making it possible to produce large enough indents. The indents are imaged after testing in order to measure the area of the indent. The total compliance is determined from the inverse of the unloading slope for each indentation ( $dh/dF$ ). The machine compliance can be deduced from the plot of the compliance verse the reciprocal of the measured indentation area. Once this value is determined it is entered into the software and used to correct raw data accordingly. In this work, the machine compliance used is  $2.1 \text{ nm/mN}$ .

For DSI, accurate knowledge of the indenter tip shape and contact area is crucial, because the hardness and Young's modulus of elasticity depend on the contact areas derived from the

measured depths. A Berkovich tip has an idealized area function  $A_{\perp}$ . However, no tip is perfect because perfect tip shape is difficult to achieve; furthermore, the indenter tip will become blunt during using and its shape significantly affects the prediction of mechanical properties, that is why the tip area function has to be determined experimentally.

Rewriting equation 2.21, the contact area related to the contact stiffness can be described as:

$$A_c = \frac{4}{\pi} \left( \frac{S}{E_r} \right)^2 \quad (3.3)$$

This means the contact area could be determined from measuring the stiffness of a material with a known reduced modulus. Fused quartz, with an extremely consistent measured modulus of  $E = 72$  GPa and Poisson's ration  $\nu = 0.17$  is used in tip calibrations. For a diamond indenter with  $E = 1147$  GPa and  $\nu = 0.07$ , the reduced modulus derived from equation 2.20 is 69.6 GPa. The amorphous structure of fused quartz also enables the consistent deformation behavior of the material. It does not display some of the discrepancies between the actual and the calculated contact area, sometimes displayed in metals. For example it does not experience distortion in the contact area that is caused by pile-up or sink-in. Fig. 3.6a shows numerous load-displacement plots performed on fused quartz with different maximum forces. Fig. 3.6b is an image of a typical fused quartz surface after indentation testing. It can be seen that the indentation behaviour of fused quartz is extremely repeatable; the loading behavior is identical in every trial and the depth of penetration is consistent for a given load. This demonstrates the consistent nature crucial for accurate tip shape calibration. Indentation tests are executed over the desired range of contact depth by changing the maximum loading force. The stiffness is taken from each of these indents and a corresponding projected area is calculated using equation 3.3. Then the contact area is plotted as a function of contact depth. All points are then fit to fifth order polynomial given by the following equation:

$$A_c = C_0 h_c^2 + C_1 h_c + C_2 h_c^{1/2} + C_3 h_c^{1/4} + C_4 h_c^{1/8} + C_5 h_c^{1/16} \quad (3.4)$$

where  $C_0 = 24.5$  and the rest are curve fitting parameters. Fig. 3.7 is a plot of the calculated projected contact area as a function of the contact depth for the Berkovich indenter used in all of experiments. This results in the following tip area function:

$$A_c = 24.5 h_c^2 + 5.96 \cdot 10^3 h_c - 2.58 \cdot 10^5 h_c^{1/2} + 2.45 \cdot 10^6 h_c^{1/4} - 6.05 \cdot 10^6 h_c^{1/8} + 3.89 \cdot 10^6 h_c^{1/16} \quad (3.5)$$

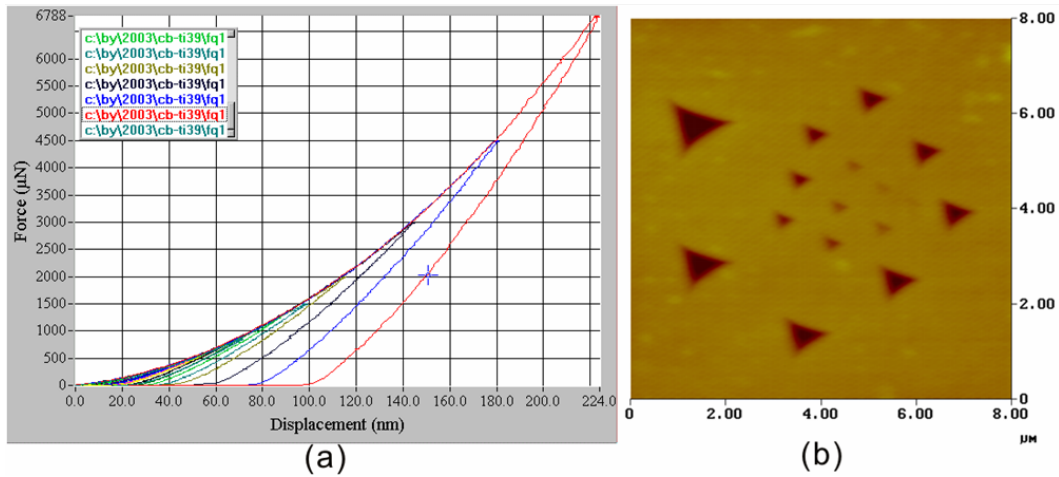


Figure 3.6: Nanoindentation tests on fused quartz for tip calibration. (a) Load-displacement curves; (b) Surface image after testing.

However, the indenter tip will become blunt with increasing using time, especially when hard materials are indented. The tip shape needs frequent calibration to create a new area function for later measurements. Therefore, in this work we only compare nanoindentation results performed in a period with the same area function.

### 3.4.2 In-situ bending AFM

The in-situ bending AFM used in this work was developed after Göken et al. [Gök02], who performed in-situ bending experiments to study the fracture behavior of NiAl single crystals in an AFM. A Photograph of the 4-point-bend loading device AFM used by Göken et al. is shown in Fig. 3.8, including a piezostack with a maximum extension of  $40 \mu\text{m}$  and a pressure bar with stain gauge with which the loading force at every step can be measured. The geometry of specimen (NiAl single crystal) with four ceramic cylinders (as the pivot) in the loading machine is shown in Fig. 3.9.

This equipment has been manifested to be a powerful tool to study the fracture behaviour, deformation processes at crack tips and crack-dislocation interaction of intermetallics [Veh79, Veh80, Veh97, Tho99]. As an example, Fig. 3.10 shows the deformation processes at crack tips of a pre-cracked NiAl single crystal during a 4-point-bending experiment imaged in-situ by AFM. With gradual increasing of the load, dislocations emission from the crack tip and crack

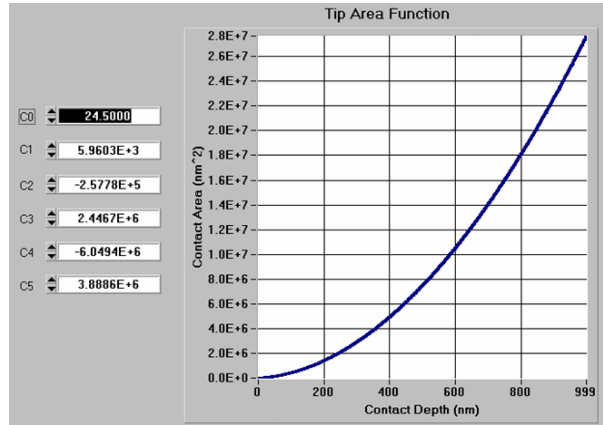


Figure 3.7: Plot of the calculated contact area as a function of contact depth of the Berkovich indenter.

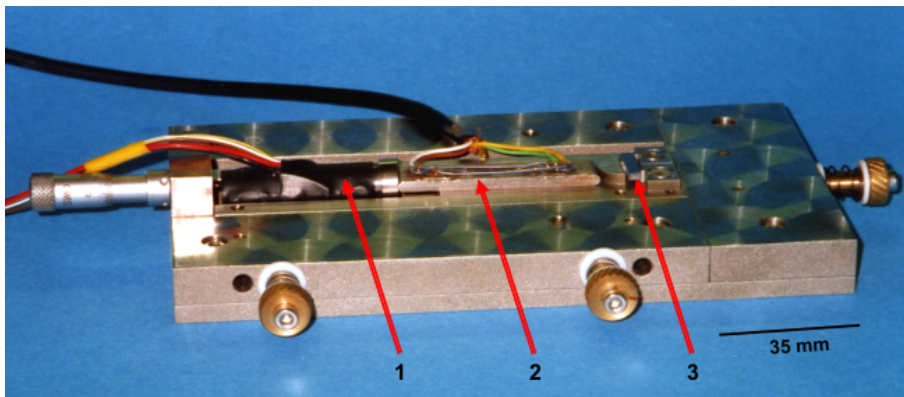


Figure 3.8: Photograph of the loading device for 4-point-bend experiment. 1. Piezostack; 2. Pressure bar with strain gauge; 3. Specimen.

propagation were clearly revealed. Therefore, we expect to use this equipment to study the fracture behaviour of bulk NC nickel. However, since the NC nickel is ductile and does not fail in a brittle fracture manner, this equipment has to be further developed:

1. The maximum extension of the piezostack ( $40 \mu\text{m}$ ) is not sufficient. Even with the maximum extension of the piezostack, the produced bending moment is too small and no plastic deformation at the crack tip could be detected by AFM. This problem is solved by attaching a manual loading handle (labeled as 1 in Fig. 3.11) to increase the bending moment;
2. To in-situ image the deformation process near the crack tip, the scan area has to be kept

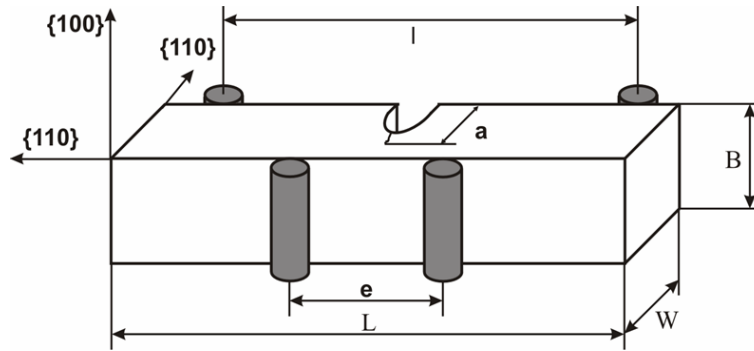


Figure 3.9: Schematic of 4-point-bending NiAl single crystal in soft orientation ( $l=13.5$  mm,  $e=3$  mm,  $B=2$  mm,  $W=3$  mm,  $a=0.89$  mm).

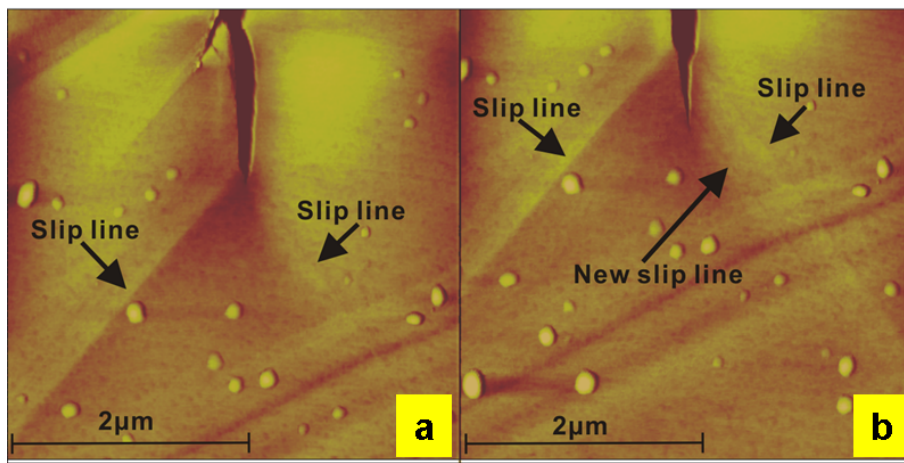


Figure 3.10: In-situ bending AFM images of the deformation process near the crack tip of a NiAl single crystal. (a) Slip lines formed by emission of dislocations from the crack tip and (b) emerging of a new slip line during crack propagation. The scan area is  $4 \times 4 \mu\text{m}$ .

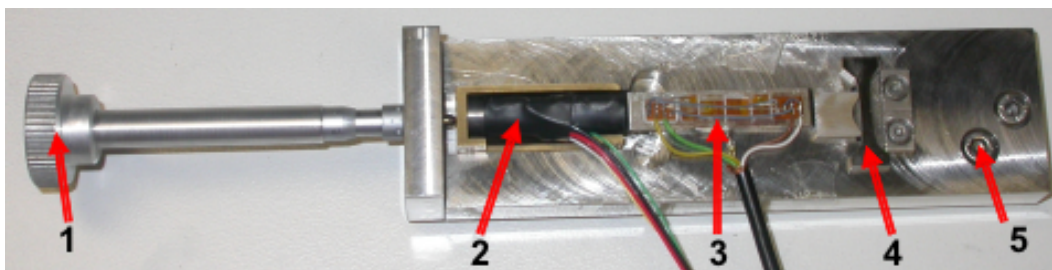


Figure 3.11: Photograph of the bending machine. 1. Manual loading handle; 2. Piezostack; 3. Pressure bar with strain gauge; 4. Specimen; 5. Setscrew.

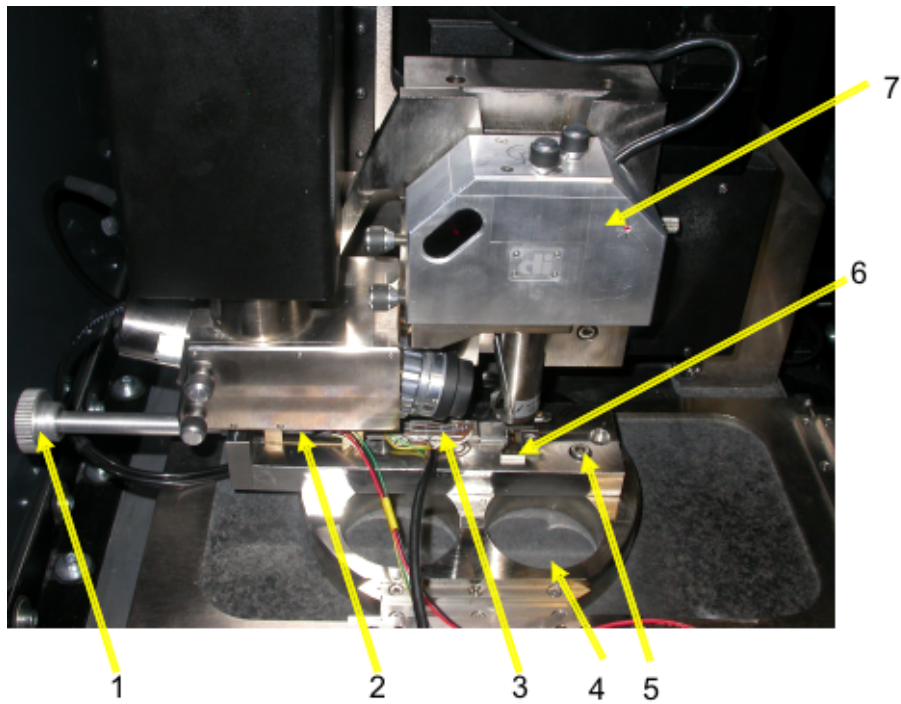


Figure 3.12: Schematic diagram of the developed in-situ bending AFM. 1. Manual loading handle; 2. Piezostack; 3. Pressure bar with strain gauge; 4. Mobile stage; 5. Setscrew; 6. Specimen; 7. SPM head.

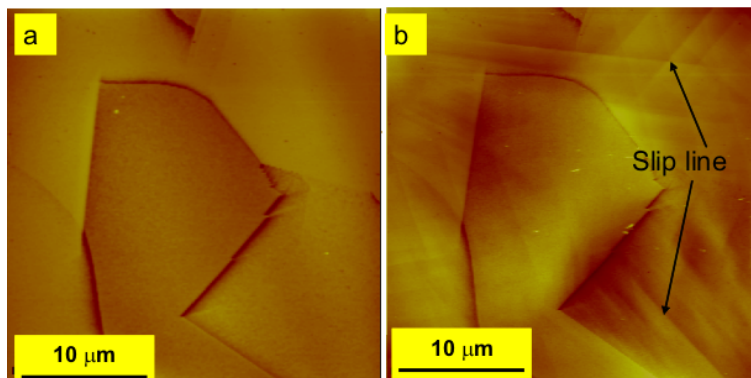


Figure 3.13: In-situ AFM imaging the deformation process of coarse-grained nickel during bending. (a) Surface image before bending; (b) Surface image after bending. Obvious slip lines appear after bending.

very small (about  $5\mu\text{m} \times 5\mu\text{m}$  or smaller, see Fig. 3.10 as an example). With increasing the bending moment step by step for further deformation, the whole bending machine moves inevitably; to relocate the old image area as soon as possible, one key to the design criteria is to reduce the displacement of the bending machine to the minimum extent. To do this, a setscrew (labeled as 5 in Fig. 3.11) is attached to fix the bending machine with the mobile stage of the image system AFM (Dimension 3000);

3. The shape of the bending machine has to be redesigned with a more compact structure in purpose to cope with the AFM.

The new bending machine after development combined with the AFM (Dimension 3000) is shown in Fig. 3.12. It keeps all the functions of the former and extends the applicability to ductile specimens; in addition, in-situ imaging of the deformation process at very large plastic strain can be achieved easily. As an example, Fig. 3.13 shows the AFM images of the as-prepared CG nickel before and after bending. After bending obvious slip lines appear, showing the clear evidence of dislocation activities.

## 3.5 Influences of specimen preparation on nanoindentation

Nanoindentation plays a critical role in this work and the results of nanoindentation can be critically distorted by specimen surface preparation. Therefore, careful examination is necessary.

### 3.5.1 Mechanical polishing and electropolishing

Mechanical polishing always results in a deformation layer with a high dislocation density on the specimen surface, leading to a higher nanohardness. Therefore, electropolishing must be performed after mechanical polishing to delete this deformation. After electropolishing pop-in appears always during nanoindentation (Fig. 3.14). This is important because pop-in plays an important role for studying the local interaction between dislocations and grain boundaries in single grains, one of the aims of this work.

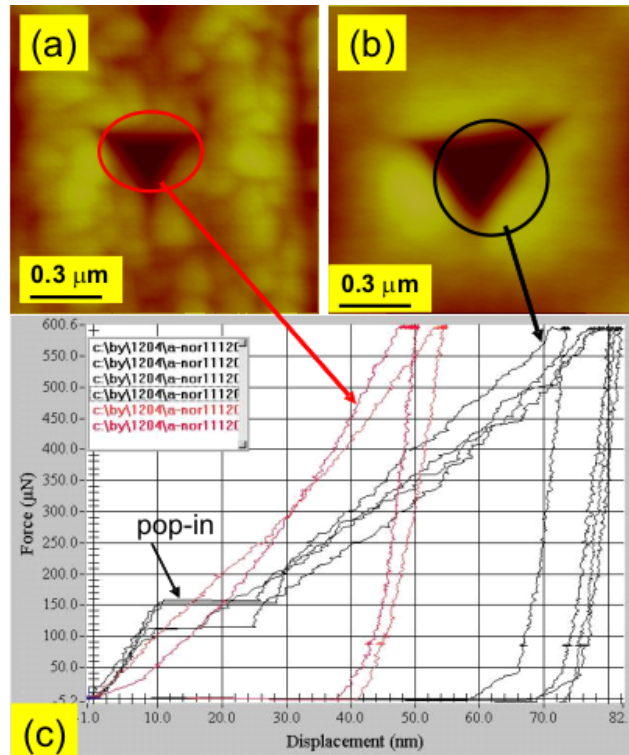


Figure 3.14: Surface effects on nanoindentation with a peak loading force of  $600 \mu\text{N}$ . (a) Mechanically polished surface after nanoindentation; (b) electropolished surface after nanoindentation; (c) force-displacement curves. The same material (a nickel single crystal after a heat-treatment at  $800^\circ\text{C}$  for 2 h in vacuum) is used to check the surface effects induced by mechanical polishing and electropolishing. For nanoindentation, the loading and unloading rate is kept constant at  $50 \mu\text{N/s}$ . Before unloading the maximum applied force is held constant for 15 s. No pop-in appears in the sample prepared by mechanical polishing (red curves), after electropolishing (black curves) pop-in appears always.

### 3.5.2 Oxide films

Oxide films on the surface also play a critical role in nanoindentation. In this work, oxide films are normally formed when a fresh electropolished surface (free of oxide film) is exposed to the air. The thickness of the film increases with the exposing time. Fig. 3.15 shows the force-displacement curves of the nanoindentation on fresh electropolished surface and the same surface exposed to the air for seven days. The specimen is an annealed nickel single crystal.

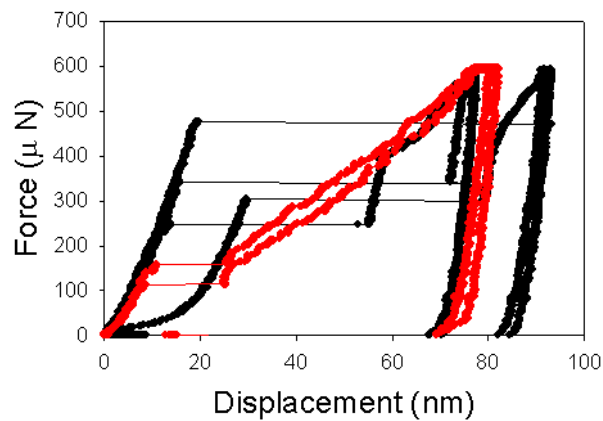


Figure 3.15: Oxide film effects on the force-displacement curves of nanoindentation on an annealed nickel single crystal. The red curves correspond to the tests on the fresh electropolished surface. The black curves correspond to the tests on the same surface after being exposed to air in one day. Hardness and pop-in behaviour of the fresh surface are almost the same but scatter significantly in the latter.

Considerable variability of mechanical behaviour can be seen: the pop-in force, pop-in width and the scatter of hardness increases significantly in the latter.

The oxide film effects on nanoindentation are more prominent for NC nickel. The F-h curves of nanoindentation on fresh electropolished NC nickel and the same surface after being exposed to air for seven days are shown in Fig. 3.16. In the latter nanohardness increases greatly and a pop-in appears during one of the unloading parts of the F-h curves, which could be attributed to the breaking of the oxide films.

Therefore, nanoindentation experiments are accomplished on freshly electropolished surfaces to reduce the effects of oxide films.

### 3.5.3 Roughness

Real surfaces are never ideally flat. Often there are even a variety of scales to the surface modulations. On a macroscopic scale roughness has little effect on indentation testing, as long as the indent is large compared to the asperity size [Tab51]. Traditionally this means that the finish of the surface and the indenter are not significant concern. However, in nanoindentation the

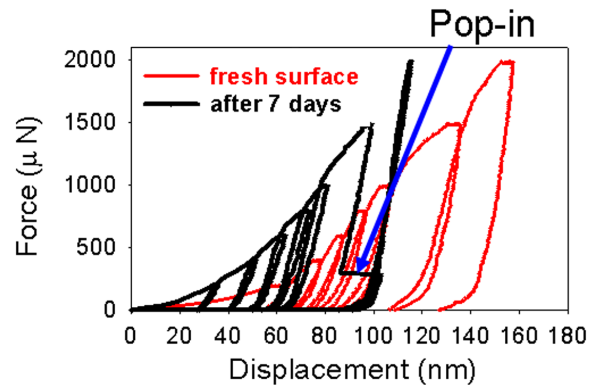


Figure 3.16: Oxide film effects on the force-displacement curves of nanoindentation on NC nickel (No.62). Multi-load function is used. The red and black curves correspond to the tests on the fresh electropolished surface and on the same surface after being exposed to air for seven days, respectively. Nanohardness increases greatly in the latter. A pop-in appears during one of the unloading parts of the F-h curves.

roughness can lead to significant error in the calculated contact area. DSI analysis techniques are based on the Sneddon elastic contact model, which states that there is a single point of contact [Sne65]. In nanoindentation, a rough surface can cause numerous points of contact with an indenter. The non-uniform contact increases the localized stress at the points of intersection, deforming the material to a greater depth at relatively low loads. This can result in a greater displacement and lower calculated hardness for a rough surface compared to a smooth one. Study on the surface roughness of an annealed nickel single crystal in this work leads to the following conclusions:

1. Roughness significantly increases the scatter in hardness, especially at small depths.
2. Roughness significantly decreases the frequency of pop-in appearance.

# 4 Results

Series of NC nickel (labelled as No. 59, 62, 87 etc.) were tested. These as-deposited NC specimens, even with the same grain size, exhibit different mechanical properties (see appendix A). This is likely caused by their different electrodeposition parameters used. Therefore, it is difficult to compare these results with each other for the study of grain size effects. In the following, all hardness (both microhardness and nanohardness) listed together for comparison are results from the specimens (as-deposited and heat-treated) produced from the same as-deposited NC bulk plate; NC specimens (as-deposited and heat-treated) for tensile experiments were from as-deposited NC bulk plates produced with the same electrodeposition parameters; since force-displacement curves recorded in nanoindentation play a critical role and they are greatly influenced by the tip radius, results used for comparison are from experiments performed in a period during which no other harder materials were indented to avoid the change of the tip radius.

## 4.1 Microstructure

### 4.1.1 Microstructure of as-prepared nickel

#### 4.1.1.1 As-prepared coarse-grained nickel

The surface microstructure of as-prepared CG nickel after chemical etching imaged by AFM is shown in Fig. 4.1. Grain size about 20  $\mu\text{m}$  can be seen. However, chemical etching is not used in later experiments because the resulting surface roughness is too high and would influence the nanoindentation results greatly.

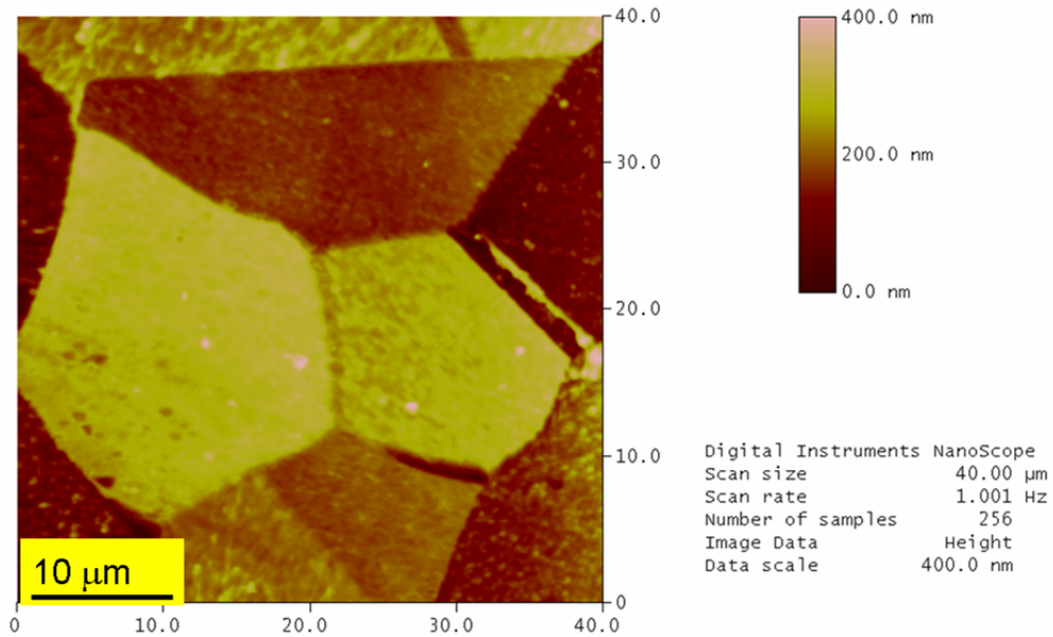


Figure 4.1: Surface structure of CG nickel after chemical etching imaged by AFM. The solution is distilled water (10 ml) +  $HNO_3$  (38 ml) +  $CH_3COOH$  (100 ml).

#### 4.1.1.2 As-prepared nanocrystalline nickel

- An AFM image of the microstructure of as-deposited NC nickel (No. 87) is shown in Fig. 4.2. An average grain size  $\bar{D} = 21.2$  nm and a standard deviation of  $\delta = 10.5$  nm is measured by AFM from surface sectioning [Nan96].
- TEM images of the same NC nickel are shown in in Fig. 4.3, confirming a fairly narrow grain size distribution with a mean grain size smaller than 30 nm. Careful examination of the microstructure shows growth twins and that the grain interior appears to be clean and free of dislocations. No second phase particles are observed at grain boundaries. A selected area diffraction (SAD) pattern is shown as an inset in Fig. 4.3b.
- Using the method of Krill et al. [Kri98], the XRD measurements (Fig. 4.4) of the same as-deposited NC nickel result in a mean grain size of  $\bar{D} = 22.2$  nm and a standard deviation of  $\delta = 7.7$  (method: Cauchy size broadening/Gaussian strain broadening). No obvious texture is detected by X-ray diffraction.

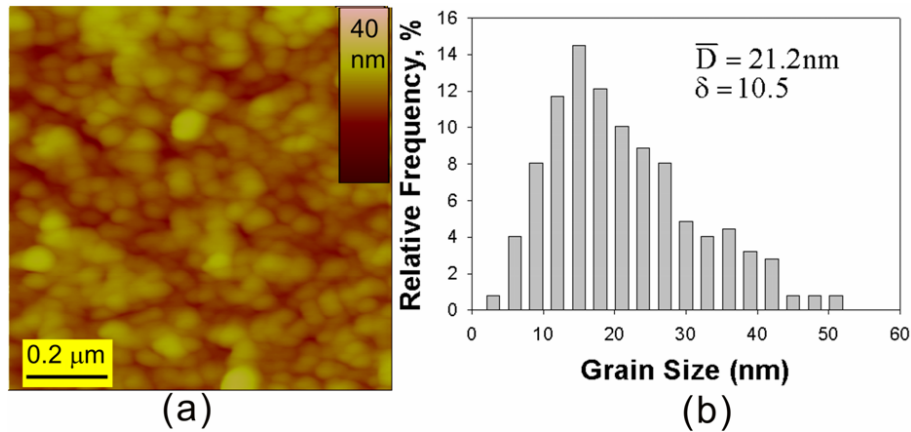


Figure 4.2: Microstructure of as-deposited NC nickel (No. 87). (a) AFM image; (b) Grain size distribution measured by AFM from surface sections.

#### 4.1.1.3 Microstructure of heat-treated nickel

The microstructure evolution of NC nickel with heat treatments was investigated by AFM, SEM and TEM. Selected images of the as-deposited NC nickel after different heat treatments are presented in Fig. 4.5. All AFM images are made with the same AFM tip. Starting with the original grain size of 21.2 nm, AFM detects little grain size growth (24 nm) for a heat-treatment at 150°C for 0.5 h (Fig. 4.5a). For a heat-treatment at 170°C for 0.5 h, a slight grain growth is detected (Fig. 4.5b), the mean grain size measured by AFM from surface section is about 37 nm. With a heat-treatment time increasing to 4 h at the same temperature, significant abnormal grain growth has occurred. Fig. 4.5c shows the surface grains of nanonickel after 4 h at 170°C. A few grains have grown to sizes of about 0.5 μm, while the surrounding small nanosized grains still show the original features. Annealing at 210°C for 2 h results in broad grain size distributions as well, and with more larger grains (Fig. 4.5d). Heat-treatments for 2 h at 250°C, 280°C and 300°C produce relatively homogenous grain size distribution and the mean grain size increases with increasing annealing temperature. The microstructures are shown in Fig. 4.5e-g, respectively. It is interesting to note that a new stage of abnormal grain growth is observed when the annealing time increases to 4 h. Most of the grains remain in the range of 0.2–1 μm, while huge grains with a size larger than 10 μm appears (Fig. 4.5h). This behaviour of abnormal grain growth is even more pronounced at higher annealing temperature ( at 440°C) with grains about 100 μm, as shown in the SEM image (Fig. 4.5i).

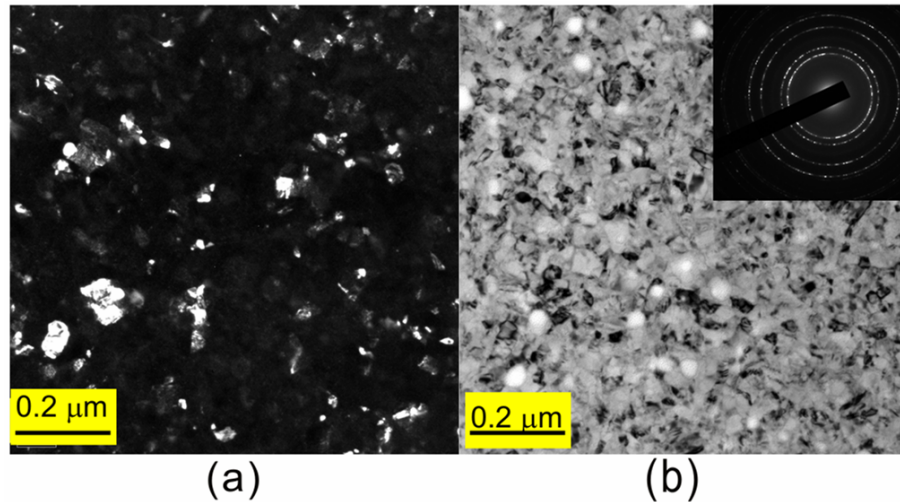


Figure 4.3: TEM images of the microstructure of as-deposited NC nickel (No. 87). (a) Dark field TEM image; (b) Bright field TEM image. The SAD pattern is overlapped. The experiments are performed with a Jeol 2010 operated at 200kV.

TEM observation gives similar results (Fig. 4.6). The mean grain size of as-deposited NC nickel and that of heat-treated specimens are summarized in table 4.1.

## 4.2 Microhardness

No significant difference in microhardness values is obtained with different maximum loading forces, for this reason, only results from maximum loading force of 4900 mN are listed. The results for as-deposited and heat-treated polycrystalline nickel are listed in table 4.1.

Microhardness as a function of mean grain size produced by different heat-treatments on NC nickel is plotted in  $H_V$  vs.  $d^{-0.5}$  to check the H-P relation, as shown in Fig. 4.7. In the grain size range from about  $40 \mu\text{m}$  to the original grain size about 22 nm, the curve separates in three segments with decreasing grain size:

1. For heat-treated nickel (segment 1 and 2), microhardness always increases with decreasing grain size, but with different H-P slope values.
  - For grain size larger than about 700 nm (segment 1), a H-P relation  $H_1 = 0.3 + 73d^{-0.5}$  can be deduced;

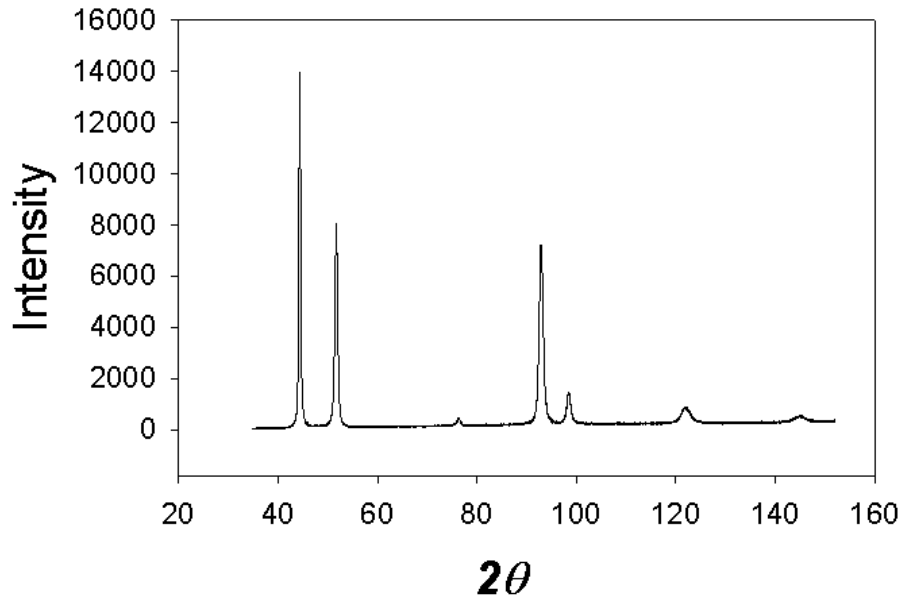


Figure 4.4: XRD pattern of as-deposited NC nickel (No. 87). The experiment is made with a Siemens D500 X-ray detector.

- For grain sizes smaller than 700 nm down to about 24 nm (segment 2), a relation  $H_2 = 3.5 + 7.0d^{-0.5}$  is measured with a much lower slope of  $k = 7.0nm^{0.5}GPa$ ;
2. When the microhardness of as-deposited NC nickel is compared with the heat-treated nickel (segment 3), the microhardness decreases with decreasing grain size.

### 4.3 Nanohardness and reduced modulus

As shown in section 3.5, specimen preparation affects the nanoindentation results greatly; therefore all specimens must be carefully prepared. Electropolishing is needed to remove the deformation layers after mechanical polishing and, most important, to reveal the grain boundaries in order to perform nanoindents in the center of grains with NI-AFM; nanoindentation must be executed on freshly prepared specimen to reduce the oxide film effects.

Different peak forces from 100  $\mu\text{N}$  to 4000  $\mu\text{N}$  are used. The peak force is held for 15 s to test for creep effects. The loading and unloading rate was kept constant at 50  $\mu\text{Ns}^{-1}$ . At 10% of the peak force after unloading the force was kept constant for 5 s to check the drift effects.

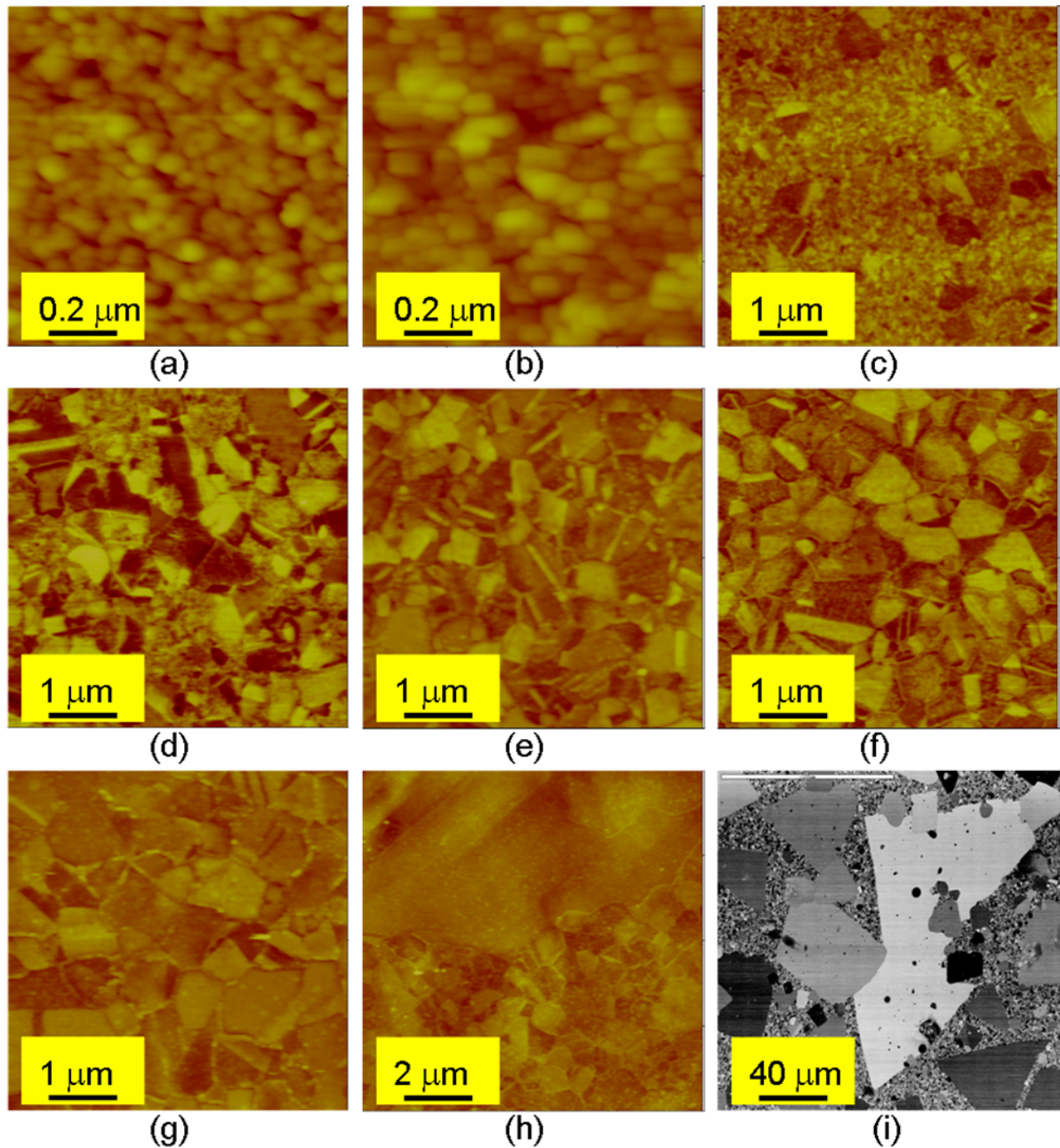


Figure 4.5: Grain structure after different heat-treatments on as-prepared NC nickel (No. 87).

AFM images of NC nickel after heat-treatment at (a) 150°C for 0.5 h; (b) 170°C for 0.5 h; (c) 170°C for 4 h; (d) 210°C for 2 h; (e) 250°C for 2 h; (f) 280°C for 2 h; (g) 300°C for 2 h; (h) 300°C for 4 h; (i) SEM image of abnormal grain growth at annealing temperature at 440°C.

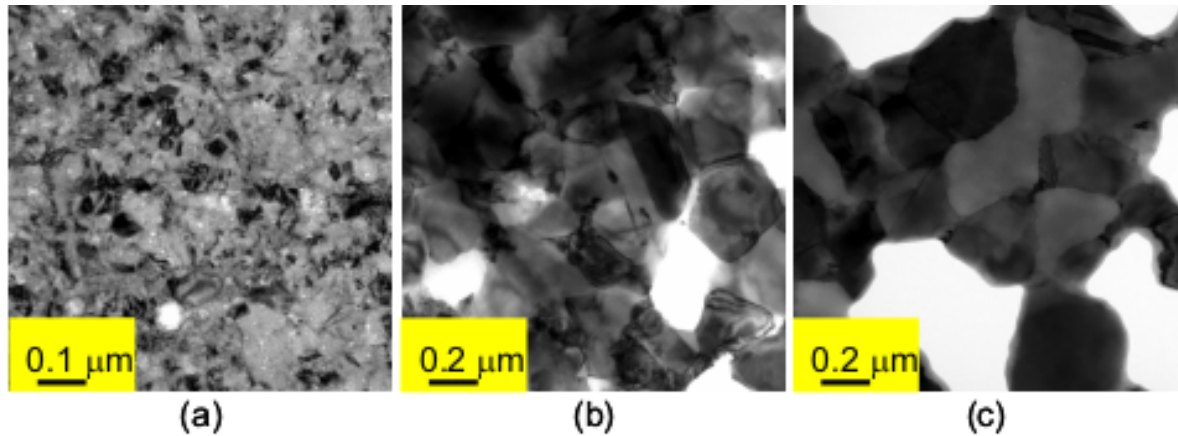


Figure 4.6: TEM observation of microstructure after different heat-treatments on as-prepared NC nickel (No. 87). (a) 150°C for 0.5 h; (b) 210°C for 2 h; (c) 300°C for 2 h.

The load function of nanoindentation with a peak force of 250  $\mu\text{N}$  is shown in Fig. 4.8.

### 4.3.1 Effects of grain boundaries and triple points

Nanoindenting on grain boundaries and on triple points result in higher nanohardness but lower modulus than indenting in the center of a grain. Fig. 4.9 shows this effect clearly. Many reasons, such as different grain boundary stiffness, segregation or more interface volume near the grain boundary than in the centre of grain, could be responsible for the observed behaviour; moreover, as the grain boundaries and triple points always form a depressed zone at the sample surface after electropolishing, the results of nanoindentation on these positions may be not accurate, because nanoindentation artefacts may exist due to the uneven surface. This increases the scatter in the measured hardness and blurs the individual grain size effect, therefore we only perform nanoindents in the center of the individual grains. In addition, since the measurements (of grain size) are on the surface and no information about the grain boundaries below the indenter are known, the largest grains for a given structure resulted from heat-treatment are always indented in order to get the highest probability to indent middle sections only.

No.	Specimen	Mean Grain Size (nm)	Microhardness $H_V$ (GPa)	Effective modulus (GPa)
1	as-deposited	21.2	$4.72 \pm 0.03$	$170 \pm 10$
2	150°C for 0.5 h	24	$4.97 \pm 0.04$	$193 \pm 8$
3	170°C for 0.5 h	37	$4.67 \pm 0.06$	$203 \pm 11$
4	170°C for 4 h	60	$4.33 \pm 0.05$	$202 \pm 9$
5	190°C for 2 h	80	$4.26 \pm 0.06$	$200 \pm 10$
6	210°C for 2 h	250	$3.87 \pm 0.04$	$204 \pm 7$
7	250°C for 2 h	450	$3.02 \pm 0.05$	$210 \pm 10$
8	280°C for 2 h	720	$2.52 \pm 0.05$	$203 \pm 18$
9	300°C for 2 h	900	$2.07 \pm 0.05$	$202 \pm 17$
10	800°C for 2 h	40,000	$0.9 \pm 0.04$	$200 \pm 20$

Table 4.1: Mean grain size and microhardness of as-deposited and heat-treated specimens prepared from NC nickel (No. 87).

### 4.3.2 Nanoindentation with peak force 2000 $\mu\text{N}$

For the convinence of comparison, nanohardness  $H$  related to the grain size is plotted in the form of  $H$  vs.  $d^{-0.5}$ , as shown in Fig. 4.10. In the whole grain size range five different segments can be observed for nanohardness:

1. For grain sizes larger than 6  $\mu\text{m}$ , nanohardness keeps almost constant (segment 1);
2. In the grain size range of about 6  $\mu\text{m}$  to 1  $\mu\text{m}$ , nanohardness increases with decreasing grain size (segment 2) and a H-P relationship of  $H_2 = 1.1 + 66d^{-0.5}$  roughly holds;
3. In the grain size range of about 1  $\mu\text{m}$  to 300 nm, nanohardness increases or decreases with decreasing grain size (segment 3);
4. In the grain size range of about 300 nm to 24 nm, nanohardness increases again with decreasing grain size (segment 4). A H-P relationship of  $H_4 = 3.37 + 7.21d^{-0.5}$  can be deduced. The H-P slope value is much smaller than that of segment 2.

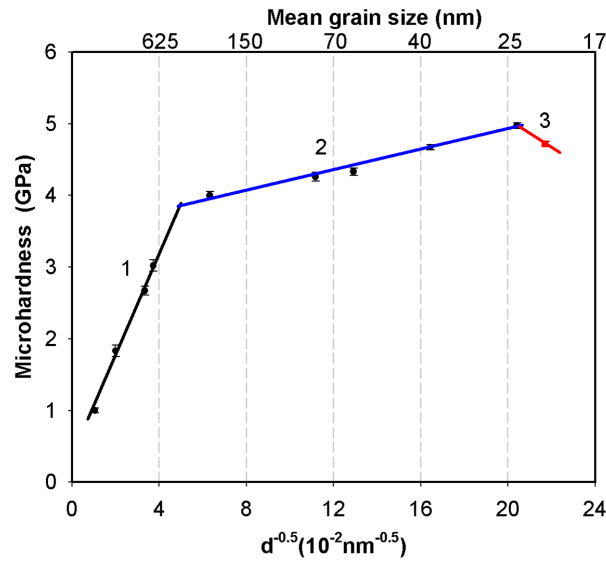


Figure 4.7: Microhardness vs. mean grain size. Different grain sizes are produced on as-deposited NC nickel (No. 87).

5. In the smallest grain size range (24 nm to the original grain size of about 21.2 nm), nanohardness decreases with decreasing grain size. Here the slight increase in grain size is produced by heat treatment at low temperatures. This so called reverse H-P behaviour has been observed in microindentation (segment 3 of Fig. 4.7).

The measured elastic modulus by nanoindentation are plotted in the same diagram and can be divided into two segments, as labelled as I and II in the diagram. It remains almost constant (segment I of Fig. 4.10) except a decrease about 15% for the as-deposited NC nickel (segment II of Fig. 4.10).

## 4.4 Strain rate sensitivity and activation volume

### 4.4.1 Strain rate sensitivity examined by nanoindentation

#### 4.4.1.1 Definition of strain rate sensitivity under indentation

The strain rate sensitivity (SRS)  $m$  under indentation is expressed by:

$$m = \partial H / \partial \dot{\epsilon}_i \quad (4.1)$$

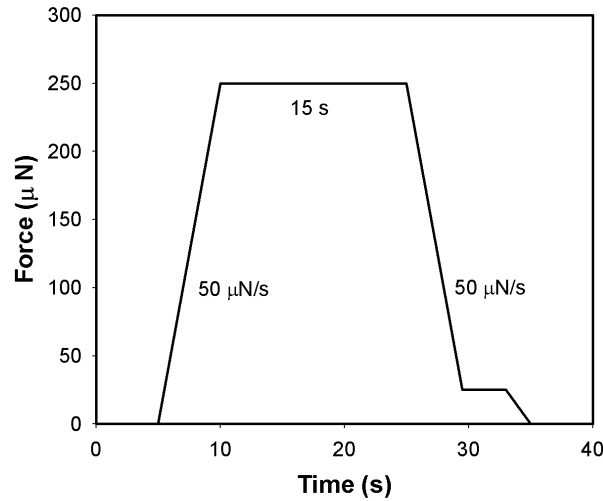


Figure 4.8: Schematic of load functions of nanoindentation with a peak force of 250  $\mu\text{N}$ .

where  $H$  is the hardness and  $\dot{\epsilon}_i$  the strain rate defined for conical and pyramidal indenters as [Poi95, May88]:

$$\dot{\epsilon}_i = \frac{1}{h} \cdot \frac{dh}{dt} \quad (4.2)$$

where  $h$  is the displacement at a given time. In this work we use a force-controlled nanoindenter, hence the strain rate  $\dot{\epsilon}_i$  in equation 4.2 is difficult to define. The indenting rate ( $dF/dt$ ) is used and applied to equation 4.1 to estimate the strain rate effect for simplification.

#### 4.4.1.2 Strain rate sensitivity studied with peak load 4000 $\mu\text{N}$

The load functions are shown in Fig. 4.11. The peak loading force is 4000  $\mu\text{N}$  with different indenting rates 10, 100 and 1000  $\mu\text{N/s}$ , the unloading rate is constant for 100  $\mu\text{N/s}$ . The maximum loading force is defined as 4000  $\mu\text{N}$ . The indent produced with this load is always larger than 1  $\mu\text{m}$ , ensuring that more grains (smaller than 1  $\mu\text{m}$ ) in UFG specimens are indented and the nanoindenter can work more like a microindenter. The results for CG, UFG and as-deposited NC nickel are listed in table 4.2. It can be seen that the SRS increases with decreasing grain size; furthermore, SRS calculated at lower indent rate range is higher than that calculated at higher indent rate range.

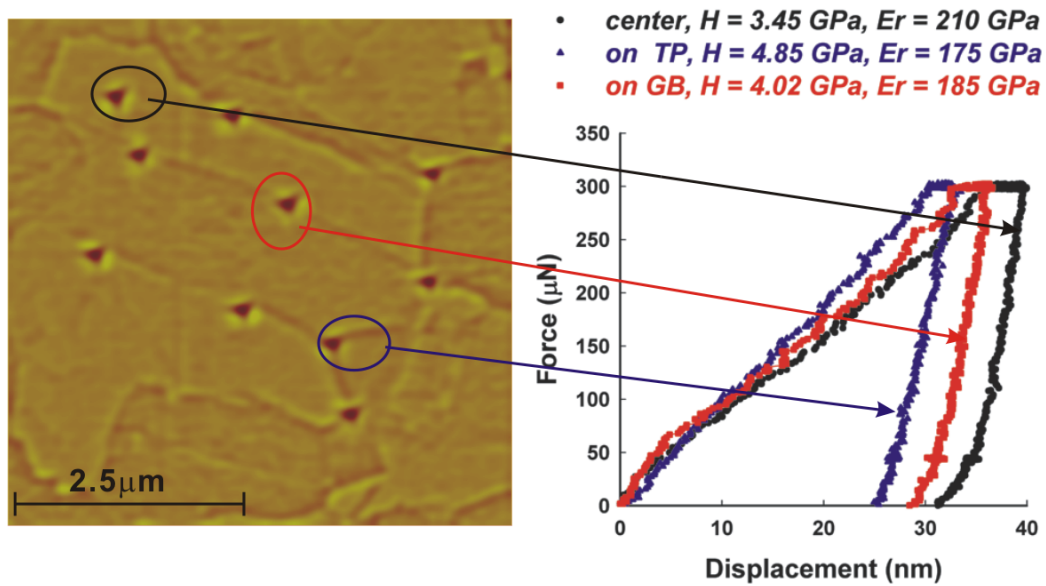


Figure 4.9: Nanoindentation in the center of a grain, at grain boundaries and at triple points. The results show higher nanohardness but lower modulus when indented at grain boundaries and triple points than in the center of the grain. The sample was produced by heat-treatment on NC nickel (No. 62).

#### 4.4.1.3 Strain rate sensitivity studied with peak load $300 \mu\text{N}$

The load functions are shown in Fig. 4.12. The peak load force is  $300 \mu\text{N}$  with different indenting rate 10, 20 and  $40 \mu\text{N/s}$ , the unloading rate is constant for  $100 \mu\text{N/s}$ . A smaller peak load of  $300 \mu\text{N}$  is chosen to make the indent size smaller (about  $400 \text{ nm}$ ), thus a local examination of grain size effects on the strain rate sensitivity can be achieved by performing the indents always in the center of the individual grains with size from  $400 \text{ nm}$  to about  $1 \mu\text{m}$ . Table 4.3 shows the results for larger grains (grain size about  $850 \text{ nm}$ , all from as-deposited NC nickel after heat-treatment at  $300^\circ\text{C}$  for 2h) and that for smaller grains (grain size about  $450 \text{ nm}$ , all from as-deposited NC nickel after heat-treatment at  $250^\circ\text{C}$  for 2h). Again, SRS increases with decreasing grain size and is enhanced at lower indent rate range.

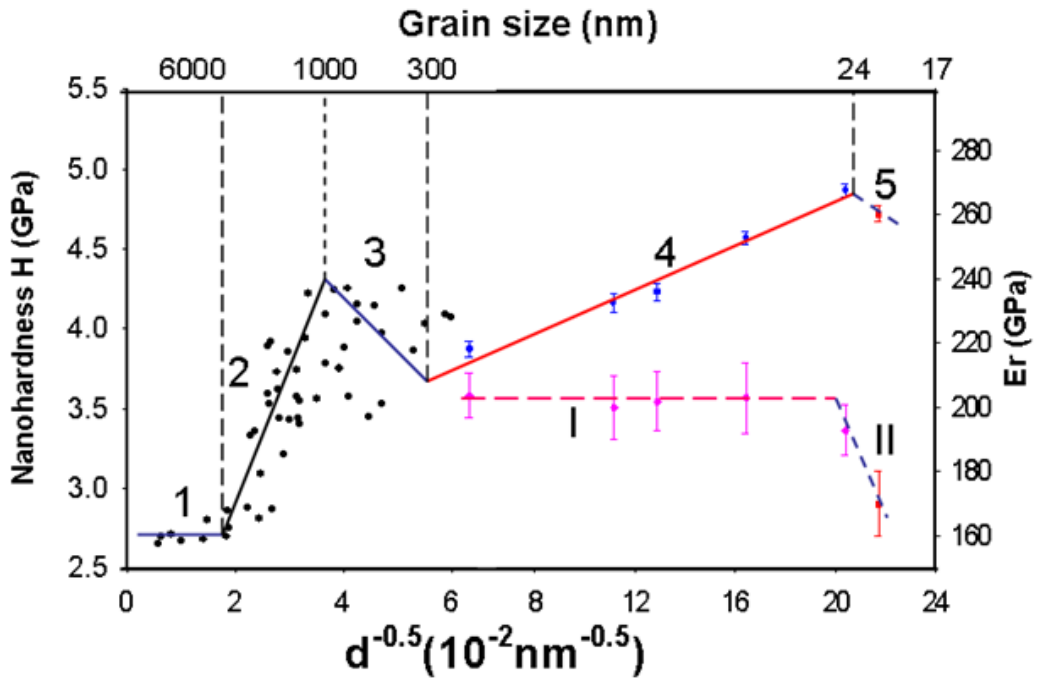


Figure 4.10: Nanoindentation hardness and modulus vs. grain size. With decreasing grain size five different segments for nanoindentation hardness (labeled as number 1, 2, 3, 4, 5) and two segments for modulus (labeled as number I and II) can be observed. The scattered points correspond to a measurement indented in the center of a grain. All specimens were produced from NC nickel (No. 87).

#### 4.4.2 Tensile strain rate jump experiments

Tensile strain rate jump experiments are performed at room temperature in order to study the thermal activation parameters SRS and activation volume (AV) introduced in section 2.2.2.

##### 4.4.2.1 Definition of the strain rate sensitivity and activation volume from a tensile strain rate jump test

The SRS  $m$  and experimental AV  $V_{exp}$  defined from a tensile strain rate jump test at a constant temperature are described as:

$$m = \frac{\partial \ln \sigma}{\partial \ln \dot{\epsilon}} = \ln \frac{\sigma_1}{\sigma_2} / \ln \frac{\dot{\epsilon}_{p1}}{\dot{\epsilon}_{p2}} \quad (4.3)$$

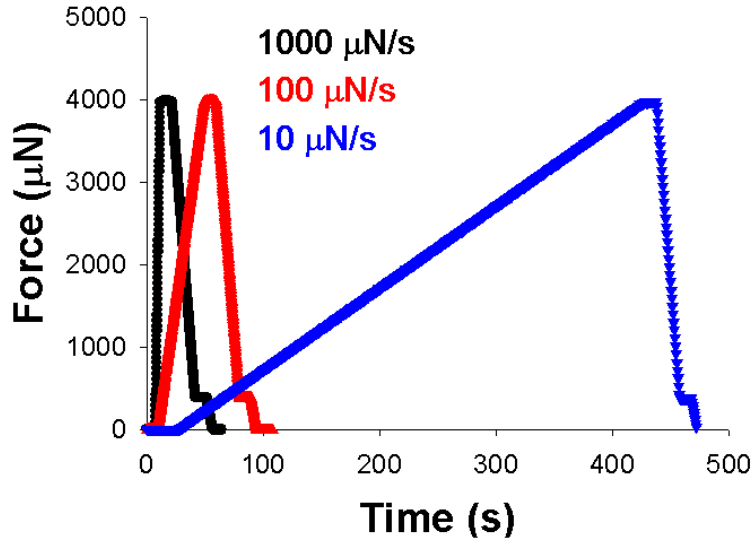


Figure 4.11: Nanoindentation load functions with peak load 4000  $\mu\text{N}$ , different indenting rates 10, 100 and 1000  $\mu\text{N/s}$  and a constant unloading rate 100  $\mu\text{N/s}$ .

Specimen	Mean grain size (nm)	$m_1$	$m_2$
CG (800°C for 2 h)	40,000	0.008	0.004
UFG (210°C for 2 h)	250	0.07	0.035
NC (as-deposited)	21.2	0.12	0.039

Table 4.2: SRS of CG, UFG and as-deposited NC nickel.  $m_1$  is calculated from the lower indent rates (10 and 100  $\mu\text{N/s}$ ) and  $m_2$  from the higher indent rates (100 and 1000  $\mu\text{N/s}$ ). All specimens were produced from NC nickel (No. 87).

and

$$V_{exp} = kT \frac{\partial \ln \dot{\epsilon}}{\partial \sigma} = kT \frac{\ln(\dot{\epsilon}_{p1}/\dot{\epsilon}_{p2})}{\sigma_1 - \sigma_2} \quad (4.4)$$

where the parameters  $\sigma$  and  $\dot{\epsilon}_p$  are schematically shown in Fig. 4.13. The effective AV  $V_{eff}$  is related to the experimental AV  $V_{exp}$  as follows:

$$V_{eff} = kT \frac{\partial \ln \dot{\epsilon}}{\partial \tau} = kT \frac{\Delta \ln \dot{\epsilon}}{\frac{\Delta \sigma}{M}} = M \cdot V_{exp} \quad (4.5)$$

where  $M$  is the Taylor factor, which is about 3.06 for a randomly textured specimen tested in uniaxial tension. In the following the AV is expressed in terms of  $b^3$ , where  $b$  is the Burgers vector of the dislocation with a value of 0.249 nm for nickel.

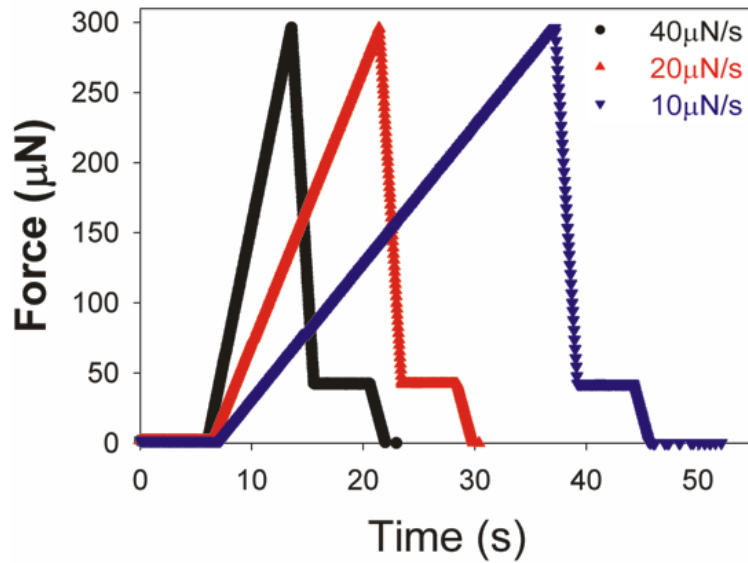


Figure 4.12: Nanoindentation load functions with peak load  $300 \mu\text{N}$ , different indenting rates 10, 20 and  $40 \mu\text{N/s}$  and a constant unloading rate  $100 \mu\text{N/s}$ . All specimens were produced from NC nickel (No. 87).

Specimen	Grain size (nm)	$m_1$	$m_2$
UFG ( $300^\circ\text{C}$ for 2 h)	850	0.032	0.017
UFG ( $250^\circ\text{C}$ for 2 h)	450	0.078	0.056

Table 4.3: SRS in UFG size range.  $m_1$  is calculated from the lower indent rates (10 and  $20 \mu\text{N/s}$ ) and  $m_2$  from the higher indent rates (20 and  $40 \mu\text{N/s}$ ). All specimens were produced from NC nickel (No. 87).

#### 4.4.2.2 Results of tensile strain jump experiments

Due to segregation of impurities at grain boundaries caused by annealing, the UFG and MC nickel produced by heat-treatments failed in very earlier stage in tensile test (details described in appendix B). Therefore, strain rate jump experiments are only performed on as-deposited NC nickel, heat-treated NC nickel ( $170^\circ$  for 4h, grain size about  $60 \text{ nm}$ ) and commercial CG pure nickel with mean grain size larger than  $10 \mu\text{m}$ . The true stress-strain curves of as-deposited NC nickel and CG nickel in tensile strain rate jump experiment are plotted in Fig. 4.14. The curve indicates a remarkable change in the stress at the strain rate change for NC nickel (No.

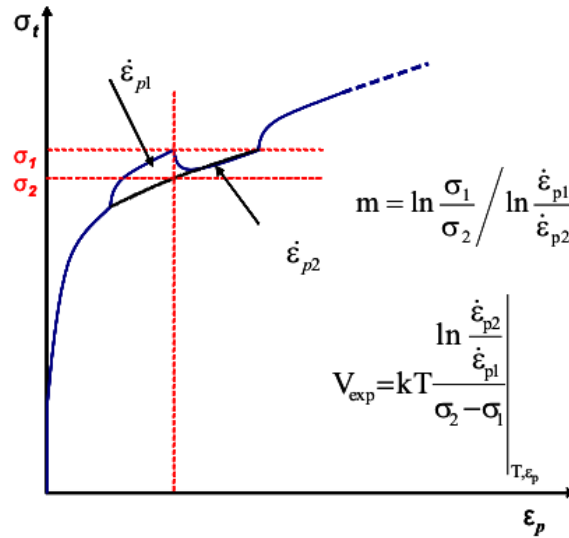


Figure 4.13: Definition of strain rate sensitivity  $m$  and experimental activation volume  $V_{exp}$  from a tensile rate jump test.  $\dot{\epsilon}_{p1}$  and  $\dot{\epsilon}_{p2}$  correspond to the different strain rates used in a strain rate jump.

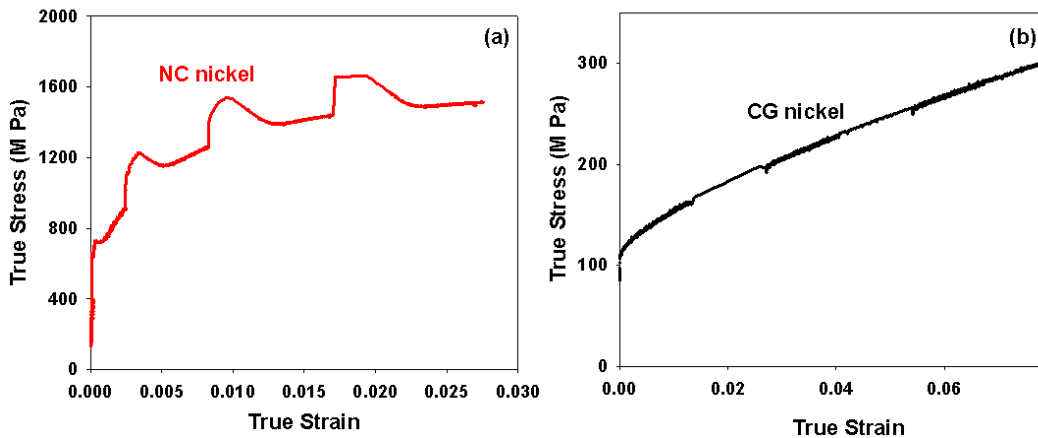


Figure 4.14: True stress-strain curves of as-deposited NC nickel and commercial CG pure nickel in a tensile rate jump test.

104, Fig. 4.14a), while for CG nickel, hardly any change in the stress at the strain rate change can be observed (Fig. 4.14b). According to equations 4.3 and 4.5, the SRS  $m$  and effective AV  $V_{eff}$  of the CG nickel are calculated and plotted as a function of plastic strain, as shown in Fig. 4.15.

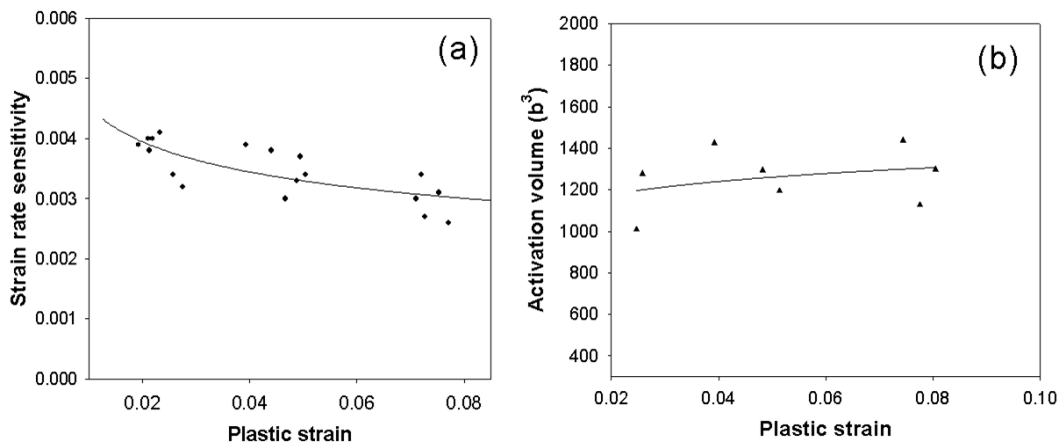


Figure 4.15: Strain rate sensitivity (a) and activation volume (b) of CG nickel as a function of plastic strain.

## 4.5 Stress jump experiments in creep tests

Tensile stress jump experiments are performed on CG, as-deposited NC and heat-treated NC nickel with Instron 8513 tensile machine. The applied stresses at different jump numbers are plotted in Fig. 4.16. The stress in every stage is kept for 9000 s before the next jump. For CG nickel no creep behaviour can be observed. The minimum steady creep rates under different stresses of as-deposited NC nickel (No. 104) are plotted in Fig. 4.17.

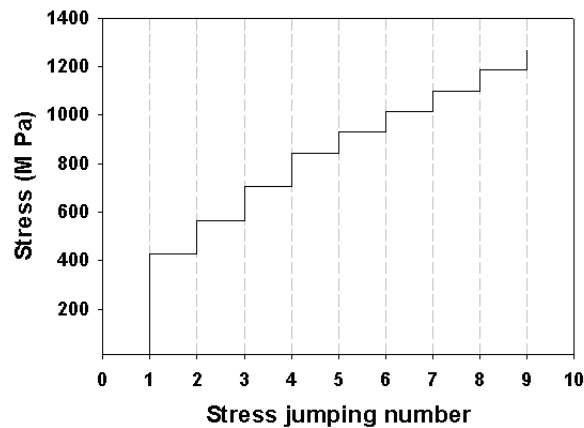


Figure 4.16: Tensile stresses for the different stress jump number from 1 to 9.

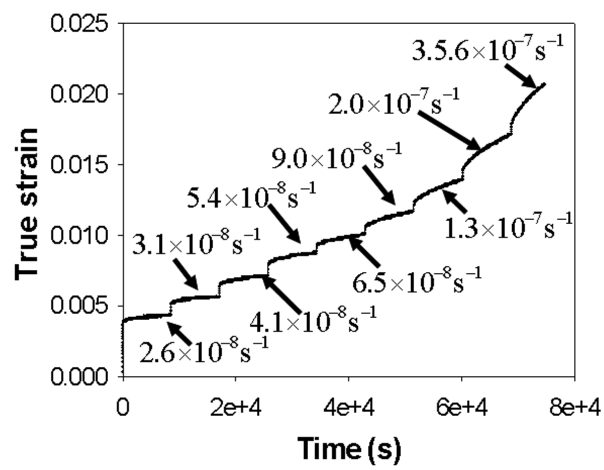


Figure 4.17: Creep rate at different stages.

# 5 Discussion

## 5.1 Nanohardness dependence on the ratio of indent size and grain size

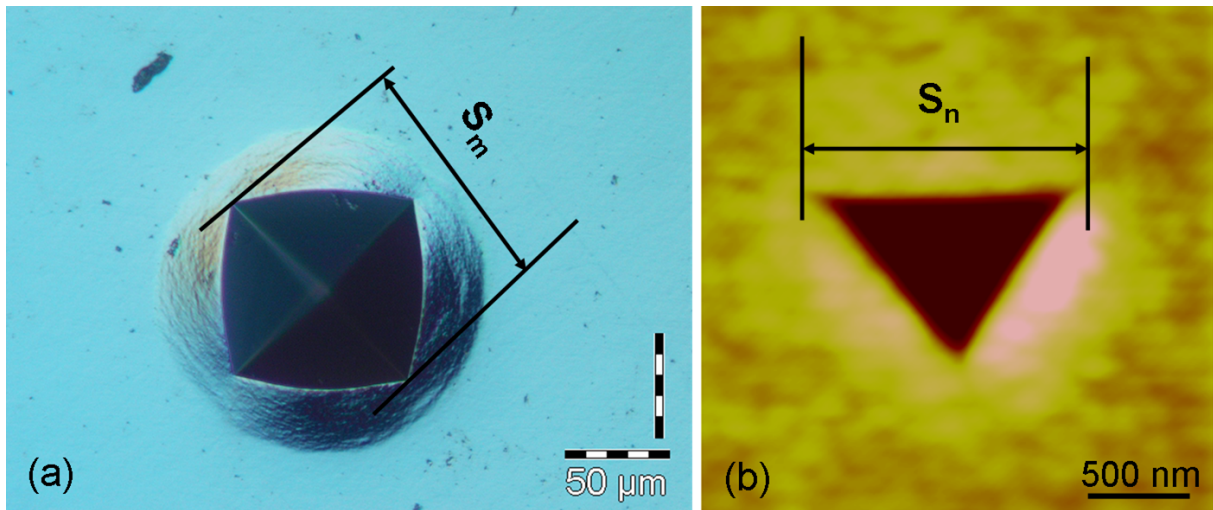


Figure 5.1: Definition of indent size. (a) Optical microscopy of microindentation with a peak force of 4900 mN and (b) AFM image of nanoindentation with a peak force of 2000  $\mu\text{N}$ . The specimen is as-deposited NC nickel (No. 87). The resulted indent size of microindentation  $S_m$  and nanoindentation  $S_n$  are shown.

Comparing the results (from NC nickel 87) of microindentation (peak force of 4900 mN, Fig. 4.7) and nanoindentation (peak force of 2000  $\mu\text{N}$ , Fig. 4.10):

1. For grain size smaller than 300 nm, similar H-P behaviour for microhardness and nanohardness are observed.

2. For grain size larger than 300 nm, microhardness always increases with decreasing grain size, while nanohardness keeps constant (segment 1 of Fig. 4.10), increases (segment 2 of Fig. 4.10), scatters (segment 3 of Fig. 4.10).

The observed behaviour can be explained by the ratio of resulted indent size (as shown in Fig. 5.1) to indented grain size.

For microindentation with a peak force of 4900 mN, the resulted indent size  $S_m$  ranges from about 45  $\mu\text{m}$  to 100  $\mu\text{m}$ , therefore lots of grains are indented. For nanoindentation with a peak force of 2000  $\mu\text{N}$ , the resulted indent size  $S_n$  ranges from about 900 nm to 1400 nm. This means for grains smaller than 300 nm, many grains are indented and the nanoindenter works like a microindenter. Therefore, in this grain size range (grain size smaller than 300 nm, segment 4 and 5 of Fig. 4.10), very similar grain size dependences of microhardness and nanohardness are observed.

The constant nanohardness in the big grain size range (segment 1 of Fig. 4.10) is not surprising, because the grain size is very big compared with the indent size (maximum 1400 nm). In this case we can assume that no dislocation produced by the nanoindenter interacts with the surrounding grain boundaries. Therefore, all these grains, even with different grain sizes, behave like a single crystal and give the same hardness. This assumption will be further checked in the following section 5.2.

With decreasing grain sizes ranging from about 6  $\mu\text{m}$  to 300 nm, nanohardness increases (segment 2 of Fig. 4.10) and then scatters (segment 2 of Fig. 4.10). Around the grain size of about 1  $\mu\text{m}$ , a peak hardness appears.

Similar behaviour are also observed in hardness measurements performed on other specimens and are discussed detailedly below.

### 5.1.1 Microindentation with peak force of 490 mN

Microhardness with a peak force of 490 mN as a function of mean grain size is plotted in  $H_V$  vs.  $d^{-0.5}$  to check the H-P relation, as shown in Fig. 5.2. The curve separates in three segments with decreasing mean grain size (from about 5  $\mu\text{m}$  to 20 nm):

1. For a grain size larger than about 1  $\mu\text{m}$  (segment 1 of Fig. 5.2), a H-P relation  $H_1 =$

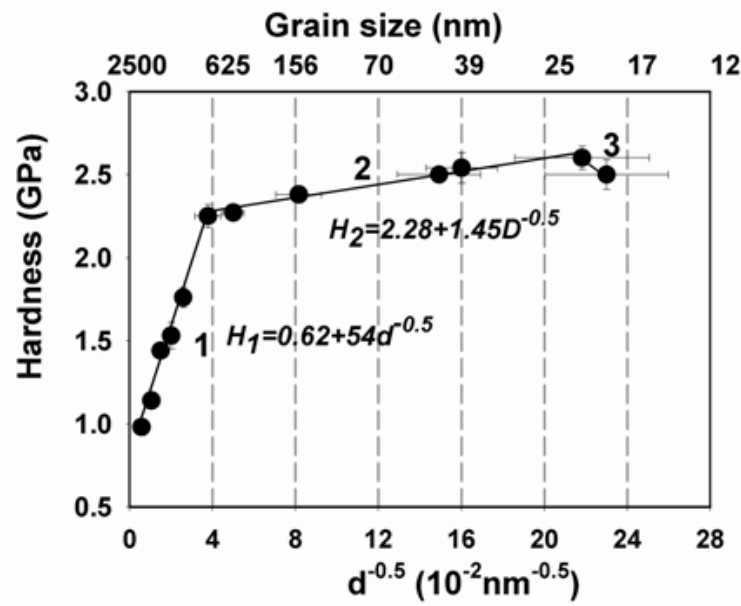


Figure 5.2: Microhardness vs. mean grain size. All specimens were produced from NC nickel (No. 62). The smaller values in segment 3 correspond to the results of as-deposited NC nickel. The resulted indent size ranges from about 19  $\mu\text{m}$  to 31  $\mu\text{m}$ .

$0.62 + 54d^{-0.5}$  fits with  $H_0 = 0.62 \text{ GPa}$  and a slope of  $k = 54 \text{ nm}^{0.5} \text{ GPa}$ .

- For grain sizes smaller than 1  $\mu\text{m}$  down to about 20 nm (segment 2 of Fig. 5.2), a relation  $H_2 = 2.28 + 1.45d^{-0.5}$  is measured but with a much lower slope of  $k = 1.45 \text{ nm}^{0.5} \text{ GPa}$ .
- For grain sizes smaller than about 20 nm (segment 3 of Fig. 5.2, as-deposited nickel), the microhardness decreases with decreasing grain size.

### 5.1.2 Nanoindentation with peak forces of 600 $\mu\text{N}$ , 300 $\mu\text{N}$ and 250 $\mu\text{N}$

The results with a peak force of 600  $\mu\text{N}$  are given in Fig. 5.3. With decreasing grain size the slope changes three times and the curve separates into four segments:

- In the grain size range between 2.5  $\mu\text{m}$  and 900 nm, nanohardness increases (segment 1 of Fig. 5.3e) with a corresponding H-P relation of  $H_1 = 0.7 + 85.9d^{-0.5}$ .

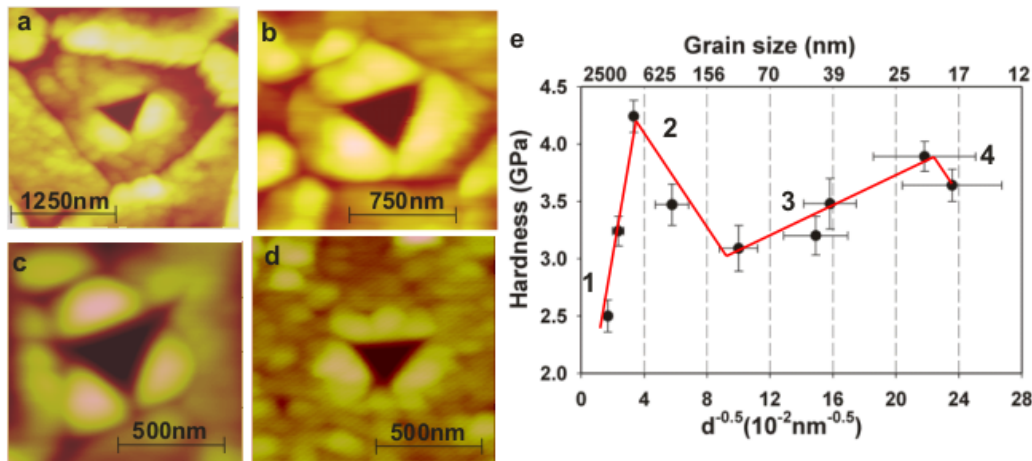


Figure 5.3: Nanohardness vs. grain size with a peak load of  $600 \mu\text{N}$ . All specimens were produced from NC nickel (No. 62).

2. In segment 2 of Fig. 5.3e, nanohardness decreases with decreasing grain size. A larger scatter in the measured nanohardness can be seen.
3. With further decreasing grain size (segment 3 of Fig. 5.3e, smaller than 100 nm), the ratio of indent size to the indented grain size becomes much larger (Fig. 5.3d), and the hardness increases again but with a smaller slope ( $H_3 = 2.0 + 4.5d^{-0.5}$ ).
4. For grain sizes smaller than about 20 nm (as-deposited), the nanohardness decreases with decreasing grain size (segment 4 of Fig. 5.3e). Here the slight increase in grain size is produced by heat-treatment at low temperatures. The same behaviour was also obtained in the microindentation results (segment 3 of Fig. 5.2).

In the smaller grain size range (segment 3 and 4 of Fig. 5.3e), the indent size is much larger than the grain size and the nanoindenter works like a microindenter, similar behaviour to that of nanoindentation with a peak force of  $2000 \mu\text{N}$  (segment 4 and 5 of Fig. 4.10). This would not be further discussed. In addition, we see the hardness decreases with decreasing grain size at the smallest grain size range. The same behaviour was also obtained in the other indentation results (segment 3 of Fig. 4.7, segment 5 of Fig. 4.10, segment 3 of Fig. 5.2). Here the slight increase in grain size is produced by heat-treatment at low temperatures. The so called reverse H-P behaviour would not be further discussed here and can be found in appendix C.

In segment 1, nanohardness always increases with decreasing grain size. It is found that the resulted indent size decreases with the decreasing grain size and is always smaller than the indented grain size (Fig. 5.3(a)). Within its resolution, the AFM detects no deformation outside the indented grain. The plastic deformation, which forms the indent, is confined in the grain. In this range grain boundaries act as barriers to the movement of dislocations (produced during indentation and responsible for the indent). Smaller grains produce smaller plastic zone size and therefore exhibits higher hardness due to their relatively higher dislocation density. A peak of hardness is found at a grain size between 750 nm and 900 nm (Fig. 5.3e), which is just a little larger than the indent size (700 nm) as measured by AFM. This segment is similar to the segment 2 of Fig. 4.10.

In segment 2 nanohardness scatters. It is found that in this range of grain size the indent size is either a little smaller (Fig. 5.3b) or even a little larger than the indented grain size (Fig. 5.3c). Thus, two situations about the plastic zone size related with the indented grain size may appear: (I) the plastic zone size is smaller than the grain size, if the plastic zone were confined only in the grain indented or (II) the plastic zone size is larger than the indented grain size, if the plastic zone spread out of the grain indented. In the first case grains yield higher hardness due to the higher dislocation density resulted from the smaller plastic zone size; in the second case several grains yield, resulting in a larger plastic zone than the former and hence a decrease in hardness. This segment is similar to the segment 3 of Fig. 4.10.

Similar results are also observed by nanoindentation with smaller peak forces.

The nanoindentation results with a peak force of 300  $\mu\text{N}$  are given in Fig. 5.4. Nanohardness first increases to grain size about 600 nm and then decreases with further decreasing grain size. A peak hardness is observed in the grain sizes between 450 nm and 650 nm. From the AFM images we can see that the indent size at the peak load of 300  $\mu\text{N}$  is about 400 nm (Fig. 5.4a-b), which is just a little smaller than the grain size.

The results of nanoindentation in the center of individual grains in ultrafine-grained size range with a peak force of 250  $\mu\text{N}$  are given in Fig. 5.5. From the force-displacement curves, we see hardness increases with decreasing grain size as far as the indent size is smaller than the indented grain size (Fig. 5.5a-c). When the indent size becomes larger than the indented grain size, a decrease in hardness is found (Fig. 5.5d). AFM images show that the indent size at the

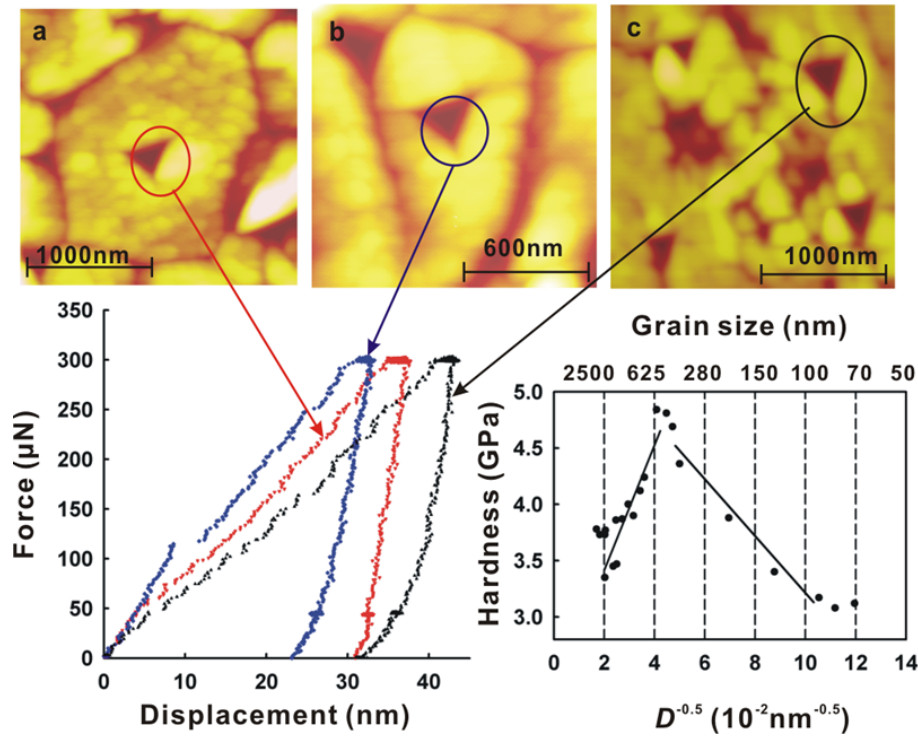


Figure 5.4: Nanohardness vs. grain size with a peak load of  $300 \mu\text{N}$ . All specimens were produced from NC nickel (No. 62).

peak load of  $250 \mu\text{N}$  is about  $250 \text{ nm}$ . The grain size which has the highest hardness is about  $300 \text{ nm}$ , just a little larger than the indent size.

Compared to the results with the peak force of  $2000 \mu\text{N}$  (where the maximum hardness corresponds to a larger grain size of about  $1 \mu\text{m}$ , Fig. 4.10),  $600 \mu\text{N}$  and  $300 \mu\text{N}$ , it clearly proves that this transition only depends on the relation between the indent size and grain size. As the plastic zone spreads out of the single grain, the hardness depends on not only the size of the indented grain, but also the size of surrounding grains. It also explains the larger scatter observed in this grain size range (segment 3 of Fig. 4.10).

### 5.1.3 Conclusion

From the discussions above, we can conclude that nanohardness depends not only on the grain size, but also on the ratio of the indent size and the grain size. For hardness measurements with a nanoindenter, different ranges of grain size related to the indent size should be taken into

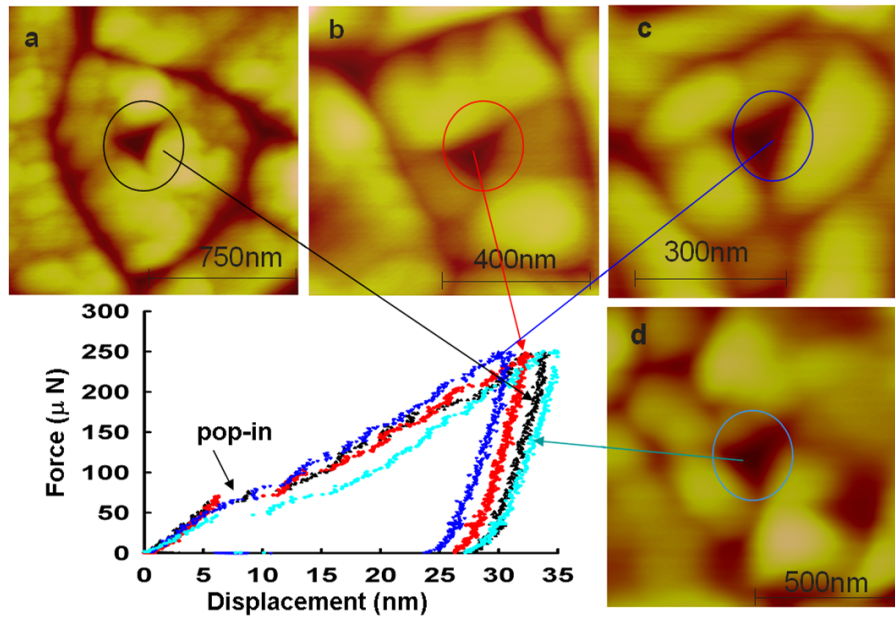


Figure 5.5: Nanoindentation in the center of individual grains with a peak load of  $250 \mu\text{N}$ . All specimens were produced from NC nickel (No. 62).

account:

1. The grain size is much larger than the indent size (segment 1 of Fig. 4.10). In this range, nanohardness remains constant and no grain size effects could be detected.
2. The indent size approaches the grain size (segment 2 and 3 of Fig. 4.10). In this range nanohardness first increases and then scatters with decreasing grain size.
3. The grain size is much smaller than the indent size (segment 4 and 5 of Fig. 4.10). In this range nanoindentation again yields the same results as with a microindenter.

## 5.2 Indentation size effect in individual grains

From section 5.1, we see that when the indent size is smaller than the grain size, nanohardness remains constant, increases and then scatters (increases further or decreases) with decreasing grain size (e.g. segments 1-3 of Fig. 4.10). This provides us an indirect evidence of the local interaction between dislocations and grain boundaries in single grains: the plastic zone size is kept constant (no interaction between dislocations produced during nanoindentation and grain

boundaries), decreases with decreasing grain size (dislocations piled up against grain boundaries) and spreads out of the single grain (activation of new dislocation sources in neighbouring grains due to pile-up of dislocation). However, the following issues are not clear:

1. When the grain boundaries act as barriers of the movement dislocations?
2. What is the relation between the plastic zone size and indentation size?
3. When the plastic zone spread from the indented grain to the neighbouring grains and how about the grain size effects on it?

These issues will be discussed in this section.

### 5.2.1 Schematic diagram of nanoindentation performed in the center of a single grain

For the convenience of discussion, a schematic diagram of nanoindentation performed in the center of a single grain at an indentation depth  $h$  is shown in Fig. 5.6. In this diagram, grain size is denoted as  $d$ , the contact radius denoted as  $a$ . The radius of indentation size is taken to be characterized by  $s$  as denoted in Fig. 5.6b. For simplicity we take

$$s = a \tag{5.1}$$

and the plastic zone size scaled with the contact radius

$$r = f \cdot a \tag{5.2}$$

where  $r$  is the radius of the plastic zone size and  $f \geq 1$ , as treated by other authors [Fen04, Dur05].

The relation between the indentation depth  $h$  and the radius of indentation size  $s$  can be deduced from the area ( $A_c$ ) function of an ideal Berkovich indenter (without tip bluntness):

$$A_c = 24.5h^2 = \frac{3\sqrt{3}}{4}s^2 \tag{5.3}$$

We have

$$s \approx 4.35h \tag{5.4}$$

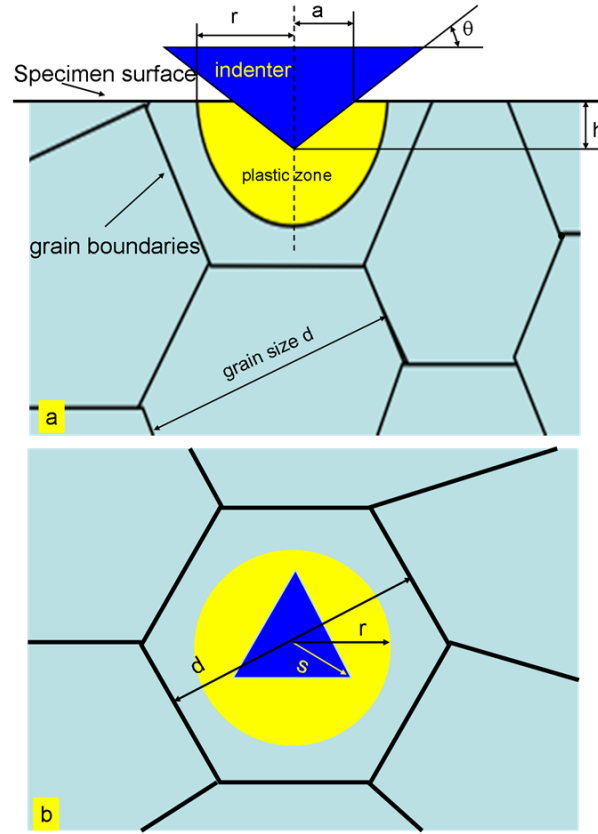


Figure 5.6: Schematic of nanoindentation performed in the center of a grain. The plastic zone size is assumed to be a hemisphere with a radius  $r$ . The grain size is denoted as  $d$ , the contact radius is denoted as  $a$ , the indentation size is denoted as  $s$ , the indentation depth is denoted as  $h$ ,  $\theta$  is the angle between the surface of the indenter and the plane of the sample surface.

For a blunt tip with radius  $R$ , as schematically shown in Fig. 5.7, a height supplement  $\Delta h$  has to be considered and equation 5.4 is then:

$$s \approx 4.35(h + \Delta h) \quad (5.5)$$

Taking the end of blunted pyramidal indenter as a pommel with the same area function of an ideal Berkovich indenter (Fig. 5.7), we have

$$24.5(R - R\cos\alpha)^2 = \pi(R\sin\alpha)^2 \quad (5.6)$$

This results in an apex angle  $\alpha = 20^\circ$  and

$$\Delta h = \frac{R}{\cos\alpha} - R = 0.064R \quad (5.7)$$

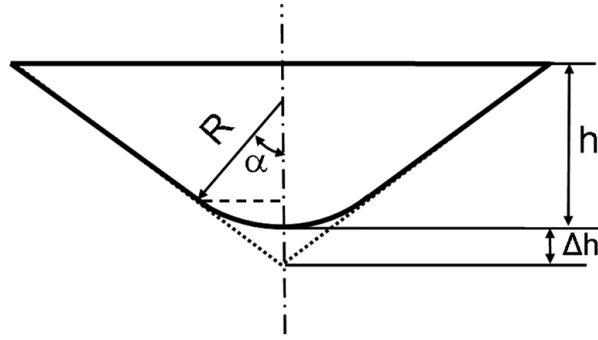


Figure 5.7: Schematic of the indenter with a tip radius  $R$ . The end of blunted pyramidal indenter is taken as a pommel with the same area function of an ideal Berkovich indenter (the dotted line).  $\alpha$  is the apex angle.

Equation 5.5 is

$$s \approx 4.35(h + 0.064R) \quad (5.8)$$

This gives the relationship between the plastic zone size  $2r$  and the indentation depth  $h$ :

$$2r = 2f \cdot a = 2f \cdot s = 8.7f(h + 0.064R) \quad (5.9)$$

In this work, the tip radius of the indenter is about 200 nm, thus equation 5.9 is

$$2r = f \cdot 2s = 8.7f(h + 13) \quad (5.10)$$

### 5.2.2 Indentation size effect vs. Grain boundary effect

Nanohardness of the individual grain sizes at different indentation depth is shown in Fig. 5.8. The results of grains of size about 80  $\mu\text{m}$ , 1350 nm and 850 nm are presented. With increasing indentation depth in the given indentation depth range:

1. For the grain with size of 80  $\mu\text{m}$  nanohardness always decreases;
2. For the individual grains with size of about 1350 nm, nanohardness first decreases (segment 1 of Fig. 5.8), then increases (segment 2 of Fig. 5.8), and decreases (segment 3 of Fig. 5.8) again, resulting in two extreme points (labelled as  $E_1$  and  $E_2$ ). The first extreme point (minimum hardness)  $E_1$  corresponds to an indentation depth of about 31 nm. The

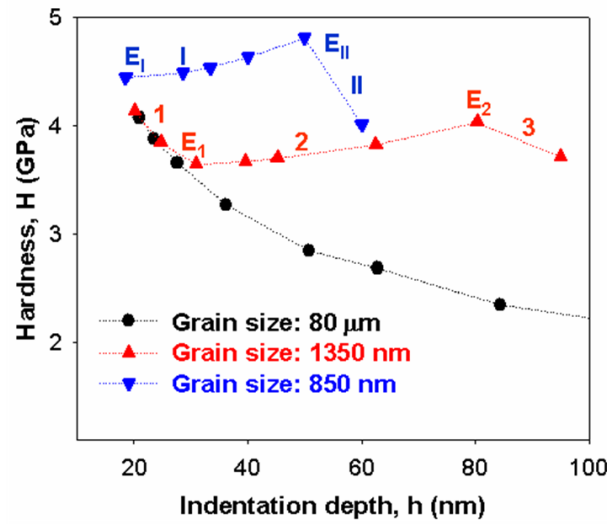


Figure 5.8: Nanohardness ( $H$ ) vs. Indentation depth ( $h$ ). Different peak forces from  $100 \mu\text{N}$  to  $4000 \mu\text{N}$  were used to produce different indentation size related to the indented grain size. The loading and unloading rates were kept constant for  $50 \mu\text{N/s}$ . All specimens were produced from NC nickel (No. 87).

second extreme point (maximum hardness)  $E_2$  corresponds to an indentation depth of about 85 nm.

- For the individual grains with size of about 850 nm, two segments are observed. Nanohardness increases from the smallest indentation depth about 18 nm to the depth of about 48 nm (segment I of Fig. 5.8), then decreases (segment II of Fig. 5.8). The extreme points are labelled as  $E_I$  and  $E_{II}$  respectively.

Considering the small indentation depth (maximum 100 nm), the grain with size of  $80 \mu\text{m}$  can be treated as a single crystal. Therefore the decrease in nanohardness with increasing indentation depth observed here is not surprising and can be explained by the normal indentation size effect (ISE) always observed in single crystals. According to the NG-model (details described in section 2.5.5.3) of ISE [Nix98], a linear relationship would be found in the plot of  $H^2$  vs.  $h^{-1}$  (equation 2.38).

For a double check, plots of  $H^2$  vs.  $h^{-1}$  according to the data in Fig. 5.8 are made, as shown in Fig. 5.9. A linear relationship between  $H^2$  and  $h^{-1}$  can be seen for the coarse grains with

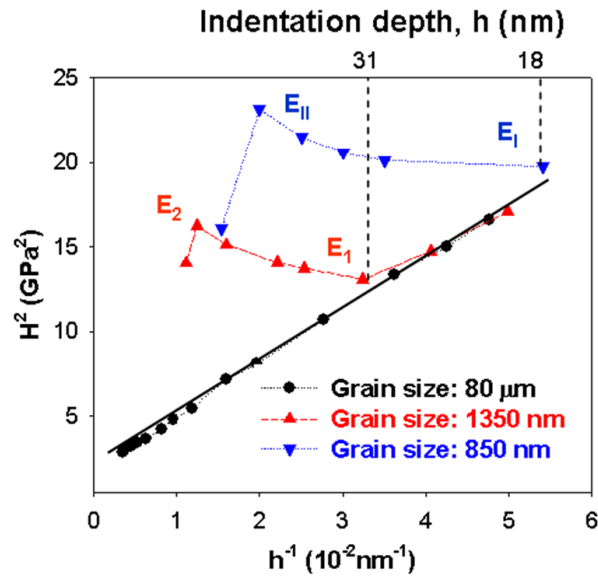


Figure 5.9: Examination of the indentation size effect in single grains with plots of  $H^2$  vs.  $h^{-1}$  according to the data in Fig. 5.8.

size of about  $80 \mu\text{m}$  in the given indentation depth range, which is in good agreement with the predictions of the equation 2.38.

From Fig. 5.9, we also see that at low indentation depth ranges (smaller than 31 nm) the data of the grains with size of about 1350 nm and the data of coarse grains ( $80 \mu\text{m}$ ) fell roughly on the same line. This means that at this smaller indentation depth range, the same indentation depth resulted in the same size of plastic zone for smaller grains as that of the larger grains. In this case hardness depends mainly on the indentation size and not on the grain size. It also explains why the nanohardness is kept constant in the grain size range 1 in Fig. 4.10.

With indentation depth larger than 31 nm, opposite behaviour of the smaller grains (1350 nm) to that of coarse grain ( $80 \mu\text{m}$ ) was observed: hardness increases with increasing indentation depth, and the normal ISE does not work. This results from the existence of grain boundaries which interact directly with the GNDs produced during indentation.

As mentioned in section 2.5.5.3, in the NG-model, the effect of interface was not taken into account. The density of GNDs  $\rho_G$  depends on the total length  $\lambda$  of the GNDs and the plastic volume  $V$  in which the GNDs contained. In addition, the volume of indent formed in the grain during indentation,  $V_{indent}$ , which also increases with indentation depth  $h$ , is ignored. As a

result of  $\lambda \propto h^2$  (equation 2.32) and the plastic zone volume  $V \propto h^3$  (equation 2.33), hardness decreases with increasing  $h$ .

For single grains with grain boundaries, with further increasing indentation depth,  $\lambda$  is the same as described in equation 2.32, but equation 2.33 does not hold anymore. Grain boundaries may obstacle the movement of dislocations, therefore the plastic deformation is confined in the indented single grains, resulting in a change of the relation between the plastic zone volume  $V$  and indentation depth  $h$ .

At the point that the plastic zone produced reaches the surrounding grain boundaries, assuming the plastic zone is also a hemisphere, the volume of plastic zone  $V$ , according to Fig. 5.6, is then defined by the radius of the grain size  $d$  and can be described as:

$$V = \frac{\pi}{12}d^3 \quad (5.11)$$

In addition, it is also necessary to take the volume of indent formed in the grain during indentation  $V_{indent}$  into account, and the actual plastic zone volume  $V$  should be:

$$V = \frac{\pi}{12}d^3 - V_{indent} \quad (5.12)$$

$$V_{indent} = \gamma \cdot h^3 \quad (5.13)$$

where  $h$  is the indentation depth and  $\gamma$  a constant depending on the real shape of the indenter (bluntness).

Assuming that the indented single grain has a real volume  $V_{grain}$  and the plastic zone is confined in the grain with the increasing indentation depth  $h$ , the actual plastic zone volume  $V$  can be written as:

$$V = \beta \frac{\pi}{12}d^3 - V_{indent} \quad (5.14)$$

where  $\beta$  is a factor increasing from 1 to a constant value smaller than  $V_{grain}/(\frac{12\pi}{d^3})$ . Then the density of GNDs  $\rho_G$  can thereby be written as:

$$\rho_G = \frac{\lambda}{V_d} = \frac{\frac{\pi}{b} \cdot \frac{h^2}{\tan\theta}}{\beta \frac{\pi}{12}d^3 - V_{indent}} \quad (5.15)$$

In this case, equation 2.37 described in the NG-model changes to:

$$\sqrt{\frac{H}{H_0}} = \sqrt{1 + \frac{\rho_G}{\rho_s}} = \sqrt{1 + \frac{h^2}{h_0^* \cdot \beta \cdot d^3 - \gamma^* \cdot h^3}} \quad (5.16)$$

where  $h_0^*$  depends on  $\rho_s$  through  $H_0$  (equation 2.36) and  $\gamma^*$  is a constant.

Equation 5.16 indicates that hardness will increase with increasing  $h$  when the grain boundaries obstacle the spreading of the plastic zone. This explains why hardness increases with increasing indentation depth  $h$  after a critical indentation depth for grains with size of about 1350 nm.

Equation 5.16 also indicates that at a constant indentation depth  $h$ , the smaller grains will exhibit higher hardness. It can be concluded that hardness  $H$  depends not only on the individual grain size  $d$ , but also on the indentation depth  $h$ .

### 5.2.3 Indentation size vs. plastic zone size

Assuming that at the critical indentation depth (corresponding to the extreme point  $E_1$  in Fig. 5.8) the produced plastic zone reaches the surrounding grain boundaries, then according to Fig. 5.9 we have

$$r = f \cdot a = f \cdot s = d/2 \quad (5.17)$$

Combining equation 5.10 results in  $f = 3.5$  for the grains with size of 1350 nm at an indentation depth of 31 nm. This means that the radius of plastic zone is about 3.5 times of the contact radius.

This explains why the hardness of the individual grains with size of about 850 nm always increases with increasing indentation depth (see Fig. 5.8). According to equation 5.10 and taking the same value  $f = 3.5$ , at an indentation depth of 18 nm the plastic zone size reaches about 950 nm, which is larger than the indented grain size. This means that the dislocations below the indenter tip interact directly with the surrounding interfaces for this grain sizes and plastic zone is confined in the indented grain. In this case,  $\rho_G$  increases with the indentation depth  $h$  (equation 5.15), hence an increase in the nanohardness occurs.

### 5.2.4 The spreading of the plastic zone out of the indented single grains

From Fig. 5.8 we see that hardness for the individual grains with size of about 1350 nm and 850 nm do not always increases with increasing  $h$ , but begin to decrease after a certain value. This

results in an extreme point of maximum in hardness for both grains ( $E_2$  and  $E_{II}$  in Fig. 5.8).

A decrease in hardness with increasing  $h$  indicates a decrease in the dislocation density. This would happen, considering that at a sufficient large  $h$  the indentation size  $2s$  would eventually exceed the indented grain size  $d$  (Fig. 5.6). In this case the factor  $\beta$  in equation 5.14 would become larger than  $V_{grain}/(\frac{12\pi}{d^3})$ , depending how many surrounding grains are indented and the grain sizes of these indented grains. This increases the volume of plastic zone volume  $V$  and thus decreases the dislocation density, leading to a decrease in hardness.

This extreme point corresponds to an indentation depth of 48 nm for the grain with size of about 850 nm, and 80 nm for the grain with size of about 1350 nm. According to equation 5.10, at  $h = 50$  nm the indentation size  $2s = 530.7$  nm, smaller than the indented grain size 850 nm. At  $h = 80$  nm the indentation size  $2s = 809$  nm, also smaller than the indented grain size 1350 nm. According to equation 5.16, hardness will increase with increasing  $h$  if only the plastic zone is confined within the indented grain. Therefore, the decrease in hardness with increasing  $h$  observed here, i.e. the increase in the plastic volume  $V$ , must result from the spreading of the plastic zone out of the indented grains to surrounding grains. This is a direct evidence of the activation of new dislocation sources in the neighbouring grains caused by the pile-up of dislocations. Before this happens, a higher maximum hardness for the smaller grains (850 nm) than that of the larger grains (1350 nm) was found, indicating that the smaller the grain size, the higher dislocation density resulted in the grain. It also means that for a larger grain, a smaller external applied load is needed to activate the new dislocation sources in neighbouring grains. This agrees with the well-known dislocation pile-up model of the H-P effects.

### 5.2.5 Conclusion

By performing nanoindentations always in the centre of individual grains and changing the grain sizes systematically, the influence of lateral boundary conditions on the indentation size effect was for the first time studied. Different indentation depth dependences of nanohardness were observed, depending on the relationship between the grain size and the produced plastic zone size. The different indentation depth (size) dependences of hardness reflect the local interaction between dislocations and grain boundaries in single grains.

1. When the dislocations nucleated below the indenter do not interact directly with the surrounding interfaces, hardness decreases with increasing indentation depth. Direct interaction between dislocations and grain boundaries was observed for grains smaller than about 850 nm.
2. When the grain boundaries act as barriers for the movement of dislocations and the plastic zone is confined in the indented grains, hardness depends on both grain size and indentation size. Hardness of single grain increases with increasing indentation depth. At a constant indentation depth, the smaller grains will exhibit higher hardness due to a higher dislocation density. That the radius of the plastic zone is about 3.5 times of the contact radius was deduced.
3. With further increasing indentation depth, a decrease in hardness is found, resulting in a maximum hardness. This is due to the spreading of the plastic zone out of the indented single grains at a critical indentation depth, a direct evidence of the activation of new dislocation sources in the neighbouring grains caused by the pile-up of dislocations. Smaller grains show a higher maximum hardness value compared with the larger grains, meaning that for a larger grain a smaller external applied load is needed to activate the new dislocation sources in neighbouring grains. This agrees with the well-known dislocation pile-up model of the H-P behaviour.

### **5.3 Direct observation of dislocation-boundary-interaction in ultrafine grains**

From the discussions described above, we know that to reveal the local interaction between dislocations and grain boundaries by nanoindentation directly,

1. the indent size, depending mainly on the indent force and the tip radius, must be controlled to be smaller than the indented grain size;
2. individual grains in the UFG size range are desirable. In this grain size range, dislocations produced during indentation interact directly with the grain boundaries.

Taking these consideration into account, a peak force of  $300 \mu\text{N}$  (load function see Fig. 4.8) is finally chosen after many experiments, and nanoindentations are always performed in the center of individual grains with sizes ranging from about 200 nm to some micrometer. The post-indentation images in-situ imaged by NI-AFM and the corresponding F-h curves are shown in Fig. 5.10.

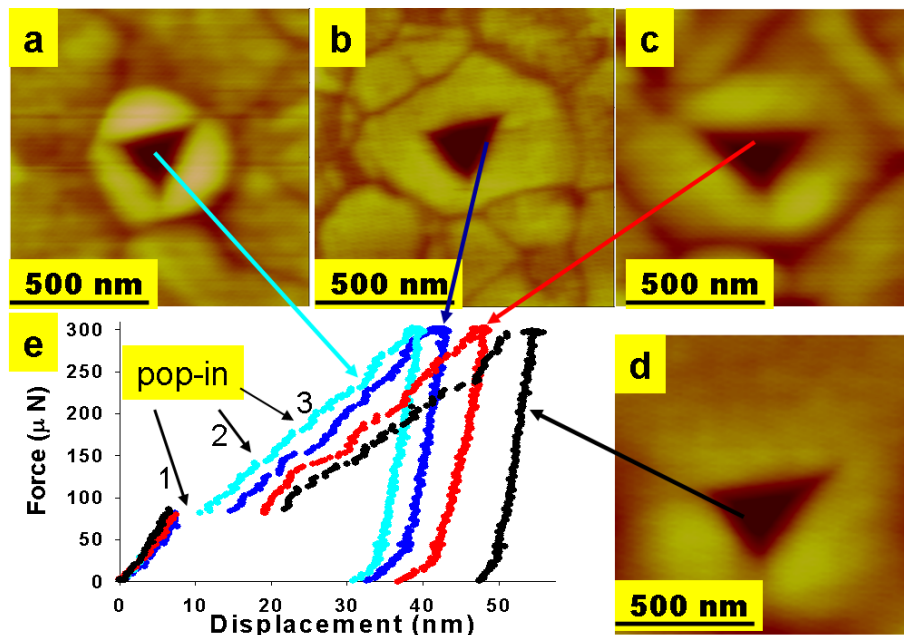


Figure 5.10: Nanoindentation in the center of individual grains with a peak force of  $300 \mu\text{N}$ . All specimens were produced by different heat treatments on NC nickel (No. 87).

### 5.3.1 The first pop-in behaviour vs. individual grain size

Pop-ins refer to the discontinuities in the load-displacement (F-h) curves obtained during nanoindentation, as can be seen in Fig. 5.10e (first pop-in (labelled as 1) and later pop-ins (labelled as 2,3)). Details about the pop-in behaviour have been described in section 2.5.5.2. Three extremely important parameters of pop-in are the pop-in force (the applied load under which the pop-in appears), pop-in displacement (the indent depth at which pop-in appears) and pop-in width ( $\Delta h^*$ , the distance of the discontinuity in the F-h curve). First let us see the first pop-in (as labelled as 1 in Fig. 5.10e) dependence on individual grain size. The pop-in force and pop-in displacement related to the individual grain size are plotted in Fig. 5.11. The maximum

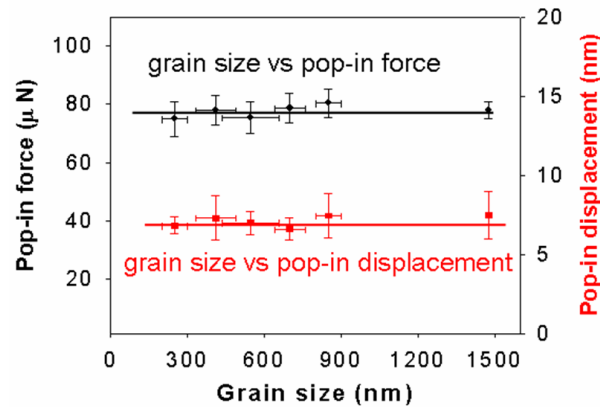


Figure 5.11: The first pop-in force and displacement vs. individual grain size. All specimens were produced by different heat treatments on NC nickel (No. 87).

shear stress  $\tau_{max}$  estimated from Hertzian contact model (equation 2.29 of section 2.5.5.2) and the first pop-in distance related to the individual grain sizes are plotted in Fig. 5.12. It can be seen that for all grains the pop-in force (75–85  $\mu\text{N}$ ), displacement (about 6.5–8.0 nm) and the maximum shear stress (about 8.0–9.1 GPa) are almost the same.

As it has been discussed detailedly in section 2.5.5.2, for a metal with low surface roughness and dislocation density, pop-in always refers to the homogenous dislocation nucleation under the indenter tip, thus corresponding to an initial yield point. As the contact area is very small during nanoindentation, it is reasonable to regard the indented structure as a perfect lattice, and the maximum shear stress ought to be comparable to the theoretical yield strength of materials, normally  $\mu/10$  to  $\mu/2\pi$ . For nickel, taking the shear modulus  $\mu = 78$  GPa, the theoretical strength is 7.8 to 12.4 GPa. The values of the maximum shear stress (8.0–9.1 GPa) estimated are reasonable values and therefore, all the pop-ins in this grain size range can be thought to be the initial yield point of nickel, corresponding to the nucleation of dislocations under the indenter tip.

The first pop-in width  $\Delta h^*$  increases with increasing grain size in the grain size range from 300 nm to 900 nm (Fig. 5.12). The decrease in  $\Delta h^*$  with decreasing grain size could be rationally considered as the fact that the free path of a dislocation is shorter for the smaller grain size due to the barrier effect of the surrounding grain boundaries to the movement of the nucleated dislocations. This is a direct evidence of the local interaction between dislocations and grain

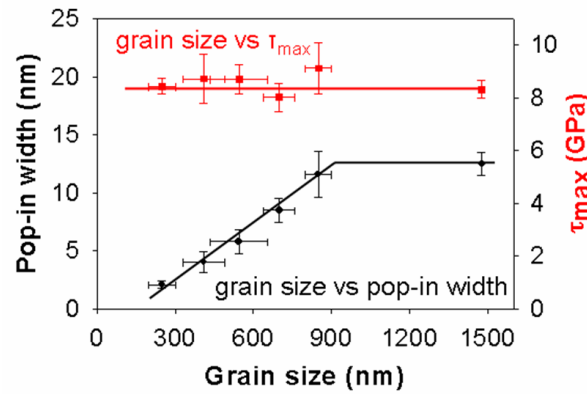


Figure 5.12: The first pop-in width and maximum shear stress ( $\tau_{max}$ ) vs. individual grain size.

The right coordinate refers the maximum shear stress estimated from Hertzian contact model. All specimens were produced by different heat treatments on NC nickel (No. 87).

boundaries. With grain sizes larger than 900 nm, we see the pop-in width  $\Delta h^*$  remains almost constant. This indicates that for individual grains larger than 900 nm, the nucleated dislocations do not interact with the surrounding grain boundaries directly.

An intensive analysis of the grain size dependence of the pop-in width  $\Delta h^*$  can offer us deeper insight into the pile-up theory of the dislocation pile-up model of the H-P effect.

In the dislocation pile-up model, an important assumption is that at the constant effective stress  $\tau_e$ , which drives the dislocation movement and is responsible for the dislocation number  $n$  contained in a pile-up length  $L$  (always taken to be half of the grain size  $d$ ), can be expressed as:

$$L = \frac{d}{2} = \frac{2nA}{\tau_e} \quad (5.18)$$

where  $A$  is a constant depending on the type of the dislocations. This means that the length of the pile-up is to be proportional to the grain size, e.g. pile-up in larger grains may contain more dislocations than that in smaller grains. However, a local examination of this important assumption with individual grains has not been made yet.

During nanoindentation dislocations are nucleated. This corresponds to the occurrence of the first pop-in. Then the nucleated dislocations move across the grain under an effective stress,

and produce a back stress to the effective stress due to the pile-up at grain boundaries. When a balance between the back stress and the effective stress reaches, an increase in the driving stress is needed for additional deformation. A decrease in applied force just after the pop-in was observed in nanoindentation on single crystals with a strain controlled nanoindenter [Kie98], similar to the drop in stress after the sharp yield point usually observed in the tensile tests on metals [Ree91], where the effective stress, which drives the movement of dislocations nucleated, is almost constant. In a nanoindentation test, when the back stress due to the nucleated dislocations is equal to the effective stress, the applied force has to be increased for larger indentation depth (additional deformation). This corresponds to the end of pop-in, resulting in a pop-in width  $\Delta h^*$  observed in the F-h curve. The number of dislocations  $n$  produced during nanoindentation is proportional to the pop-in width, i.e. the more the dislocations nucleated in the pile-up, the larger the pop-in width. Assuming the same constant effective stress during nanoindentation as in a tensile test exists, then the relationship between  $\Delta h^*$  and grain size  $d$  can be used to check equation 5.18.

As shown in Fig. 5.12, a linear relationship between grain size  $d$  and the pop-in width  $\Delta h^*$  was obtained, i.e.

$$d \propto \Delta h^* \quad (5.19)$$

The number of dislocations  $n$  produced during nanoindentation is proportional to the pop-in distance  $\Delta h^*$ , i.e.

$$n \propto \Delta h^* \quad (5.20)$$

A relationship between the grain size  $d$  and the number of dislocations  $n$  contained in the pile-up under the constant stress can be deduced,

$$n \propto d \quad (5.21)$$

It means that more dislocations are nucleated for the larger grains to reach the balance described above. Hence for the first time the equation 5.18 described in the dislocation pile-up model was examined locally in real experiments performed in bulk specimens.

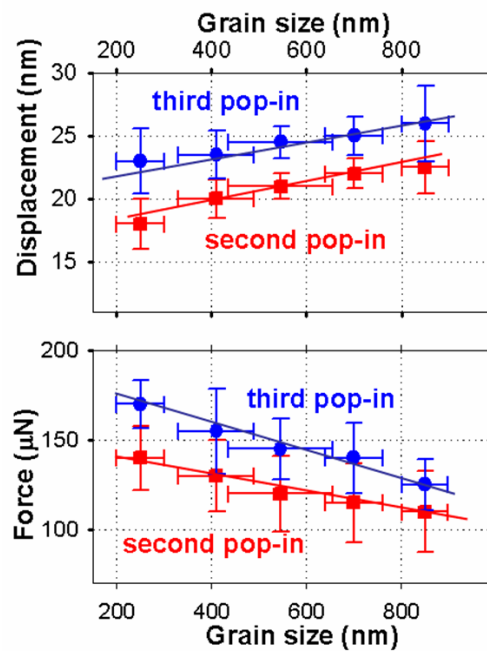


Figure 5.13: Later pop-ins vs. individual grain size. All specimens were produced by different heat treatments on NC nickel (No. 87).

### 5.3.2 The later pop-ins

As can be seen in Fig. 5.10e, beside the first pop-in behaviour discussed above, later pop-ins (labelled as 2 and 3) appear with increasing applied force. The displacements and loads for the later different pop-ins are plotted in Fig. 5.13.

1. The later pop-ins appear frequently for smaller grains (especially for grain size smaller than 800 nm) at smaller indentation depth ranges (smaller than 30 nm);
2. With decreasing grain size later pop-ins appear with increasing loading force and a decreasing displacement (indentation depth). For larger grains, especially that with size larger than  $1.5 \mu\text{m}$ , later pop-ins are rarely detected in this displacement ranges.

Considering the results shown in Fig. 5.8, where for smaller grains hardness begins to decrease at smaller indentation depth after a larger maximum hardness reaches, it is rationally to assume that appearance of the later pop-ins is an evidence for the activation of dislocation sources in the adjacent grains caused by the dislocation pile-up. According to the classical H-P model, the increasing force and decreasing displacement with decreasing grain size for later pop-ins can be

easily understood. As discussed in section 5.3.1, the first pop-in, which appears at the similar load and displacement for all grains, corresponds to the initial yield point of nickel. Later pop-in only appears in the work hardening stage. Since the number of dislocations  $n$  contained in the pile-up length  $L$  increases with increasing grain size (observed as the increasing pop-in width), assuming that the critical stress for the activation of sources in adjacent grains is nearly constant as assumed by Hall and Petch, a higher external stress is needed for smaller grains. The higher pop-in load and lower displacement in smaller grains, as observed in the Fig. 5.13 (beside of scatter due to orientation effects), just verified this theoretical prediction. Furthermore, considering the negligible grain size influences on nanohardness in the larger grains at smaller indentation depth (grain size 1350 nm, indentation depth smaller than 31 nm, Fig. 5.8), we know that for grains with size larger than 1.5  $\mu\text{m}$ , the dislocations produced during nanoindentation are not interacting directly with the grain boundaries at this lower indentation depth ranges. Therefore no later pop-ins would be observed in this smaller indentation depth range.

The experimental results are reproducible, but with deviations if the nanoindenter tip radius changes. However, further experiments are needed to proof this assumption. Efforts has being carried out to increase the resolution of Electron Channelling Contrast Imaging (ECCI) to image the dislocation distribution as a function of the load directly in Field Emission Scanning Electron Microscopy (FESEM).

### 5.3.3 Conclusion

Taking the influences of specimen preparation, indentation position and the ratio of the indent size to the grain size into account, nanoindents were performed always in the centre of individual grains (larger than 200 nm) with a carefully selected load function. Each indent behaves extensive elastic deformation before plastic deformation, corresponding to a discontinuity (pop-in) in the F-h curves. These (first) pop-ins appear almost at the same displacement and the same applied force, and corresponds to a maximum shear stress (estimated from Hertzian contact model) comparable to the theoretical shear stress necessary to nucleate the dislocation. In the grain size range of about 300 nm to 900 nm, direct dislocation-boundary-interaction in bulk specimens was observed:

1. With increasing grain size the first pop-in width increases and nanohardness decreases.
2. The grain size dependence of the pop-in width can be used to examine the pile-up length theory proposed in the dislocation pile-up model of the H-P effect.
3. After the appearance of the first pop-ins, later pop-ins were also observed in the F-h curves with the increasing applied force. Statistic results show that later pop-ins occur at lower loads with increasing pop-in width. This could be regarded as an evidence for the pile-up length effect on the dislocation nucleation in adjacent grains. The results agree well with the theoretical prediction of dislocation pile-up model of the H-P effect.

## **5.4 Grain size effects on the deformation mechanisms revealed from the plastic strain rate-controlled experiments**

As shown in Fig. 4.7 as well as in Fig. 5.2, when the grain size decreases to UFG and NC range, a decrease in the H-P slope values can be observed. This deviation of the H-P behaviour, similar to that observed in other reports [Kna04, Gut01, Mor97, Mas98], was regarded as an indirect evidence of the transition in the deformation mechanisms with decreasing grain size. A better understanding of the different plastic deformation mechanisms in CG, UFG and NC size range can be obtained by evaluating the thermal activated parameters (SRS and AV ) from the strain rate-controlled experiment results.

### **5.4.1 Grain size effects on the tensile deformation mechanisms**

According to the results listed in section 4.4.2.2, strain rate sensitivity (SRS) values of as-prepared commercial CG nickel with a mean grain size larger than 10  $\mu\text{m}$ , heat-treated NC nickel with a mean grain size of about 60 nm and as-deposited NC nickel with a mean grain size smaller than 30 nm are plotted in Fig. 5.14 as a function of plastic strain. SRS increases with decreasing grain size at the same plastic strain.

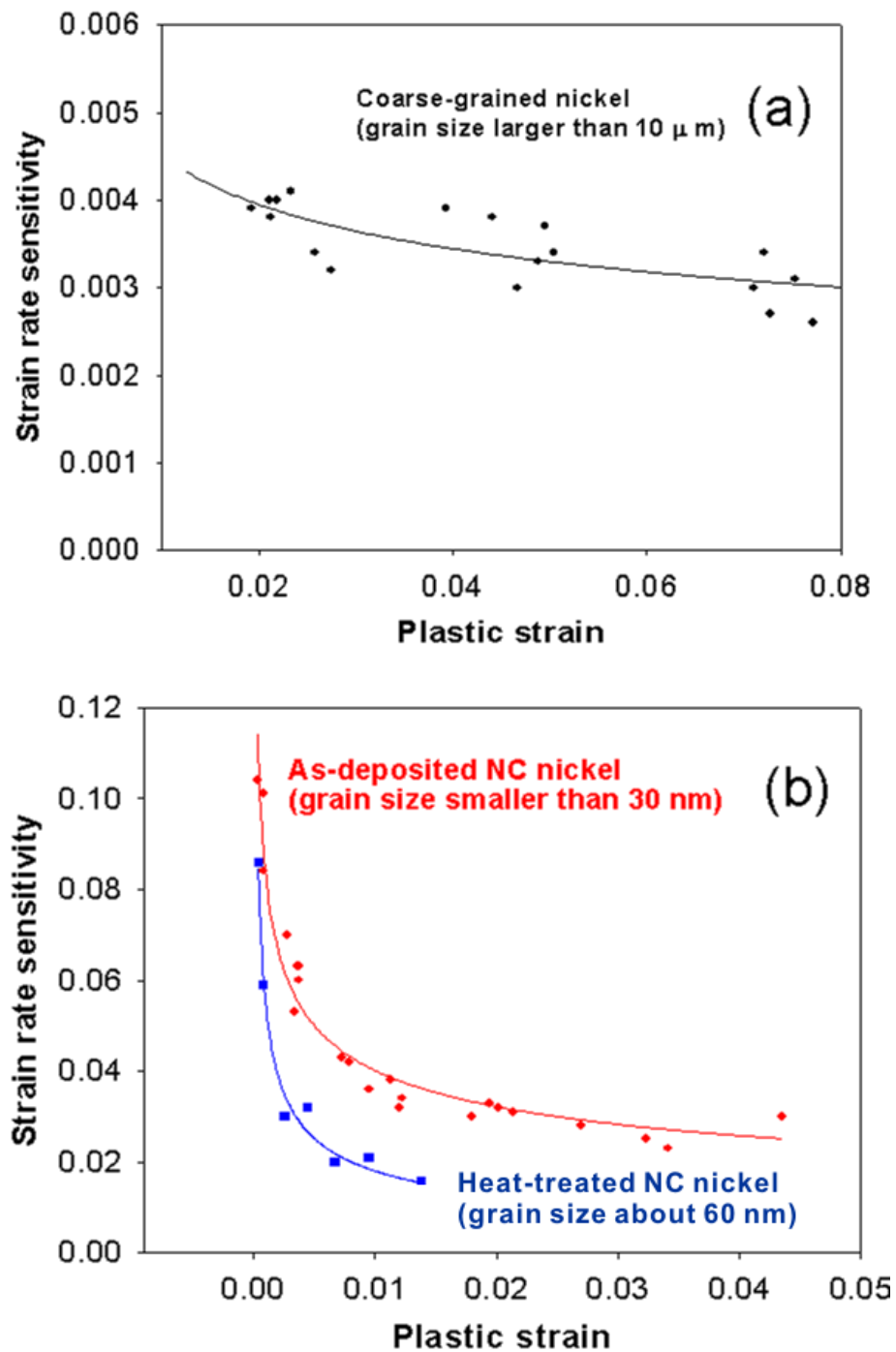


Figure 5.14: Strain rate sensitivity of NC nickel and CG nickel as a function of plastic strain.

(a) CG nickel; (b) as-deposited NC nickel with a mean grain size smaller than 30 nm and heat-treated NC nickel with a mean grain size of about 60 nm; All NC nickel specimens were produced with the same producing procedure; CG nickel specimens were as-prepared commercial nickel with a mean grain size larger than  $10 \mu\text{m}$ .

In the whole plastic strain range CG nickel shows low values of 0.002 to 0.004 (Fig. 5.14a), which are in good agreement with other results in literature [Wei04, May05]. In CG polycrystalline metals, it is known that the plasticity is normally carried by dislocations generated by sources within the grains. Such dislocations propagate and interact with pre-existing structures and also with each other, and can partly annihilate each other. At a given deformation level, all the dislocation segments that have not annihilated make up the final microstructure of the deformed state and are stored as extrinsic grain boundary dislocations, dislocation walls and subgrain boundaries, or individual dislocation segments [Mug91]. This type of deformation always shows a low value of SRS.

The values of the as-deposited NC nickel range from 0.03 to 0.11 in the whole plastic strain range. The heat-treated NC nickel show SRS values from 0.02 to 0.09. The increasing SRS values in NC nickel may correspond to different plastic deformation kinetics from that of CG nickel. These SRS values of NC nickel (especially in the beginning plastic deformation stage) measured from this experiments are a little higher than that reported in recent papers available on the deformation kinetics of UFG and NC metals, where the deformation is described as being thermally activated [Wei04, Dal05, Con03]. Considering the typical SRS value of 0.5 for materials deforming via grain boundary sliding and the low value of 0.004 for CG fcc metals deforming via dislocation slip, the SRS values suggest that the NC nickel deforms with two competitive deformation mechanisms; dislocation activities and grain boundary sliding.

The larger SRS measured in the as-deposited NC nickel demonstrated that grain boundary sliding takes place easier with decreasing grain size. In addition, we see SRS decreases with increasing plastic strain, indicating that grain boundary sliding plays a more important role in the initial plastic stage. With further plastic deformation, deformation through dislocation activities plays a bigger role in this grain size range.

### **5.4.2 Grain size effects on the indentation deformation mechanisms**

As stated in section 4.4.1.2 and 4.4.1.3, the results of nanoindentation with a peak force of 4000  $\mu\text{N}$  and 300  $\mu\text{N}$  show SRS increases with decreasing grain size and is enhanced at lower indent

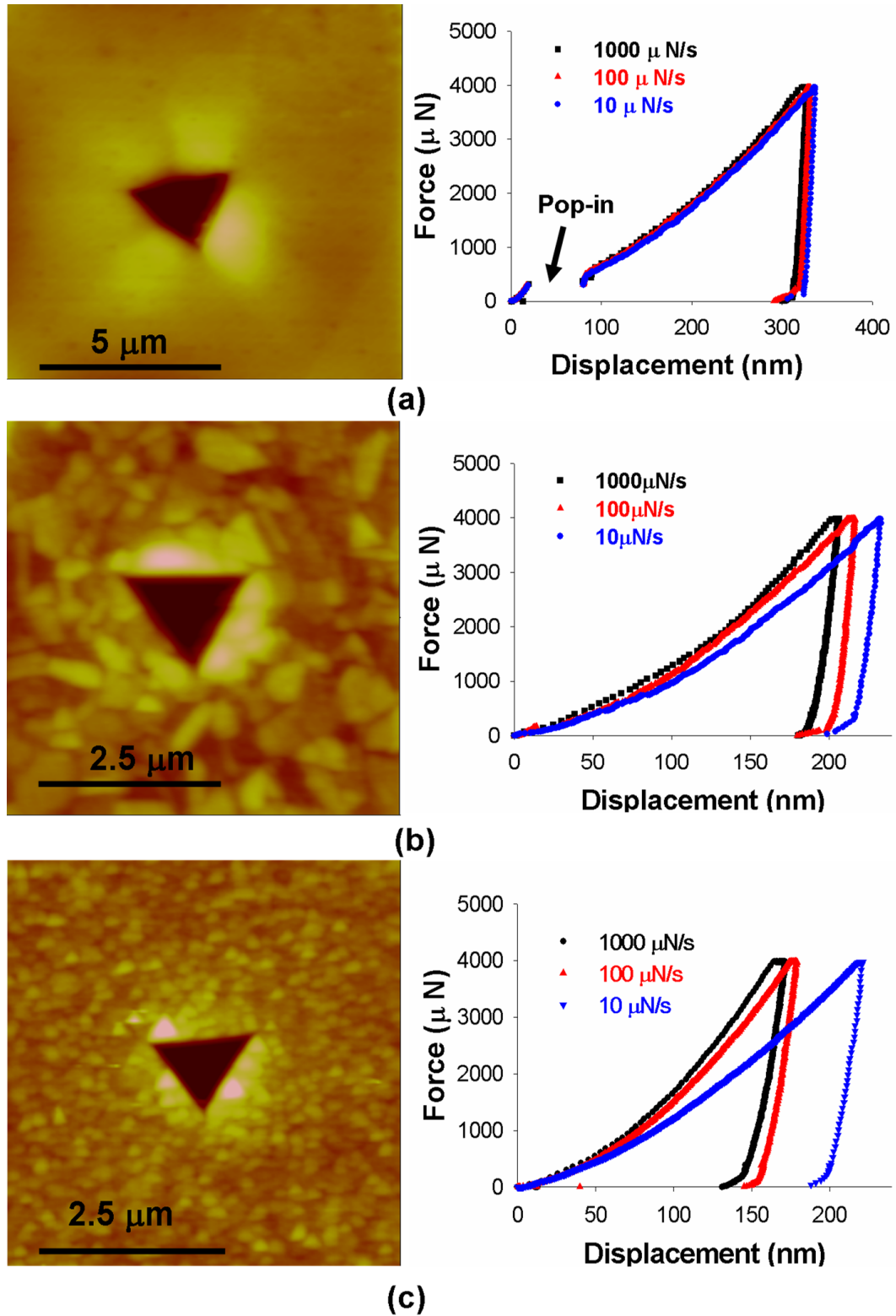


Figure 5.15: Nanoindentation on CG(a), UFG(b) and as-deposited NC nickel(c) with peak force of 4000  $\mu\text{N}$  and different indent rates. All specimens were produced from NC nickel (No. 87).

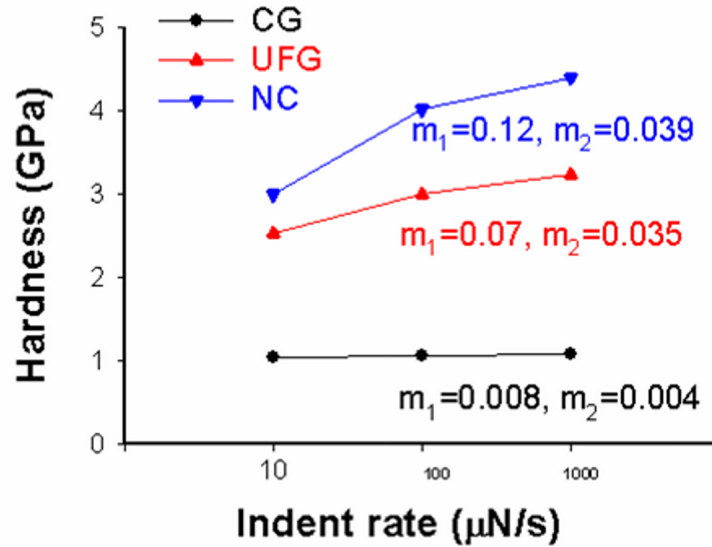


Figure 5.16: Hardness and strain rate sensitivity of CG, UFG and as-deposited NC nickel.  $m_1$  is calculated from the data with indent rate 10  $\mu\text{N/s}$  and 100  $\mu\text{N/s}$ , while  $m_2$  from 10  $\mu\text{N/s}$  and 1000  $\mu\text{N/s}$ . All specimens were produced from NC nickel (No. 87).

rate range.

F-h curves of nanoindentation with a peak force of 4000  $\mu\text{N}$  were plotted in Fig. 5.15a for CG nickel, Fig. 5.15b for UFG nickel and Fig. 5.15c for as-deposited NC nickel respectively, combined with a post-indentation image in-situ captured by NI-AFM on the left. According to the results listed in table 4.2, nanohardness of CG, UFG and as-deposited NC nickel (No. 87) related to indent rates were plotted in Fig. 5.16. The values of strain rate sensitivity  $m$  calculated were also added on the same diagram.

We can see that for CG nickel, the nanohardness increases slightly with the increasing indent rate, resulting in very low strain rate sensitivity (SRS) ( $m_1 = 0.008$  in the lower indent rate range and  $m_2 = 0.004$  in the higher indent rate range). For CG nickel (Fig. 5.15a), the indent rate has little influence on the indentation behaviour, the three curves lap over almost each other till the very last stage. The SRS of CG nickel resulted from the experiments, though not deduced from the normal strain jumping test, are consistent with results of the tensile strain jump experiments on CG nickel. Identical pop-in behaviour, which corresponds with the transition from elastic to plastic deformation, appears in the initial part of the F-h curves (Fig. 5.15a), indicating dislocation nucleation and motion in the grain.

The SRS increases with decreasing grain size, especially in the lower indent rate range. This is also consistent with the tensile strain jump experiments.

For the UFG nickel, the SRS in the lower indent range  $m_1$  is 0.07, about 10 orders of the CG nickel; even in the higher indent rate range a value  $m_2 = 0.035$  is calculated. From Fig. 5.15b, a distinct and experimentally detectable effect of indent rate for UFG nickel can be seen, for higher indent rates higher indent forces are always required in order to produce the same displacement. The SRS value of UFG nickel measured in nanoindentation tests ( $m_1 = 0.07$ ,  $m_2 = 0.035$ ) indicate that grain boundary sliding takes place during indentation. This may be due to the movement of grain boundaries caused by the indenter tip, because the indent size is large and many grains are indented, as can be seen in the post-indentation image Fig. 5.15b in-situ captured by NI-AFM. However, even in the local nanoindentation examination in UFG size range, grain boundary sliding was also confirmed.

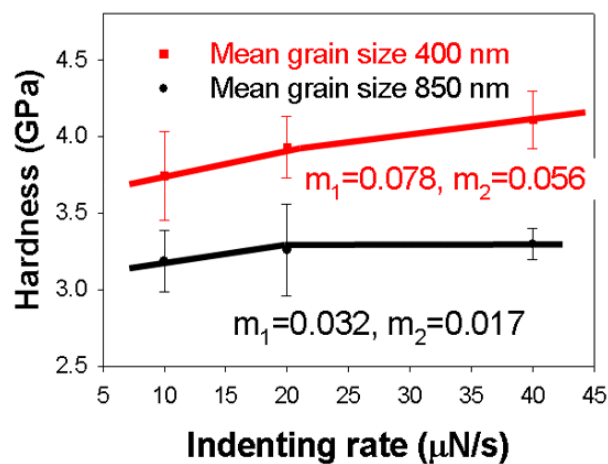


Figure 5.17: Hardness and strain rate sensitivity of grains with sizes of 850 nm and 400 nm.  $m_1$  is calculated from the data with indent rate of 10  $\mu\text{N/s}$  and 20  $\mu\text{N/s}$ , while  $m_2$  from indent rates of 20  $\mu\text{N/s}$  and 40  $\mu\text{N/s}$ .

According to the results listed in table 4.3, nanohardness related to indent rates were plotted in Fig. 5.17. The values of calculated strain rate sensitivity  $m$  were also added on the same diagram. F-h curves of nanoindentation are plotted in Fig. 5.18a for larger grains (grain size about 850 nm, all from as-deposited NC nickel after a heat-treatment at 300°C for 2h) and Fig. 5.18b for smaller grains (grain size of about 400 nm, all from as-deposited NC nickel after

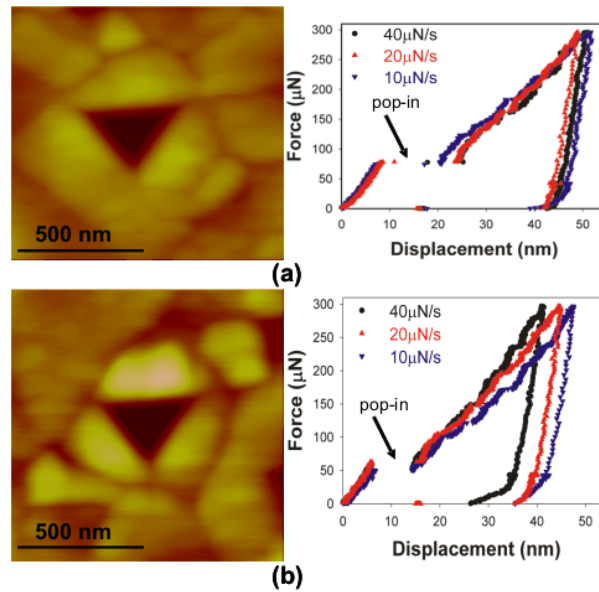


Figure 5.18: Local examination of indent rate effects in UFG grains (the sizes of individual grains are about 850 nm for (a) and 400 nm for (b)) with peak force of 300  $\mu\text{N}$ . All specimens were produced from NC nickel (No. 87).

heat-treatment at 250°C for 2h) respectively. A post-indentation image captured by NI-AFM is on the left and the F-h curves are on the right. That the indent size is smaller than the indented grain can be seen. Both UFG grains show enhanced indent rate effects compared the CG nickel, and the SRS increases with decreasing grain size and is pronounced in the lower indent range (Fig. 5.17). Pop-in appears always in the F-h curves, and higher hardness are observed in the smaller grains (Fig. 5.17). This indicates that in this grain size range grain boundary sliding takes place during indentation, but dislocation activity is the dominant deformation mechanism.

The increase in SRS is more pronounced for as-deposited NC nickel with values  $m_1 = 0.12$  in the lower indent range and  $m_2 = 0.039$  in the higher indent rate range (Fig. 5.16). The SRS of as-deposited NC nickel in the lower indent range (0.12) is about 15 times of the SRS of CG nickel (0.008) examined at the same conditions. The post-indentation image (Fig. 5.15c) in-situ captured by NI-AFM shows clear evidence of grain boundary sliding around the indenter.

The significant increase in the SRS in UFG and NC fcc metals compared with that in the CG counterparts is not completely understood up to now. In our local nanoindentation experiments, we only indent in the center of the large grains (larger than 80  $\mu\text{m}$ ) for CG nickel, so it can

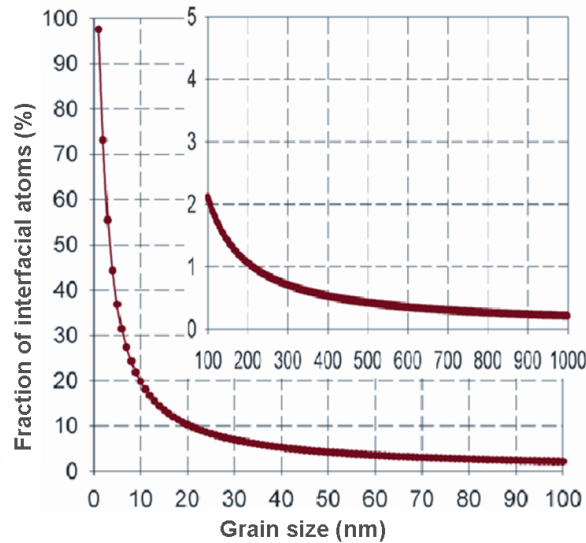


Figure 5.19: Fraction of interfacial atoms of a grain related to the grain size. The part of grain size range from 100 nm to 1000 nm is overlapped.

be considered that the effects of grain boundaries are negligible. If the grain boundary volume tested by the nanoindenter increases with the decreasing grain size, the significant increase of SRS must closely be related to the grain boundary-mediated deformation. This is reasonable, because the interface volume increases with refinement of grain size. Taking a simple spherical shape of grains, the volume fraction of interfacial atoms (assuming one atom in thickness) of a grain related to the grain size are plotted in Fig. 5.19. There would be 10% atoms occupying the interface for a 20 nm grain. The increase in the interface volume with refinement of the grain size is more pronounced as the grain size is smaller than 20 nm. Furthermore, in the particular test of nanoindentation, the plastic deformation zone is much more concentrated, which assuredly enhances the grain boundary-mediated deformation.

An example was shown in Fig. 5.20. From the post-indentation images captured in-situ by AFM, grain boundary sliding during nanoindentation can be directly observed at the surface. The surface of as-deposited NC nickel (No. 62) before (Fig. 5.20a) and after indentation (Fig. 5.20b) was analysed. Only two grains (labelled as 1 and 2) far from the indent were marked as an example. The AFM line section results in Fig. 5.20(c,d) show no obvious shape change of the two grains after indentation, but the height of the grains in relation to each other changes greatly. Farther from the indenter, no height changes were detected. Consider the AFM with

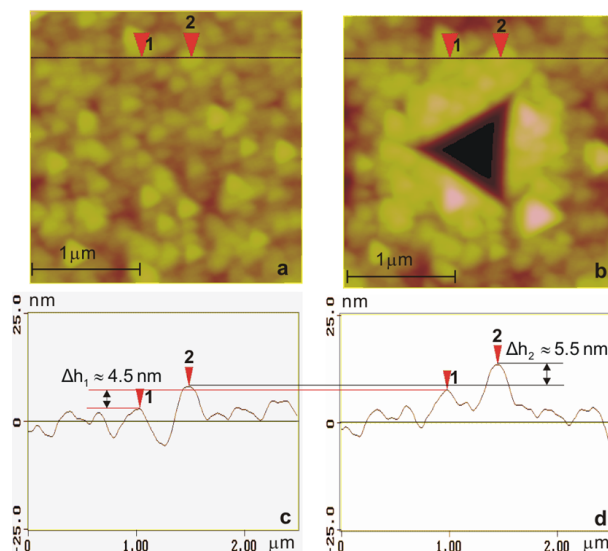


Figure 5.20: The same surface area before and after indentation. Grain boundary sliding around the indenter can be seen. Nanoindentation was performed on as-deposited NC nickel (No. 62) with a peak force of  $2000 \mu\text{N}$ .

a height resolution better than 2 nm, it is reasonable to conclude that grain boundary sliding around the indenter happens in this type of particular test.

### 5.4.3 Plastic deformation kinetics revealed by analysis of activation volume

The SRS values released from the tensile strain rate jump experiments show that NC nickel deforms with grain boundary sliding and dislocation activities. However, the dislocation source is not clear. To find out whether the dislocations are emitted from grain boundary (grain boundary dislocation) or from the inner of the grain (like Frank-Read source), let us see the activation volume (AV) in NC (as-deposited and annealed) and CG nickel resulted from the tensile strain rate jump experiments.

Effective AV as a function of plastic strain is plotted in Fig. 5.21. Opposite to the SRS dependence on the grain size, the AV decreases with decreasing grain size and increases with increasing strain. The obtained activation volume of CG nickel is in the range of  $1000\text{--}1500 b^3$  while for the as-deposited NC nickel it is only  $8\text{--}20 b^3$ ; as the grain size increases a little bit,

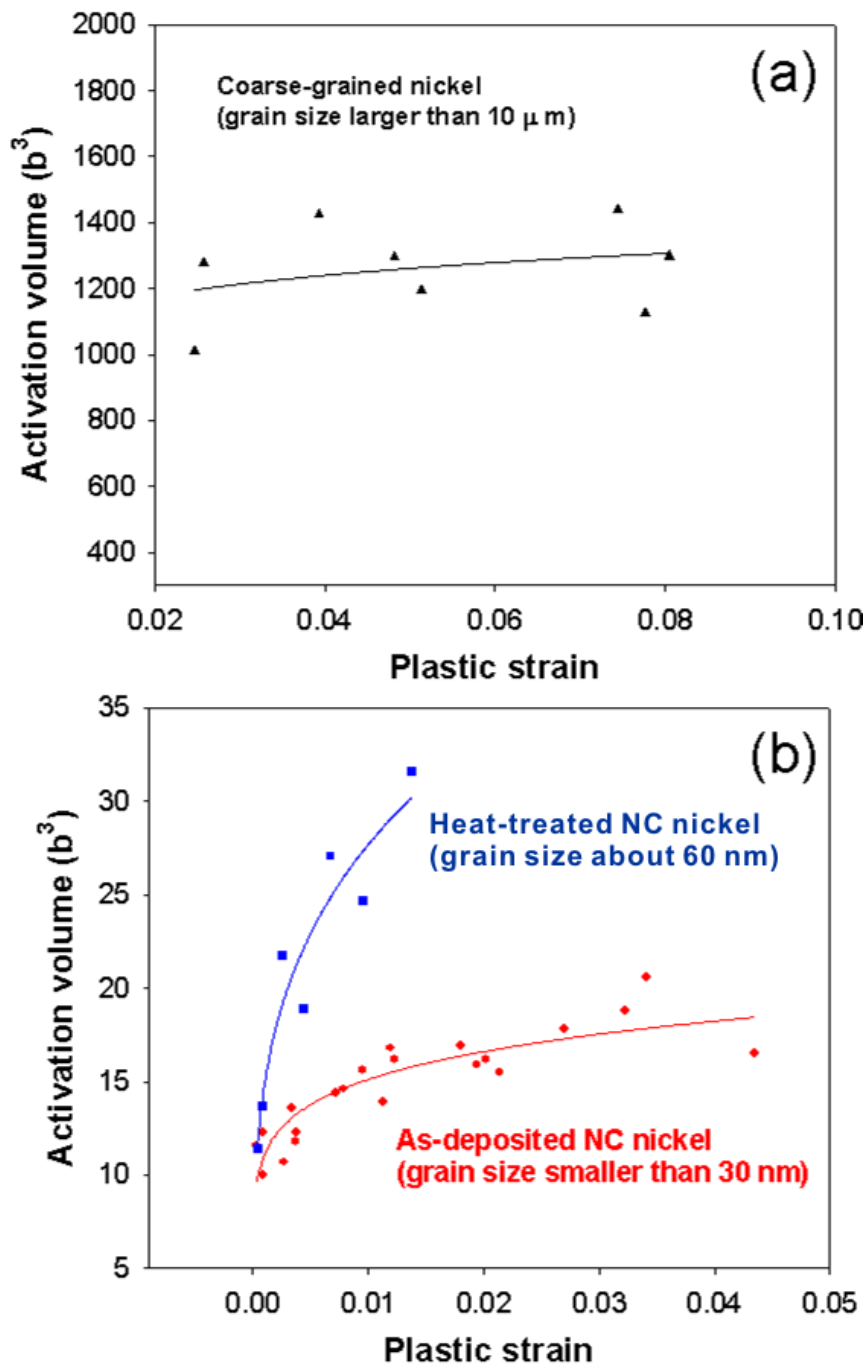


Figure 5.21: Activation volume of NC nickel and CG nickel as a function of plastic strain. (a) CG nickel; (b) as-deposited NC nickel with a mean grain size smaller than 30 nm and heat-treated NC nickel with a mean grain size of about 60 nm; All NC nickel specimens were produced with the same producing procedure; CG nickel are as-prepared commercial nickel with mean grain size larger than  $10 \mu\text{m}$ .

the AV value increases to  $10\text{--}32 b^3$ , still much smaller than that of the CG nickel.

According to the work of Becker [Cah01, Koc01], the AV  $V_a$  can be written as:

$$V_a = l \cdot \xi \cdot b \quad (5.22)$$

where  $l$  is the obstacle distance,  $\xi$  the obstacle width and  $b$  the Burger's vector. Taking the obstacle width  $\xi$  with the same value of Burger's vector, the obstacle distance  $l$  can be estimated by:

$$l = \frac{V_a}{b^2} \quad (5.23)$$

For CG nickel, with the shear modulus  $\mu = 78$  GPa and  $b = 2.5 \cdot 10^{-10}$  m, the stress needed to bow out a dislocation can be estimated from:

$$\sigma_{min} = \frac{\mu}{bl} = \frac{\mu b}{V_a} \quad (5.24)$$

which is 52–78 MPa. The value is much smaller than the tensile strength observed (about 300 MPa). Therefore, the plasticity in CG nickel is mainly carried by dislocations generated by sources (very likely the Frank-Read dislocation source) within grains.

Using the same procedure described above, the minimum stress needed to activate a Frank-Read source is 3900 MPa for as-deposited NC nickel and 2230 MPa for heat treated NC nickel (about 60 nm grain size), much higher than the real value measured in the experiments (maximum 1800 MPa). Therefore, in NC nickel the operating dislocation mechanism is definitely different from that in the CG nickel. Considering the results revealed by MD simulations and TEM observations [Van02, Yam02, Lia04], it is directly confirmed that grain boundaries are the sources of the dislocation (perfect or partial) emission.

#### 5.4.4 Conclusion

1. Tensile strain rate jump experiments revealed that in the whole plastic strain range CG nickel show low SRS values about 0.002–0.004, which are typical values for CG fcc metals deforming by dislocation slip; the SRS values increase to 0.03–0.11 for as deposited NC nickel with mean grain size smaller than 30 nm and 0.03–0.09 for heat-treated NC nickel with grain size of about 60 nm. The highest SRS value was observed at the beginning plastic deformation stage. The SRS value of NC nickel lies between that of materials

deforming via grain boundary sliding and dislocation slip, indicating both mechanisms operating during deformation. Thus, with grain size decreasing from conventional CG size range to nanograin size range, the intergranular deformation process competes with the traditional dislocation mechanism and plays an increasing role, especially at the initial plastic deformation stage.

2. The grain size effects on the SRS resulted from nanoindentation tests are consistent with that of tensile strain rate jump tests. For CG nickel the indent rate has little influence, resulting in a low value of SRS. Identical pop-in behaviour was observed in the F-h curves, indicating dislocation nucleation and motion in the grain. The SRS increases as the grain sizes decreases down to UFG and NC scale, especially in the lower indent rate range. For as-deposited NC nickel, post-indentation AFM images show clear evidence of grain boundary sliding around the indenter.
3. CG nickel show much higher AV values ( $1000\text{--}1500 b^3$ ) than that of NC nickel ( $8\text{--}32 b^3$ ). Analyses of the AV values confirmed that the plasticity in CG nickel is carried by dislocations generated from Frank-Read-like sources within grains; in NC nickel, however, the dislocations are nucleated from grain boundaries.

## **5.5 Grain size effects on the room temperature creep behaviour and the creep mechanisms of nanocrystalline nickel according to Norton's creep law**

From the room temperature tensile stress jumping experiments, creep behaviour was observed only in NC (as-deposited and heat treated) nickel. It is known that two parameters, i.e. grain size and diffusivity, involved in dictating the creep rate of a polycrystalline material. By increasing diffusivity and/or reducing the grain size, the creep rate of a polycrystalline material can be enhanced. With respect to the diffusivity, experimental work [Hor87] has shown that for the NC Cu it is  $10^3$  times higher than that in conventional CG Cu. Therefore, the results for CG

nickel (creep behaviour not observed at this room temperature test) are normal.

We use the Norton's creep law [Nor29] to reveal the creep mechanisms of NC nickel. The Norton's creep law can be described as:

$$\dot{\epsilon}_s = k_3 \cdot \sigma^n \quad (5.25)$$

In this equation  $\dot{\epsilon}_s$  is the steady-state creep rate,  $k_3$  a constant,  $\sigma$  the applied stress and  $n$  the coefficient. According to this law it follows:

- $n = 1$ , Coble or Nabarro-Herring creep
- $n = 2$ , grain boundary sliding
- $n \geq 3$ , dislocation creep

According to the Fig. 4.17, the stress related to the creep rate of NC nickel is plotted with a log-log form in Fig. 5.22. The fitted coefficients  $n$  according to the Norton's creep law are added on the same diagram.

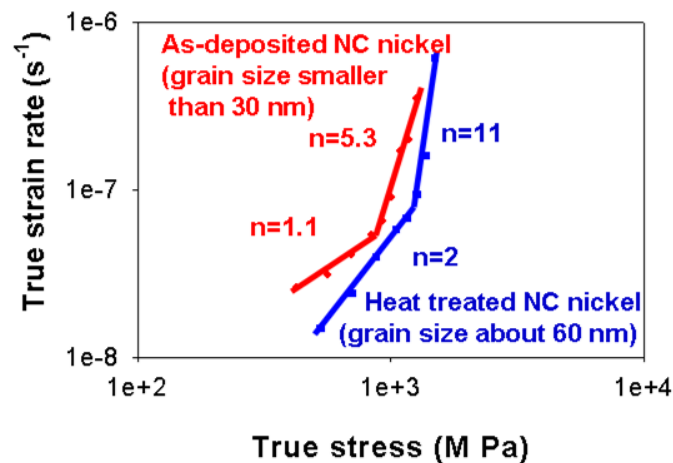


Figure 5.22: Creep rate as a function of stress plotted with log-log form. As-deposited NC nickel with a mean grain size smaller than 30 nm and heat-treated NC nickel with a mean grain size of about 60 nm; All NC nickel were produced with the same producing procedure.

For as-deposited NC nickel with mean grain size smaller than 30 nm, we have:

1.  $\sigma < 1$  GPa and  $\dot{\epsilon}_s < 6 \times 10^{-8} s^{-1}$ ,  $n = 1.1$ , the deformation mechanism is controlled by grain boundary sliding together with diffusion along the interface;
2.  $\sigma > 1$  GPa and  $6 \times 10^{-8} s^{-1} < \dot{\epsilon}_s < 3.5 \times 10^{-7} s^{-1}$ ,  $n = 5.3$ , in this condition the deformation is mainly controlled by dislocation creep.

For heat-treated NC nickel with mean grain size about 60 nm, we have:

1.  $\sigma < 1$  GPa and  $\dot{\epsilon}_s < 6.5 \times 10^{-8} s^{-1}$ ,  $n = 2.03$ , the deformation mechanism is controlled mainly by grain boundary sliding;
2.  $\sigma > 1$  GPa and  $6 \times 10^{-8} s^{-1} < \dot{\epsilon}_s < 3.5 \times 10^{-7} s^{-1}$ ,  $n = 11$ , in this condition the deformation is mainly controlled by dislocation creep.

For as-deposited NC nickel, the slope value of 1.1 lies between that of grain boundary sliding and Coble creep; comparing the results of 2 for heat-treated NC nickel with larger grain sizes, it confirms that grain size has a great influence on the creep behaviour: diffusion along the interface is preferred for small grains.

From the results we see, as the creep rate is larger than  $3.5 \times 10^{-7} s^{-1}$  for the as-deposited nickel with grain size smaller than 30 nm and larger than  $1.7 \times 10^{-7} s^{-1}$  for the heat-treated NC nickel with mean grain size of 60 nm, dislocation creep mechanism begins to play a dominant role in the beginning plastic deformation stage. It explains the higher value of SRS (Fig. 5.14) and lower value of AV (Fig. 5.21) as the plastic strain  $\epsilon_p < 0.005$  in the tensile strain rate jump experiments. For strain larger than 0.005 the creep process could exist but it is not important: the dislocation-controlled mechanism dominates the deformation process.

At high stress levels, dislocation creep becomes the predominant deformation mechanism for both of the two NC nickel, indicating a deformation mechanism transition from an intergranular process to an intragranular process.

## 5.6 Deformation behaviour of bulk nanonickel studied by in-situ bending AFM

### 5.6.1 Bending behaviour

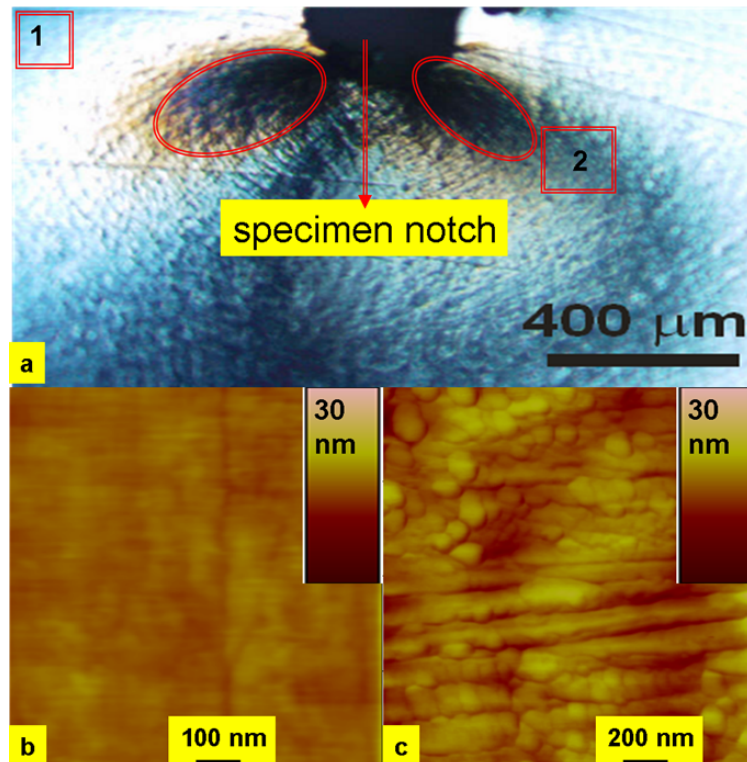


Figure 5.23: Bending response of NC nickel. (a) Optical microscopy surface topography after bending. The largest plastic deformation took place at two areas near the specimen notch (marked by the ellipse). (b) AFM image of the surface area without plastic deformation (frame 1 in Fig. 5.23a). (c) AFM image of the surface area with large plastic deformation (frame 2 in Fig. 5.23a). Nanograins moved up in order to accommodate to the large plastic strain.

The bending behaviour of as-deposited NC nickel (No. 62) was examined. The specimen was loaded by the in-situ bending machine to a large plastic strain. Optical microscopy surface topography after bending is shown in Fig. 5.23a. Different areas of the specimen surface were captured by AFM. The area without plastic deformation (labeled as 1 in Fig. 5.23a) has a smooth surface, as shown in Fig. 5.23b. The area with large plastic deformation (labeled as 2

in Fig. 5.23a) is shown in Fig. 5.23c. The AFM images show that the nanograins moved up obviously in order to accommodate to the large plastic strain, indicating grain boundary sliding taking place during bending.

### 5.6.2 Fatigue response and fracture behaviour

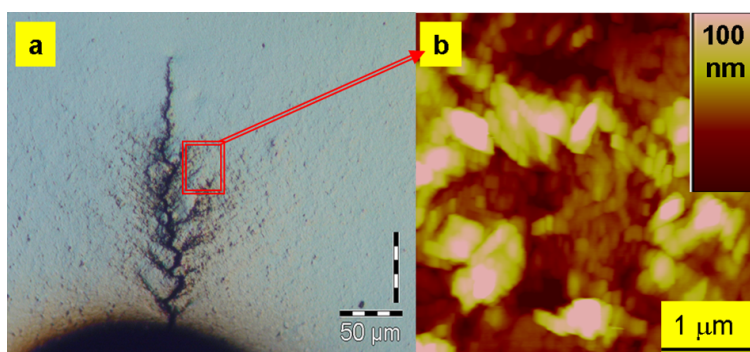


Figure 5.24: Surface topography of as-deposited NC nickel after fatigue. (a) Optical microscopy image and (b) AFM image near the main crack; the height scale can be seen on the upper right-hand side.

The surface of as-deposited NC nickel after fatigue is shown in Fig. 5.24. Optical microscopy (Fig. 5.24a) reveals a tree-like crack propagating type after fatigue. Fig. 5.24b is an AFM image captured near the main crack, where a bumpy surface topography can be seen. The position of the nanograins related to each other changes a lot: some grains moved up and some grains moved down. This is a clear evidence of grain boundary sliding. The severe deformation near the crack results in a higher roughness, as measured by AFM. AFM roughness measurements show a roughness value of 24 nm for Fig. 5.24b, which is much higher than the value (4 nm) before fatigue.

The crack tip after fatigue imaged by in-situ AFM is shown in Fig. 5.25a. With increasing load, the crack becomes wider and the deformation extent around the tip increases, as shown in the sequent images of Fig. 5.25b and c. It seems that the crack propagates along the grain boundaries. However, a definite crack propagating path was not acquired in this case, because the crack does not grow further with increasing load; furthermore, because the plastic deformation near the crack tip is quite large, it is very difficult to distinguish the single grains.

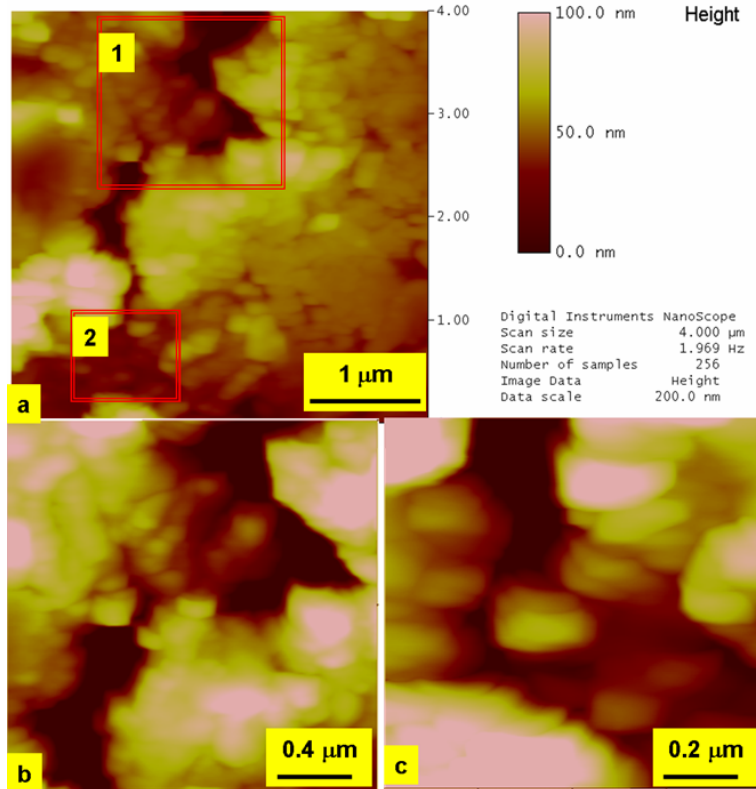


Figure 5.25: AFM images of as-deposited NC nickel after fatigue. (a) The end of the crack tip after fatigue. (b) The area (labeled as 1 in (a)) in-situ imaged after increasing the load. (c) The area (labeled as 2 in (a)) in-situ imaged after increasing the load.

To image the crack path in the quite ductile NC nickel, the critical factor is to make the crack as sharp as possible. At the same time, the deformation near the crack tip must be kept as small as possible. Only in this case, the fracture pattern of the bulk specimen can be imaged by AFM in a relative flat plane. A better result was achieved by just pulling the specimen (with a pre-crack induced by fatigue) to a plastic strain of  $6 \times 10^{-3}$ . Fig. 5.26a shows the very end of the crack tip after this treatment. By increasing the load step by step with the help of the in-situ bending machine, the crack tip became wider. The crack propagation pattern is shown in the sequent images of Fig. 5.26b-d. It can be seen that the crack propagation of as-deposited NC nickel is intergranular. No sub-cracks are observed. It is worth noting that the grain, as marked by the arrow in Fig. 5.26a and b, cannot be definitely detected any more in Fig. 5.26c, as the crack opened much wider. Images show higher height of grains along the crack, indicating that the crack propagation associates with grain boundary sliding.

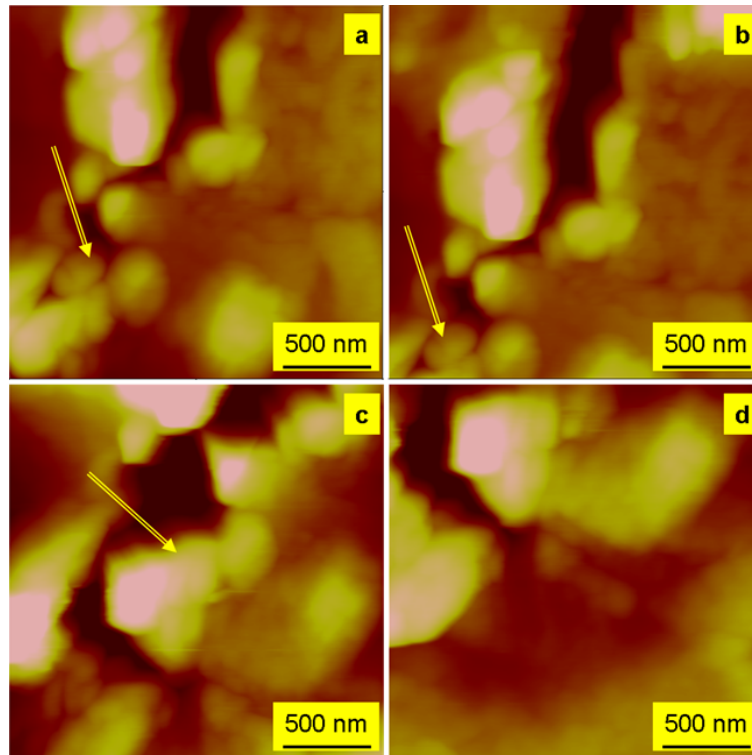


Figure 5.26: Crack tip of as-deposited nanocrystalline nickel revealed by in-situ bending AFM. (a) The crack tip after fatigue; (b-d) successive images of the crack tip with increasing load.

A similar observation has been reported recently by Shan and Mao [Sha05]. They studied the deformation process of as-deposited NC nickel (with a mean grain size of about 10 nm) in response to the tensile displacement pulse with in-situ TEM technique. Their dark-field TEM images showed that large bright features form at first during deformation; with further loading, crack nucleates among the newly formed bright features. Because these bright features are much larger than the average grain size and do not result from nanograin growth, they concluded that a strong grain boundary-related activity, such as grain boundary sliding and grain rotation, occurred for as-deposited NC nickel.

## **5.7 The local dislocation-boundary-interaction and the deformation mechanisms of bulk nanocrystalline nickel**

In this chapter, the results are intensively discussed in six parts according to the aims of this work.

The local interaction between dislocations and grain boundaries in single grains examined by nanoindentation are discussed in the first three parts: (1) Nanohardness dependence on the ratio of indent size and grain size. Nanohardness may remain constant, increase and decrease with decreasing grain size, depending on the relationship between the indent (plastic zone) size and the indented grain size, which is further quantitatively defined in (2) Indentation size effect in individual grains. Different indentation depth dependences of nanohardness were observed, which reflect directly the local interaction between dislocations and grain boundaries in single grains, and further discussed from the grain size effects on the pop-in behaviour described in (3) Direct observation of dislocation-boundary-interaction in ultrafine grains.

The deformation mechanisms of electrodeposited nanonickel at room temperatures are discussed in the next three parts: (1) Grain size effects on the thermal activated parameters revealed from the plastic strain rate-controlled experiments: strain rate jump experiments in tensile tests and nanoindentation experiments by using different loading rates. The SRS increases as the grain sizes decrease down to UFG and NC scale, indicating that the grain boundary mediated deformation process competes with the traditional dislocation (slip) mechanism and plays an increasing role, especially at the initial plastic deformation stage. Quantitative analyses of the AV show that in NC nickel the conventional Frank-Read dislocation source cease to operate and grain boundaries act as dislocation sources; (2) Room temperature creep behaviour. Room temperature creep is observed only in NC nickel. Results show that in NC nickel grain boundary sliding or diffusion along interface seem to dominate at lower stress levels, but with increasing stresses the deformation process is mainly controlled by dislocation creep; (3) The bending behaviour, fatigue response and fracture of bulk NC nickel revealed by the in-situ bending AFM. For the first time, grain boundary sliding at room temperature is observed playing an important

role in bulk NC nickel during bending and fatigue tests. The fatigue crack of bulk NC nickel is revealed to be intergranular, which is different from the well-known intragranular fracture behaviour in coarse-grained metals. These results demonstrated a transition in the dominating deformation mechanism with grain size decreasing from conventional CG size range to nanograin size range, which is responsible for the deviation of H-P behaviour observed in NC materials.

## 6 Summary

The microstructure is crucial to a wide variety of the properties of any engineering material. For this reason, the study of structure-property relationship has been historically of greatest interest in materials science. A subject of continuous investigation is the grain size effects on the mechanical properties of materials.

An increase in yield strength with decreasing grain size is characteristic for most of the metals and alloys, and has become known as the H-P effect. Although the validity of H-P relationship has been confirmed in many systems of materials from millimeter-sized grains down to the submicron regime, the physical basis of this behaviour remains imperfectly understood.

The availability of NC materials in recent years provides a unique opportunity to investigate the grain size effects on the mechanical properties at an extremely fine microstructural scale, igniting a renewed interest in this field. A new phenomenon is the deviation of H-P behaviour observed only in the nanograin size range. This deviation is thought to be due to a change in the deformation mechanisms, about which a universal agreement is not made yet.

The above considerations motivated the preceding chapters described in this thesis: to study the two important aspects related to grain size: the physical basis of H-P behavior and the deformation mechanisms in nanocrystals.

In Chapter 2, a literature review of the current research status is offered. Beginning with a brief review of the synthesis, common characteristics, mechanical properties of NC materials and the general introduction of plastic deformation, the two most accepted models of the H-P behaviour, the specific deformation mechanisms in NC materials and the present study methods are presented. At the end of this chapter the reasons for the scarcity of a full understanding to the origin of H-P relationship and the deformation mechanism in the nanograin size range are analysed, and the aims of the study are defined further: (1) Probing the interaction between dis-

locations and grain boundaries in single grains directly by performing nanoindentations in the center of individual grains with the help of a NI-AFM; (2) Unravelling the deformation mechanisms of electrodeposited nanonickel at room temperatures.

In Chapter 3 the experimental details were described, including the specimen preparation, the microstructure analysis and the related mechanical property measurements: microindentation, nanoindentation, tensile and bending, etc. Two important techniques, NI-AFM and in-situ bending AFM, which play a key role in the investigations, are described in detail.

According to the aims of this study, the results given in Chapter 4 were discussed and concluded in six parts in Chapter 5.

*The local interaction between dislocations and grain boundaries in single grains* were discussed detailedly in the first three parts:

1. Nanohardness dependence on the ratio of indent size and grain size. In this part, for the first time, it is pointed out that nanohardness depends not only on the grain size, but also on the ratio of the indent size to the grain size. For hardness measurements with a nanoindenter, different ranges of grain size related to the indent size must be taken into account. Nanohardness may remain constant, increase and decrease with decreasing grain size, depending on the relationship between the indent (plastic zone) size and the indented grain size.
2. Indentation size effect in individual grains. In this part, the influence of lateral boundary conditions on the indentation size effect was for the first time studied. Different indentation depth dependences of nanohardness were observed, which reflect directly the local interaction between dislocations and grain boundaries in single grains. (1) When the dislocations nucleated below the indenter do not interact directly with the surrounding interfaces, hardness decreases with increasing indentation depth; (2) When the grain boundaries act as barriers for the movement of dislocations and the plastic zone is confined in the indented grains, hardness increases with increasing indentation depth. At a constant indentation depth, a smaller grain will exhibit a higher hardness due to a higher dislocation density. That the radius of the plastic zone is about 3.5 times of the contact radius was deduced in this work; (3) With further increasing indentation depth, a decrease

in hardness is found, resulting in a maximum hardness. This is due to the spreading of the plastic zone out of the indented single grains at a critical indentation depth, a direct evidence of the activation of new dislocation sources in the neighbouring grains caused by the pile-up of dislocations. Smaller grains show a higher maximum hardness value compared with the larger grains, meaning that for a larger grain a smaller external applied load is needed to activate the new dislocation sources in neighbouring grains. This agrees with the well-known dislocation pile-up model of the H-P behaviour.

3. Direct observation of dislocation-boundary-interaction in ultrafine grains. In this part, the direct dislocation-boundary-interaction in single grains is described from the grain size effects on the pop-in behaviour. With increasing grain size in the range of about 300 nm to 900 nm, the first pop-in width increases and later pop-ins were observed with the increasing applied force. The observed behaviour can be used to examine the pile-up length theory proposed in the dislocation pile-up model of the H-P effect.

*The deformation mechanisms of bulk electrodeposited nanonickel* are revealed in the following three parts:

1. Grain size effects on the thermal activated parameters revealed from the plastic strain rate-controlled experiments. (1) Tensile strain rate jump experiments revealed that in the whole plastic strain range CG nickel show low SRS values of about 0.002–0.004, which are typical values for CG fcc metals deforming by dislocation slip; the SRS values increase to 0.03–0.11 for as-deposited NC nickel with mean grain size smaller than 30 nm and 0.03–0.09 for heat-treated NC nickel with mean grain size of about 60 nm. The highest SRS value was observed at the beginning plastic deformation stage. The SRS value of NC nickel lies between that of materials deforming via grain boundary sliding and dislocation slip, indicating the operating of the both mechanisms during deformation; (2) The grain size effects on the SRS resulted from nanoindentation tests are consistent with that of tensile strain rate jump tests. For CG nickel the indent rate has little influence on hardness, resulting in a low value of SRS. Identical pop-in behaviour was observed in the F-h curves, indicating dislocation nucleation and motion in the grain. The SRS increases as the grain sizes decrease down to UFG and NC scale, especially in the lower

indent rate range; (3) CG nickel show much higher AV values (1000–1500  $b^3$ ) than that of NC nickel (8–32  $b^3$ ). Analyses of the AV values confirmed that the plasticity in CG nickel is carried by dislocations generated from Frank-Read-like sources within grains; in NC nickel, however, the dislocations are nucleated from grain boundaries. From the above discussions it can be concluded that there is a transition in the dominating deformation mechanism as grain size decreases from conventional CG size range to nanograin size range, which is responsible for the deviation of H-P behaviour observed in NC materials.

2. Room temperature creep behaviour. Room temperature creep is observed only in NC nickel. Results show that in NC nickel grain boundary sliding or diffusion along interface seem to dominate at lower stress levels, but with increasing stresses the deformation process is mainly controlled by dislocation creep;
3. The bending behaviour, fatigue response and fracture of bulk NC nickel revealed by the in-situ bending AFM. For the first time, grain boundary sliding at room temperature is observed playing an important role in bulk NC nickel during bending and fatigue tests. The fatigue crack of bulk NC nickel is revealed to be intergranular, which is different from the well-known intragranular fracture behaviour in coarse-grained metals.

# **A Mechanical properties of different as-deposited nanonickel**

The mean grain size of different as-deposited NC nickel measured by AFM and XRD are summarized in table A.1. Microhardness, nanohardness and reduced modulus of as-deposited nickel are listed table A.1. The peak force of the microindentation that was used is 490 mN. For nanoindentation the peak force used is 2000  $\mu\text{N}$ , the load function is shown in Fig. 4.8. Tensile experiments are performed at different as-prepared nickel specimens with the hydraulic high-speed tensile machine Instron 8511 with a plastic strain rate of  $1.7 \times 10^{-2} \cdot \text{s}^{-1}$ . The engineering stress-strain curves are plotted in Fig. A.1.

No.	From AFM Section (nm)	From XRD (nm)	Microhardness <i>HV</i> (GPa)	Reduced modulus (GPa)
59	21	28	$3.12 \pm 0.04$	$169 \pm 10.1$
62	19	38	$2.25 \pm 0.07$	$165 \pm 16$
87	21.2	28.7	$4.72 \pm 0.03$	$170 \pm 10$
88	27	30.1	$4.51 \pm 0.03$	$168.52 \pm 11$
90	24	28	$4.78 \pm 0.03$	$156.8 \pm 14$
91	21	26	$4.93 \pm 0.04$	$171.7 \pm 11.2$

Table A.1: Mean grain size, microhardness, nanohardness and reduced modulus of different as-deposited NC nickel specimens.

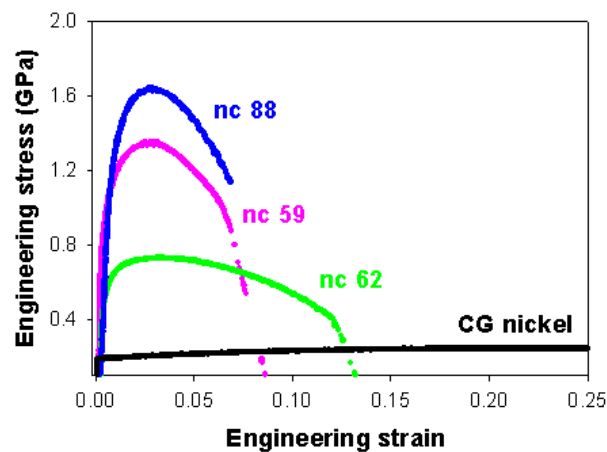


Figure A.1: Engineering stress-strain curves at high strain rates for as-prepared nickel. The black curve corresponds to the behaviour of CG nickel, the colour ones correspond to different as-deposited NC nickel.

## B Effects of annealing on tensile properties of nanonickel

Fig. B.1 shows the room temperature engineering stress-strain curves of as-deposited and heat-treated NC nickel 87 at a strain rate of  $1.7 \times 10^{-2} \cdot s^{-1}$ . To avoid the overlapping of multiple stress-strain curves, the tensile plots are displaced along the X-axis for clarity. The fractographs of the specimens were shown in Fig. B.2.

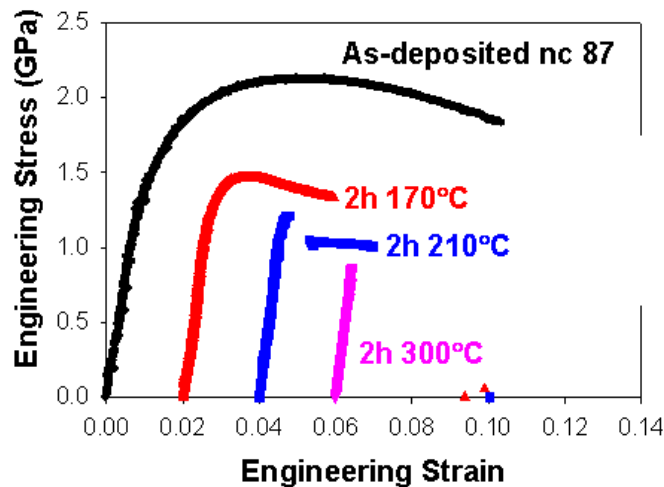


Figure B.1: Room temperature engineering stress-strain curves of as-deposited and heat-treated NC nickel 87 at a strain rate of  $1.7 \times 10^{-2} \cdot s^{-1}$ . To avoid the overlapping of multiple stress-strain curves, the tensile plots are displaced along the X-axis for clarity.

Compared to the as-deposited NC nickel, the heat treated specimens show lower tensile strength as well as a reduced elongation, especially at a higher temperature (300°C). Ductile dimples can be seen for as-deposited NC nickel (Fig. B.2a), but the dimple sizes are much

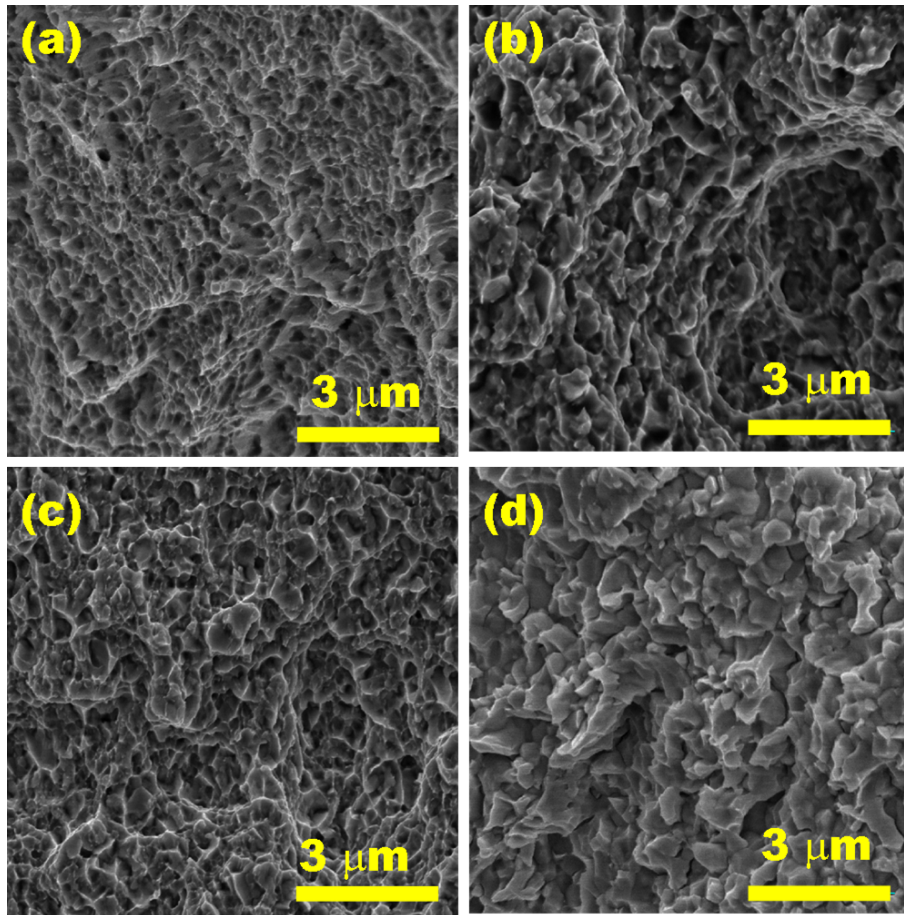


Figure B.2: SEM fractographs of electrodeposited nickel. (a) as-deposited; (b) annealed at 170°C for 2 h; (c) annealed at 210°C for 2 h; (d) annealed at 300°C for 2 h. The mean grain size increases from original size (smaller than 30 nm, (a)) to about 900 nm for annealed nickel (d).

larger than the grain size; these ductile dimples reduce extremely after annealing.

Annealing at low temperature can lead to a change in the grain boundary structure to an equilibrium state through the elimination of grain boundary dislocations contained in as-deposited NC samples [Wan02]. As the strain  $\epsilon$  related to the dislocation density  $\rho$  by the relation of  $\epsilon = \alpha \rho b s$  ( $\alpha$  is constants,  $b$  the burgers vector and  $s$  the average distance each dislocation has moved) [Cot53], a lower dislocation density due to the annihilation of dislocations would lead to a lower tensile strain. This may result in a lower elongation as observed after annealing at 200°C for 2 h.

The dramatic embrittlement of electrodeposited nickel at room temperature after annealing at

relatively higher temperatures may result from the impurities segregation at grain boundaries. Contamination from the ingredients in the electroplating bath is a long-standing issue. The impurities incorporated into the deposits can include sulfur, nitrogen, oxygen, hydrogen and some metallic elements that come from bath additives such as coumarin or saccharin as well as from anode materials [Wan04, Kum03]. At as-deposited state or specimens annealed at low temperatures, these impurities are assumed to be uniformly distributed in the specimen and no effects on the mechanical property (or very trivial if any). At high temperature, as the diffusivity of impurity elements (like sulfur) in Ni is several orders higher than the self-diffusivity of Ni at these annealing temperatures [Heu00], S and impurities similar to S are expected to segregate to the much smaller number of grain boundaries of larger grains. Concentration of sulfur along the grain boundaries has also been reported in annealed electrodeposited nickel [Hib02, Wan04]. In this experiments EDX was used to analyse the fracture surface of different specimens. However, within the resolution of the EDX, no impurities were detected in as-deposited nickel as well annealed samples.

# **C The reverse Hall-Petch effect caused by annealing**

## **C.1 Effects of annealing on the hardness and elastic modulus**

As can be seen in Fig. 4.7, hardness decreases with decreasing grain sizes at the smallest grain size range (segment 3), resulting in a change of the H-P slope from a positive value to negative value. The same behaviour was also obtained in the other indentation results (segment 3 of Fig. 4.7, segment 5 of Fig. 4.10, segment 3 of Fig. 5.2). In addition, an increase in reduced modulus about 15% was observed after heat treatment (segment I of Fig. 4.10). For clarity we plot the modulus as a function of heat-treatment, as shown in Fig. C.1. It is clear that as-deposited NC nickel has a lower modulus compared to the heat treated ones.

The slight increase in grain size (from original 22.2 nm to 24 nm measured by AFM) is produced by a low temperature annealing at 150°C for 0.5 h to as-deposited NC nickel. In the heat treated specimens hardness always decreases with increasing grain size.

## **C.2 Explanations**

The change of H-P behaviour caused by annealing seems to be a common phenomenon in NC materials. Carl. C. Koch and J. Narayan [Koc01] critically reviewed the data in literature which gives softening — the inverse Hall-Petch effect — at the finest nanoscale grain sizes. They pointed out that most data that exhibit the negative H-P effect at the smallest grain sizes have

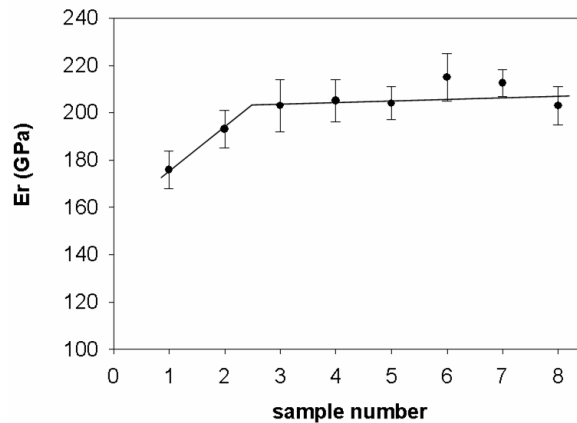


Figure C.1: Reduced modulus evolution with heat treatments. All specimens were produced by different heat treatments on NC nickel (No. 87). The numbers in the x-coordinate correspond to different specimens: (1) as-deposited; (2) 150°C for 0.5 h; (3) 170°C for 0.5 h; (4) 190°C 2 h; (5) 210°C for 2 h; (6) 250°C for 2 h; (7) 280°C for 2 h; (8) 300°C for 2 h.

resulted from NC samples that have been annealed to increase their grain size. It is suggested that thermal treating of NC materials in the as-produced condition may result in changes in structure such as densification, stress relief, phase transformations or grain boundary structure, all that may lead to the observed negative H-P behavior.

Electroplated NC Ni is considered fully dense with only minor micro- and nanoscale pores, therefore it is unlikely that the density change is the only cause for the notable strengthening upon thermal annealing; the redistribution of the trace amounts of impurities may have some effects on the strength, but redistribution is difficult to take place at low temperatures in a short time (150°C for 0.5 h), at least this was not detected by EDX (or beyond its detection limit).

NC metals have high grain boundary interfacial area/volume ratio (see Fig. 5.19). Owing to the high percentage of grain boundary area, NC materials have been viewed as a ‘composite’ of grains with normal lattice atoms and the grain boundary region comprising atoms with different interatomic spacing [Wan93]. The grain boundary region characterizes lower elastic modulus than the normal lattice atoms. Grain growth caused by annealing will result in a the reduction of the softer part, therefore an increase the elastic modulus (see Fig. C.1) and hardness.

Grain boundary regions in as-deposited NC materials are always in a high non-equilibrium

state, containing lots of grain boundary dislocations randomly oriented. Recent MD simulation suggests that thermal annealing can lead to strengthening of NC metals due to relaxation at the non-equilibrium grain boundaries. Annealing can change the grain boundary structure to an equilibrium state through the redistribution of grain boundary dislocations in the samples [Wan02]. This process is accompanied with significant reduction of grain boundary dislocations and makes it more difficult for such relaxed grain boundaries to emit dislocations or undergo grain boundary sliding. As a result, the material becomes more resistant to yielding under applied stresses, thus resulting in a hardening effect [Fed03, Gut03].

To check this effect, XRD was used to analyse the average grain size and microstrain of the two specimens (as-deposited and heat-treated at 150°C for 0.5 h). The results (table C.1) show a little decrease in the microstrain after annealing, suggesting the (grain boundary) dislocation reorganization activities.

<b>Specimen</b>	<b>As-deposited</b>		<b>150°C for 0.5 h</b>	
Applied methods	Grain Size (nm)	Microstrain	Grain Size (nm)	Microstrain
Cauchy size broadening/ Cauchy size broadening	$45.9 \pm 35.9$	$0.002 \pm 0.0011$	$49.4 \pm 44.7$	$0.0021 \pm 0.0012$
Gaussian size broadening/ Gaussian size broadening	$28.7 \pm 11.5$	$0.0026 \pm 0.0007$	$26.9 \pm 9.6$	$0.0025 \pm 0.0007$
Cauchy size broadening/ Gaussian size broadening	$22.7 \pm 11.7$	$0.0012 \pm 0.0019$	$21.5 \pm 8.4$	$0.001 \pm 0.0024$

Table C.1: Grain size and microstrain of as-deposited and annealed nanocrystalline nickel measured by XRD.

# Bibliography

- [Alv96] H. Alves, M. Ferreira, U. Koster, B. Muller, *Materials Science Forum* **769** (1996) 225.
- [Asa05] R.J. Asaro and S. Suresh, *Acta Mater.* **53** (2005) 3369.
- [Ash71] M.F. Ashby, in: A. Kelly et al(eds.), *Strengthening Methods in Crystals*, Elsevier, Amsterdam 1971.
- [Ash72] M.F. Ashby, *Acta Metall.* **20** (1972) 887.
- [Aus93] K.T. Aust, U. Erb and G. Palumbo, in *Mechanical Properties and Deformation Behaviour of Materials Having Ultrafine Microstructures*, M. Nastasi et al(eds.), Kluwer Academic Publishers, (1993) 107.
- [Bak93] I. Bakonyi et al., *Nanostr. Mat.* **3** (1993) 155.
- [Bar01] M. D. Baro et al., *Rev. Adv. Mater. Sci.* **2** (2001) 1.
- [Bir89] R. Birringer, *Mat. Sci. Eng. A* **117** (1989) 33.
- [Bir84] R. Birringer, H. Gleiter, H. P. Klein and P. Marquardt, *Phys. Lett. A* **102** (1984) 365.
- [Bon91] R. Bohn, T. Haubold, R. Birringer, H. Gleiter, *Scr. Metall. Mater.* **25** (1991) 811.
- [Bra04] J. E. Bradby, J.S. Willams and M.V. Swain, *J. Mater. Res.* **19(1)** (2004) 380.
- [Bud04] Z. Budrovic, H. Van Swygenhoven, P. M. Derlet, S. Van Petegem, B. Schmitt, *Science* **304** (2004) 273.
- [Bhu03] B. Bhushan and X. Li, *International Materials Reviews* **48** (2003) 125.

- [Cad88] J. Cadek, *Creep in Metallic Materials*, Elsevier Science Publishing Company, New York, 1988.
- [Cah83] R.W. Cahn and P. Haasen, *Physical Metallurgy*, 3rd ed., North-Holland Physics Publ., USA, 1983.
- [Cah01] J.W. Cahn and F. R. N. Nabarro, *Phil. Mag. A* **81** (2001) 1409.
- [Cai99] B. Cai, Q.P. Kong, L. Lu and K. Lu, *Scr. Mater.* **41** (1999) 755.
- [Che03] S. Cheng, J.A. Spencer, W.W. Milligan, *Acta Mater.* **51** (2003) 4505.
- [Che03a] M. W. Chen et al., *Science* **300** (2003) 1275.
- [Cho89] A.H. Chokshi, *Scr. Metall.* **23** (1989) 1679.
- [Cob63] R.L. Coble, *J. Appl. Phys.* **34(6)** (1963) 1679.
- [Con03] H. Conrad, *Mater. Sci. Eng. A* **341** (2003) 216.
- [Cot53] A.H. Cottrell, *Dislocations and Plastic Flow in crystals*, Oxford University Press, 1953.
- [Dal05] F. Dalla Torre, P. Spätig, R. Schäublin, M. Victoria, *Acta Mater.* **53** (2005) 2337.
- [Des87] A.R. Despic, V. D. Jovic, *J. Electrochem. Soc.* **134** (1987) 3004.
- [Doe86] M.F. Doerner, W. D. Nix, *J. Mater. Res.* **1** (1986) 601.
- [Dur05] K. Durst, B. Backes, M. Göken *Scripta Mater.* **52** (2005) 1093.
- [Eas92] J. A. Eastman et al., *Nanostruct. Mater.* **1(1)** (1992) 47.
- [Ebr98] F. Ebrahimi et al., *Scr. Mater.* **21** (1998) 315.
- [Ebr99] F. Ebrahimi et al., *Nanostruct. Mater.* **11** (1999) 343.
- [Ehr97] W. Ehrfeld, V. Hessel, H. Loewe, C. Schulz and L. Weber, *Proc. of 2nd Int. Conf. of MicroMaterials 97*, Berlin 1997.

- [Els95] A. M. Elsharik and U. Erb, *J. Mater. Sci.* **30** (1995) 5743.
- [Erb93] U. Erb, A. M. El-Sherik, G. Palumbo, K. T. Aust, *Nanostr. Mat.* **2** (1993) 383.
- [Erb95] U. Erb, *Nanostructured Mater.* **6** (1995) 533.
- [Far02] D. Farkas, H. Van Swygenhoven, P.M. Derlet, *Phys. Rev. B* **66** (2002) 060101-1.
- [Fec95] H.J. Fecht, *NanoStruc. Mater.* **6** (1995) 33.
- [Fed03] A.A. Fedorov, M. Yu. Gutkin, I. A. Ovid'ko, *Acta Mater.* **51** (2003) 887.
- [Fen04] G. Feng, W.D. Nix, *Scripta Mater.* **51** (2004) 599.
- [Fit91] M.R. Fitzsimmons et al., *Phys. Rev. B* **44(6)** (1991) 2452.
- [Fle94] N.A. Fleck, G.M. Muller, M.F. Ashby, J.W. Hutchinson, *Acta Met. Mater.* **42** (1994) 475.
- [Fro04] A.G. Froseth, P.M. Derlet, H. Van Swygenhoven, *Acta Mater.* **52** (2004) 5863.
- [Gai03] Y. Gaillard, C. Tromas, J. Woirgard, *Acta Mater.* **51** (2003) 1059.
- [Gil83] P.S. Gilman and J.S. Benjamin, *Ann. Rev. Mater. Sci.* **11** (1983) 279.
- [Gif68] R.C. Gifkins, *J. Am. Ceram. Soc.* **51** (1968) 69.
- [Gle89] H. Gleiter, *Prog. Mat. Sci.* **33** (1989) 223.
- [Gou01] A. Gouldstone, K. J. Van Vliet and S. Suresh, *Nature* **411** (2001) 656.
- [Gök99] M. Göken, M. Kempf, *Acta Mater.* **47** (1999) 1043.
- [Gök02] M. Göken, F. Thome and H. Vehoff, *Philosophical Magazine A* **82** (2002) 3241.
- [Gök01] M. Göken, M. Kempf, *Z. Metallkd.* **92** (2001) 1061.
- [Gus98] AI Gusev, *Physics - Uspekhi* **41(1)** (1998) 49.
- [Gut01] M.Y. Gutkin, I. A. Ovidko, C. S. Pande, *Rev. Adv. Mater. Sci.* **2** (2001) 80.

- [Gut03] M. Yu. Gutkin, I. A. Ovid'ko, N.V. Skiba, *Acta Mater.* **51** (2003) 4059.
- [Hal51] E.O. Hall, *Proc. Phys. Soc. London* **B64** (1951) 747.
- [Han05] B. Han et al., *Rev. Adv. Mater. Sci.* **9** (2005) 11.
- [Höp02] H. W. Höppel, Z. M. Zhou, H. Mughrabi, R. Z. Valiev, *Phil. Mag. A* **82** (2002) 1781.
- [Has03] A. Hasnaoui, H. Van Swygenhoven, P. M. Derlet, *Science* **300** (2003) 1550.
- [Hau89] T. Haubold, R. Birringer, B. Lengeler, H. Gleiter, *Phys. Lett. A* **135** (1989) 461.
- [Her50] C. Herring, *J. Appl. Phys.* **21** (1950) 437.
- [Her81] H. Hertz, *J. Reine Angew. Math.* **92** (1881) 156.
- [Heu00] J.K. Heuer, P. R. Okamoto, N. Q. Lam, J. F. Stubbins, *Appl. Phys. Lett.* **76** (2000) 3403.
- [Hib02] D.D. Hibbard, J. L. McCrea, G. Palumbo, K. T. Aust, U. Erb, *Scripta Mater.* **47** (2002) 83.
- [Hir92] J.P. Hirth and J. Lothe, *Theory of Dislocation*, Krieger, Malabar, FL 1992.
- [Hir92] J.P. Hirth and J. Lothe, *Theory of Dislocations*, 1st edn. Wiley, New York, 1982, pp.306-353.
- [Hol04] C. Holste, *Phil. Mag.* **84** (2004) 299.
- [Hor87] J. Horvath, R. Birringer, H. Gleiter, *Solid State Commun.* **62** (1987) 319.
- [Jia95] Z. Jiang, J. Lian and B. Baudalet, *Acta Metall. Mater.* **43** (1995) 3349.
- [Kar87] J. Karch, R. Birringer, H. Gleiter, *Nature* **330** (1987) 556.
- [Kem02] M. Kempf, M. Göken, H. Vehoff, *Mat. Sci. Eng. A* **184** (2002) 329.
- [Kem02a] M. Kempf, Dissertation, Saarbrücken, Germany, 2002.
- [Kie98] J.D. Kiely and J. E. Houston, *Phys. Rev. B* **57** (1998) 12588.

- [Kna04] J.A. Knapp and D.M. Follstaedt, *J. Mater. Res.* **19** (2004) 218.
- [Kim99] H.S. Kim and M. B. Bush, *Nanostruct. Mater.* **11** (1999) 361.
- [Krs93] V. Krstic, U. Erb, and G. Palumbo, *Scr. Metall. Mater.* **29** (1993) 1501.
- [Kri98] C.E. Krill and R. Birringer, *Phil. Mag. A* **77(3)** (1998) 612.
- [Koc75] U.F. Kocks, A. S. Argon and M. F. Ashby, *Thermodynamics and kinetics of slip*, 1st ed., Pergamon Press Ltd., Oxford, 1975.
- [Koc01] C.C. Koch and J. Narayan, *Mat. Res. Soc. Symo.* **634** (2001) B5.1.1.
- [Koc02] C.C. Koch, *Nanostructured Materials*, Noyes Publications, Norwich, New York 2002.
- [Koc89] C.C. Koch, *Ann. Rev. Mater. Sci.* **19** (1989) 121.
- [Kum03] K.S. Kumar, H. Van Swygenhoven, S. Suresh, *Acta Mater.* **51** (2003) 5743.
- [Kum03a] K. S. Kumar, S. Suresh, M. F. Chisholm, J. A. Horton, P. Wang, *Acta Mater.* **51** (2003) 387.
- [Leg00] M. Legros et al., *Philos. Mag. A* **80** (2000) 1017.
- [Li02] X. Li and B. Bhushan, *Materials Characterization* **48** (2002) 11.
- [Li63] J.C.M. Li, *Trans. Metall. Soc. AIME* **277** (1963) 239.
- [Li70] J.C.M. Li and Y.T. Chou, *Metall. Trans.* **1** (1970) 1145.
- [Lia03] X.Z. Liao, *Appl. Phys. Lett.* **83** (2003) 632.
- [Lia04] X.Z. Liao et al., *J. Appl. Phys.* **96** (2004) 636.
- [Lor03] D. Lorenz, A. Zeckzer, U. Hilpert, and P. Grau, *Phys. Rev. B* **67** (2003) 172101.
- [Lu96] K. Lu, *Mat. Sci. Eng. R* **16** (1996) 161.
- [Lu00] L. Lu, M. L. Sui and K. Lu, *Science* **287** (2000) 1463.
- [Lu01] Y. Lu and P. K. Liaw, *JOM* **53(3)** (2001) 31.

- [Lüt79] H. Lüthy, R. A. White, O.D. Sherby, *Mater. Sci. Eng.* **39** (1979) 211.
- [Maq95] Q. Ma, D.R. Clarke, *J. Mater. Res.* **10** (1995) 853.
- [Mar03] M. Marx, Dissertation, Saarbrücken, Germany, 2003.
- [Mar04] J. Markmann, Dissertation, Saarbrücken, Germany, 2004.
- [Mas98] R.A. Masumura, P. M. Hazzledine, C. S. Pande, *Acta Mater.* **46** (1998) 4527.
- [May05] J. May, H.W. Höppel, M. Göken, *Scr. Mater.* **53** (2005) 189.
- [May88] M.J. Mayo and W.D. Nix, *Acta Metall.* **36** (1988) 2183.
- [McF99] S.X. McFadden, R. S. Mishra, R. Z. Valiev, A. P. Zhilyaev, A. k. Mukherjee, *Nature* **398** (1999) 684.
- [McC04] M. McCann, Dissertation, 2004, Blacksburg, Virginia, USA.
- [Mey82] M.A. Meyers and E. Ashworth, *Phil. Mag.* **46** (1982) 737.
- [Min04] A.M. Minor, E.T. Lilleodden, E.T. Atach, J.W. Morris. Jr., *J. Mater. Res.* **19(1)** (2004) 176.
- [Mor97] D.G. Morris and M.A. Morris, *Mater. Sci. Forum* **861** (1997) 235.
- [Mor01] J.W. Morris, in: S. Takaki, T. Maki (eds.), *International Symposium on Ultrafine Grained Steels, Iron and Steel Inst. Japan*, 2001.
- [Muk02] A.K. Mukherjee, *Mater. Sci. Eng. A* **322** (2002) 1.
- [Mug91] H. Mughrabi, in *Plastic Deformation and Fracture of Materials*, R. W. Cahn, P. Haasen, E. J. Kramer, Eds., *vol. 6 of Materials Science and Technology*, Wiley-VCH, Weinheim, Germany, 1991, pp. 1-19.
- [Mut98] T. Mutschele and R. Kirchheim, *Scr. Mater.* **39** (1998) 315.
- [Nab48] F.R.N. Nabarro, *Report of a conference on Strength of Solids*, The Physical Society, London, 1948, pp. 75-90.

- [Nan96] *NanoScope: Command Reference Manual*, Version 4.20, Digital Instruments Inc., California, 1996.
- [Nat96] H. Natter, R. Hempelmann, *J. Phys. Chem.* **100** (1996) 19525.
- [Nat98] H. Natter, M.Schmelzer and R. Hempelmann, *J. Mater. Res.* **13** (1998) 1186.
- [Nie91] T.G. Nieh, J. Wadsworth, *Scr. Metall.* **25** (1991) 955.
- [Niem90] G.W. Nieman, J. R. Weertman and R.W. Siegel, *Scr. Metall. Mater.* **24** (1990) 145.
- [Niem91] G.W. Nieman, J.R. Weertman and R. Siegel, *J. Mater. Res.* **6** (1991) 1012.
- [Nie97] T.G. Nieh, J. Wadsworth, O.G. Sherby, *Superplasticity in metals and ceramics*, 1st edn., Cambridge University Press, Cambridge, UK, 1997.
- [Nix98] W.D. Nix and H. Gao, *J. Mech. Phys. Solids* **46(3)** (1998) 411.
- [Nor29] F.H. Norton, *Creep of Steel at High Temperature*, McGraw Hill, New York 1929.
- [Oro54] E. Orowan, *Dislocation in Metal*, Amer. Inst. Min. (Metall.) Engres. (1954).
- [Oli92] W.C. Oliver and G. M. Pharr, *J. Mater. Res.* **7** (1992) 1564.
- [Pal90] G. Palumbo, S. J. Thorpe, K. T. Aust, *Scr. Metall. Mater.* **24** (1990) 1347.
- [Pet53] J. Petch, *J. Iron Steel Inst.* **174** (1953) 25.
- [Pha92] G.M. Pharr, W. C. Oliver and F. R. Brotzen, *J. Mater. Res.* **7** (1992) 613.
- [Poi95] W.H. Poisl, W.C. Oliver and B. D. Fabes, *J. Mater. Res.* **10** (1995) 2024.
- [Ree91] R.E. Reed-Hill and R. Abbaschian, *Physical Metallurgy Principles*, 3rd Edition, PWS Publishing Company, USA, 1991, pp285.
- [Rit97] M.N. Rittner, J. R. Weertman, J. A. Eastman, K. B. Yoder and D. S. Stone, *Mater. Sci. Eng. A* **237** (1997) 185.
- [Ros05] A. Rosochowski, *Solid State Phenomena* **101-102** (2005) 13.

- [Rob99] A. Robertson, U. Erb, G. Palumbo, *Nanostruct. Mater.* **12** (1999) 1035.
- [San97] P.G. Sanders, J. A. Eastman and J. R. Weertman , *Acta Mater.* **45** (1997) 4019.
- [Sax02] A. Saxena, *Proc. Semin. On 'Strength, fracture and fatigue behavior of nanostructured materials'*, Singapore 2002.
- [Sch98] J. Schiotz, F. D. DiTolla, K. W. Jacobsen, *Nature* **391** (1998) 561.
- [Sch03] R. Schwaiger, B. Moser, M. Mao, N. Chollacoop, S. Suresh, *Acta Mater.* **51** (2003) 5159.
- [Sch04] J. Schiotz, *Scripta Mat.* **51** (2004) 837.
- [Sne65] I.N. Sneddon, *International Journal of Engineering Science* **3** (1965) 47.
- [Sha04] Z.W. Shan et al., *Science* **305** (2004) 654.
- [Sha05] Z. Shan and Scott X. Mao, *Advanced Engineering Materials* **7** (2005) 603.
- [She95] T.D. Shen, C. C. Koch, T. Y. Tsui, G. M. Pharr, *J. Mater. Res.* **10** (1995) 2892.
- [Shi93] M. Shirkhazadeh, *Mat. Lett.* **16** (1993) 189.
- [Sie93] R.W. Siegel, *Nanostruct. Mater.* **3** (1993) 1.
- [Sie97] R.W. Siegel, *Materials Science Forum* **851** (1997) 235.
- [Sio04] K.S. Siow, A. A. O. Tay, P. Oruganti, *Mater. Sci. Tech.* **20** (2004) 285.
- [Sor03] J. B. Sorensen, J. Schiotz, *Science* **300** (2003) 1244.
- [Sun00] X.K. Sun, H. T. Cong, M. Sun and M. C. Yang, *Metall. Mater. Trans. A* **31A** (2000) 1017.
- [Sur95] C. Suryanarayana, *Inter. Mater. Rev.* **40** (1995) 41.
- [Sur92] C. Suryanarayana and F. H. Froes, *Metall. Trans. A* **23A** (1992) 1071.
- [Swa02] J.G. Swadener, E.P. George, G.M. Pharr, *J. Mech. Phys. Solids* **50** (2002) 681.

- [Tab51] D. Tabor, *The Hardness of Metals*, Oxford University Press, London, 1951.
- [Tak92] L. Takacs, *Mate. Lett.* **13** (1992) 119.
- [Tel01] V.L. Tellkamp, A. Melmed and E. J. Lavernia, *Metall. Mater. Trans. A* **32A** (2001) 2335.
- [Tho99] F. Thome, M. Göken, H. Vehoff, *Intermetallics* **7(3-4)** (1999) 491.
- [Tri96] *Triboscope Nanomechanical Test System User's Manual*, ed. H. Inc., Minneapolis, 1996.
- [Val93] R.Z. Valiev, A. Korsnikov, R. R. Mulyukov, *Mater. Sci. Eng. A* **166** (1993) 143.
- [Val00] R.Z. Valiev, R. K. Islamgaliev, I. V. Alexandrov, *Prog. Mat. Sci.* **45** (2000) 103.
- [Val97] R.Z. Valiev, *Mater. Sci. Eng. A* **234-236** (1997) 59.
- [Van97a] H. Van Swygenhoven, A. Caro, *Appl. Phys. Lett.* **71** (1997) 1652.
- [Van99] H. Van Swygenhoven, M. M. Spaczer, A. Caro, and D. Farkas, *Phys. Rev. Lett.* **60** (1999) 22.
- [Van02] H. Van Swygenhoven, *Science* **296** (2002) 66.
- [Van02a] A. Hasnaoui, H. Van Swygenhoven, P. M. Derlet, *Phys. Rev. B* **66** (2002) 184112.
- [Van04] H. Van Swygenhoven, P. M. Derlet, A. G. Froseth, *Nature* **31** (2004) 399.
- [Van04a] H. Van Swygenhoven, P. M. Derlet, A. G. Froseth, *Nature* **31** (2004) 399.
- [Veh79] H. Vehoff and P. Neumann, *Acta Metall.* **27** (1979) 915.
- [Veh80] H. Vehoff and P. Neumann, *Acta Metall.* **28** (1980) 265.
- [Veh97] H. Vehoff, P. Ochmann, M. Göken, M. Grosse Gehling, *Mater. Sci. Eng. A* **239-240** (1997) 378.
- [Wan93] N. Wang, G. Palumbo, Z. Wang, U. Erb, K. T. Aust, *Scr. Metall. Mater.* **28** (1993) 253.

- [Wan97] N. Wang, Z. Wang, K.T. Aust, U. Erb, Mater. Sci. Eng. A **237** (1997) 150.
- [Wan02] Y. Wang, M. Chen, F. Zhou, E. Ma, Nature **491** (2002) 912.
- [Wan04] Y.M. Wang et al., Scripta Mater. **51** (2004) 1023.
- [Wee99] J.R. Weertman, D. Farkas, K. Hemker, H. Kung, M. Mayo, R. Mitra and H. Van Swygenhoven, MRS Bull. **24** (1999) 44.
- [Wei04] Q. Wei, S. Cheng, K. T. Ramesh, E. Ma, Mater. Sci. Eng. A **381** (2004) 71.
- [Wel04] M. Welsch, Diploma Thesis, Saarbrücken, Germany, 2004.
- [Wür87] R. Würshum, M. Scheytt, H. E. Schaefer, Phys. stat. sol. (a) **102** (1987) 119.
- [Wol05] D. Wolf et al, Acta Mater. **53** (2005) 1.
- [Www01] [www.tf.uni-kiel.de/matwis/amat/mwl\\_ge/kap\\_a/bachbone/ra\\_2\\_1.html](http://www.tf.uni-kiel.de/matwis/amat/mwl_ge/kap_a/bachbone/ra_2_1.html).
- [Www02] <http://num.web.psi.ch/reports/2004/ASQ/asq-2004-03.pdf>.
- [Www03] [www.nanoindentation.cornell.edu/home\\_main.htm](http://www.nanoindentation.cornell.edu/home_main.htm).
- [Yip98] S. Yip, Nature **391** (1998) 532 .
- [Yam00] T. Yamasaki, Mater. Phys. Mech. **1** (2000) 127.
- [Yam02] V. Yamakov et al., Nature **1** (2002) 1.
- [Yam02a] V. Yamakov, D. Wolf, S. R. Phillpot, H. Gleiter, Acta Mater. **50** (2002) 5005.
- [Yam02b] V. Yamakov, D. Wolf, S. R. Phillpot, A. K. Mukherjee, H. Gleiter, Nature Mater. **1** (2002) 45.
- [Yam03] V. Yamakov, D. Wolf, S. R. Phillpot, A. K. Mukherjee, H. Gleiter, Phil. Mag. Lett. **83** (2003) 385.
- [Yam04] V. Yamakov et al., Nat. Mater. **3** (2004) 43.
- [Zhou03] Y. Zhou, U. Erb, K. T. Aust, G. Palumbo, Scr. Mater. **48** (2003) 825.

[Zho03] F. Zhou, X. Z. Liao, Y.T. Zhu, S. Dallek, E. J. Lavernia, *Acta Mater.* **51** (2003) 2777.

[Zhu04] Y.T. Zhu and T.G. Langdon, *JOM* **56(10)** (2004) 58.

[Zhu87] X. Zhu, R. Birringer, U. Herr, H. Gleiter, *Phys. Rev. B* **35** (1987) 9085.

# Publications

1. B. Yang, H. Vehoff, to be submitted to Int. J. Mat. Res., *Pop-ins in nanoindentation on Ni crystal - from the influence of specimen preparation to the grain size effect*
2. B. Yang, H. Vehoff, M. Göken, to be submitted, *A study on the fracture process of NiAl single crystal by applying atomic force microscopy*
3. B. Yang, H. Vehoff, submitted to Acta Mater., *The effect of lateral interfaces on the indentation size effect - a local examination of the interaction between dislocations and grain boundaries*
4. B. Yang, H. Vehoff, R. Hempelmann, Z. Metallkd., in press (2006), *The deformation behaviour of electrodeposited nanocrystalline Ni in an atomic force microscopy with a newly developed in-situ bending machine*
5. B. Yang, H. Vehoff, Mater. Sci. Eng. A, **400-401** (2005) 467, *Grain size effects on the mechanical properties of nanonickel examined by nanoindentation*
6. B. Yang, H. Vehoff, Z. Metallkd. **95** (2004) 6, *The effect of grain size on the mechanical properties of nanonickel examined nanoindentation*
7. Bo Yang, Chinese J. of Rare Metals, **25** (2001) 36, *Influence of Annealing on Microstructure and Forging Property of Steel Bonded Hard Alloys*
8. C. Wang, B. Yang and M. Zhou, Chinese J. Rare Metals and Cemented Carbides, **132** (1998) 13, *Study on Forge Deformation and Microstructure of Steel Bonded Hard Alloys*